Politecnico di Milano

School of Industrial and Information Engineering
Master of Science in Nuclear Engineering

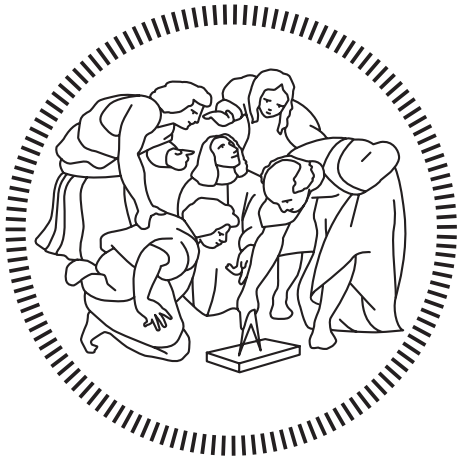

Development of non-conventional targets for laser-driven particle sources

Supervisor
Prof. Matteo Passoni

Co-Supervisor
Ing. Davide Vavassori

Candidate
Francesco Gatti – 919407

Academic Year 2020 – 2021

Contents

Acronyms

BNCT	Boron Neutron Capture Therapy
CE	Coulomb Explosion
CPA	Chirped Pulse Amplification
CVD	Chemical Vapour Deposition
DCMS	Direct Current Magnetron Sputtering
DLT	Double Layer Target
EDXS	Energy Dispersive X-ray Spectroscopy
HiPIMS	High Power Impulse Magnetron Sputtering
MS	Magnetron Sputtering
OPA	Optical Parametric Amplification
OPCPA	Optical Parametric Chirped Pulse Amplification
PIC	Particle-In-Cell
PIGE	Proton Induced Gamma-ray Emission
PIXE	Particle Induced X-ray Emission
PLD	Pulsed Laser Deposition
PVD	Physical Vapour Deposition
RPA	Radiation Pressure Acceleration
SEM	Scanning Electron Microscopy
SLT	Single Layer Target
TNSA	Target Normal Sheath Acceleration

List of Figures

List of Tables

Abstract

The study of laser interaction with matter is a research topic of strong interest, both for fundamental science and for application-oriented reasons. Among these, there is the possibility of accelerating particles. Sources of various kind can be obtained, for example protons ones. It has to be highlighted that, due to the peculiar characteristics of laser-driven sources, such as high laminarity and pulsed nature, they are complementary and not competitive to conventional ones. A broad range of applications of such sources is foreseen in various sectors: materials science, industrial processes, biomedical applications, radioisotopes production, experimental physics and inertial confinement nuclear fusion research. Parallel to the development of laser systems, the study and the optimization of the targets with whom the radiation interacts has proved to be of fundamental importance. This is particularly true in the case of compact sources, based on lasers in the tens of TW power range, which could likely be installed in industries and universities.

To goal of this thesis work is thus to investigate the possibility of producing solid targets, both as pure metallic and multi-layered. In particular, the so-called Double Layer Targets (DLTs) are considered, in which an additional low density material allows to improve the performances of the acceleration system. While the conventional targets typically consist in laminated foils, a strategy to produce these components through direct deposition of the materials on perforated holders is presented in this work. In particular, two Physical Vapour Deposition (PVD) techniques are exploited: Magnetron Sputtering, both as Direct Current (DCMS) and in pulsed mode (HiPIMS), and Pulsed Laser Deposition (PLD). The aim is thus to tune such strategy and to verify its limits of applicability. The direct deposition should allow to obtain films with greater reproducibility in terms of their properties. Thus, in turn, the accelerated particles sources should result as more reliable and with more finely controlled characteristics.

Sommario

Lo studio dell'interazione tra laser e plasma è un tema di ricerca di forte interesse, sia per considerazioni di scienza fondamentale che per ragioni più applicative. Tra queste, trova spazio la possibilità di accelerare particelle e realizzare così sorgenti di varia natura, ad esempio protoni. Grazie alle loro peculiari caratteristiche, quali l'elevata laminarità e la natura pulsata, le sorgenti da laser non sono competitive ma complementari alle sorgenti tradizionali. Infatti, queste trovano possibili sfoghi applicativi in vari ambiti, quali scienza dei materiali, processi industriali, applicazioni biomediche, produzione di radioisotopi ed anche fisica sperimentale e ricerche sulla fusione nucleare a confinamento inerziale. Parallelamente allo sviluppo dei sistemi laser, lo studio e l'ottimizzazione dei bersagli con cui la radiazione interagisce si è rivelato di fondamentale rilevanza. Ciò risulta particolarmente vero nel caso di sorgenti compatte, basate su laser con potenze nell'ordine delle decine TW, che quindi potrebbero verosimilmente essere installate in industrie ed università.

Per questo, l'obiettivo del presente lavoro di tesi è di studiare la possibilità di produrre bersagli solidi, sia puramente metallici che multistrato, in cui uno strato aggiuntivo di materiale a bassa densità permette di migliorare le prestazioni del sistema di accelerazione. Questi ultimi sono chiamati Double Layer Targets (DLTs). Mentre i bersagli convenzionali consistono, tipicamente, in fogli laminati, in questo lavoro viene presentata una strategia per realizzare componenti tramite deposizione diretta dei materiali su holder perforati, sfruttando tecniche fisiche da fase vapore. In particolare, vengono impiegate magnetron sputtering, sia in modalità Direct Current (DCMS) che pulsata (HiPIMS), e Pulsed Laser Deposition (PLD). L'obiettivo è quindi di mettere a punto tale strategia e di verificarne i limiti di applicabilità. Infatti, la deposizione diretta dovrebbe permettere di ottenere film con proprietà maggiormente riproducibili e, di conseguenza, fasci di particelle accelerate più affidabili e con caratteristiche più controllate.

Chapter 1

Laser-driven ion acceleration

In this chapter, an introduction to the topic of laser-driven acceleration is given. Starting from a very brief description of the technology that enables the production of short, high intensity laser pulses and their characteristics in section 1.1, their interaction with matter is then addressed in section 1.2. The process through which ions can be accelerated is depicted in the following (section 1.3), with particular focus on TNSA. Lastly, in section 1.4, some potential practical uses of these kind of sources are described, ranging from materials science to medical applications and to fundamental research.

1.1 Pulsed lasers and high intensity

Light amplification by stimulated emission of radiation was experimentally demonstrated in 1960 by T.H. Maiman. The device built upon this idea, the laser, immediately gained a prominent role in research, spreading its applications to many areas of science and technology. The reasons for such a success rely on its unique characteristics, such as coherence, directionality, and monochromaticity, which make it a quite versatile electromagnetic radiation source.

A laser can be schematized as shown in Figure 1.1. It is composed by a pump, a resonator (which can be a couple of mirrors, one only partially reflecting to allow the beam out) and an active medium.

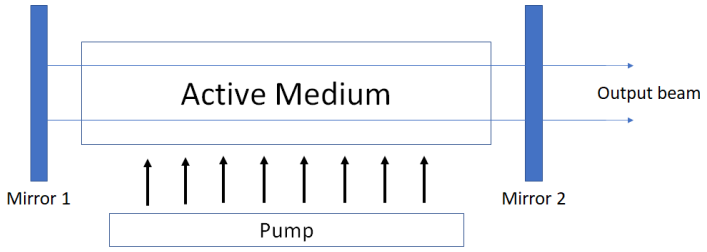

Figure 1.1. Basic scheme of a laser.

The physical phenomenon exploited in a laser is the stimulated emission: the pump, which for example can be a lamp or another laser, gives energy to electrons of the active material, exciting them to a higher level. Then, they can then decay, emitting

photons, stimulated by the electromagnetic wave itself. The radiation is amplified by passing through the media several times, being (partially) confined by the resonator. Since the process is forced by the incident radiation, the emission of every atom adds in phase to that of the incoming wave and along the same direction, giving directionality and coherence.

The active material, also called gain, could be a gas (as He-Ne or CO_2), a solid (like Nd:YAG, Ti:Sapphire or semiconductor diodes) or a liquid (organic dyes). To be able to lasing, it should be in a condition called population inversion.This means that the ground state is much less occupied than the excited state, and so the pump is needed. Nevertheless, media with just two levels cannot reach this condition because of saturation. Indeed, exciting the electrons to the higher state, a stationary condition is reached, in which absorption events equal stimulated emission ones. So, three- or four-level schemes must be adopted, in which the lifetime of the pumping level and of the laser destination state are much shorter than the lasing one (see Figure 1.2).

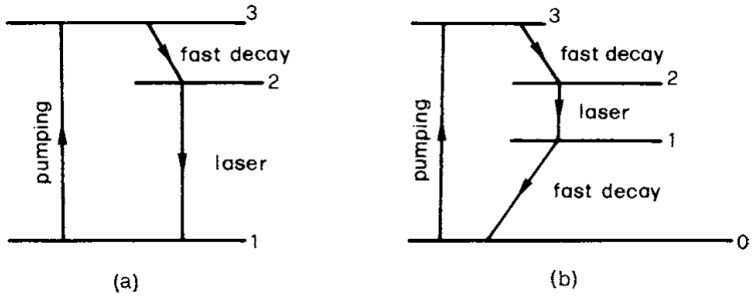

Figure 1.2. (a) Three-level and (b) four-level laser schemes, from [1].

Lasers not only can emit continuous wave radiation, but also electromagnetic pulses, thanks to special techniques: Q-switching and mode locking. It is important to point out that the duration of such pulses, roughly equal to the inverse of the linewidth of the electronic transition, is linked to the frequency spectrum through Fourier transform, meaning that the shorter the pulse, the wider the band ($\Delta t \Delta \nu \geq 1$). Short time duration can be considered as the counterpart of monochromaticity. Note that, anyway, while all lasers can be operated with monochromatic emission, a broad linewidth is needed to deliver short pulses. Given this, solid state active materials are the best candidates for pulsed mode, with durations down to 10 fs [1].

Laser pulses are interesting not only because they allow to investigate processes that happens at such timescales, like molecular dynamics, but also because they pave the way to reach very high intensities. To better understand, consider a Gaussian power profile, ideal but quite realistic:

$$P(t) = P_{peak} \exp{(t/\tau)^2}$$

where P_{peak} is the maximum value of the power and τ is the temporal width. Note that the average power is determined by another relevant characteristic of pulsed lasers: the repetition rate (R_{Rate}). It is the frequency at which the system is able to deliver a pulse, and so $P_{avg} = E_{pulse} \times R_{Rate}$. Intensity, instead, usually refers to the peak value, so it is defined as

$$I = \frac{E_{pulse}}{\tau S} = \frac{P_{peak}}{S}$$

with S area of the spot size, usually taken as the distance between the points where the intensity is decreased by a factor $1/e^2$, and E_{pulse} is the energy of a single pulse. It is then clear how high intensity can be reached, i.e. increasing the energy, reducing the duration, or tightly focusing the laser. The invention of the Chirped Pulse Amplification (CPA) technique in 1985 by G. Mourou and D. Strickland [2], awarded with the Nobel Prize in Physics in 2018 [3], allowed to drastically increment the achievable E_{pulse}. Amplification from nJ to kJ was demonstrated, delivering powers of TW or even PW. Intensities of 10^{14} W/cm^2 are not difficult to achieve, with a record up to date of 2×10^{22} W/cm^2. In Figure 1.3, taken from [4], the evolution over the years of achieved intensities is shown. It can be seen the role that CPA had in the development and also which optical regimes could be investigated at corresponding values.

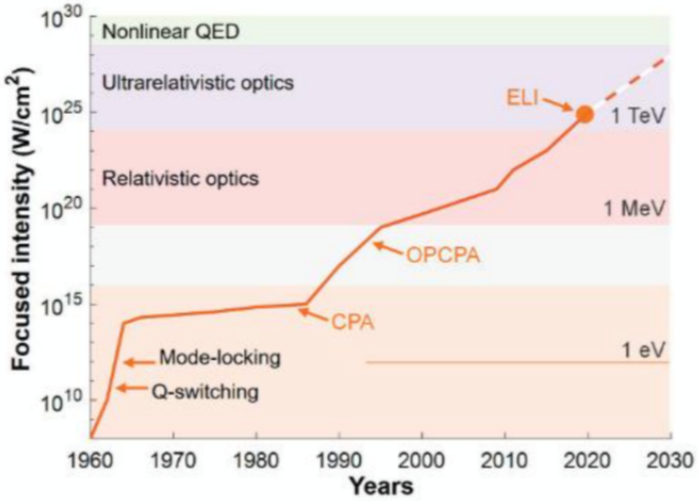

Figure 1.3. Development over the years of the highest intensities reached by lasers, from [4].

The main issues in amplifying a pulse are the possible damages to both the optic elements and the active medium, arising when too high intensity is achieved. CPA gets around such problem by increasing the energy while keeping the power low: the pulse is initially stretched in time and then, after amplification, compressed back to the original duration. To achieve the highest values reported above, in current laser systems, CPA is exploited along with a particular amplification strategy, that is Optical Parametric Amplification (OPA), giving OPCPA (Figure 1.4). In short, OPA exploits the energy transfer from an auxiliary electromagnetic wave, the pump, to the signal wave in a non-linear crystal.

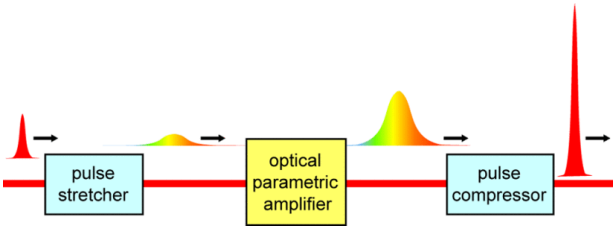

Figure 1.4. Scheme of OPCPA, from [5].

In real systems, the pulse time shape is not perfect and pre-pulses can arise from several phenomena, like amplified spontaneous emission or incomplete compression. When dealing with very high intensities, even having high contrast (i.e, the ratio between the intensity of the main pulse and the pre-pulse) could give really intense pre-pulses, that can strongly affect the system with which it interacts. This is particularly relevant in the field of particle acceleration, as the unwanted light that precedes the main pulse can influence or damage the experimental setup. To give an idea, typical contrasts can be of the order of $10^2 - 10^8$, that means, for a main pulse of 10^{20} W/cm^2, a pre-pulse of 10^{12} W/cm^2 at best. Several strategies are adopted in order to reach higher and higher contrast, for example the use of plasma mirrors and fast Pockels cells, with results greater that 10^{11} [6].

1.2 Laser-matter interaction

The interaction of a laser pulse with matter brings in a broad variety of phenomena, depending on the intensity regime. For example, non-linear effects become relevant when $I > 1$ GW/cm^2, and self-focusing of the wave during propagation can occur. In particular, in case of values of the order of $10^{13} - 10^{15}$ W/cm^2, ionization takes place and a plasma is formed. In this state, the behaviour of matter changes dramatically and its evolution strongly affects the further propagation of radiation. In laser-driven particle acceleration, the regime to consider is the one above 10^{20} W/cm^2, so its description not only needs to deal with electromagnetic waves in plasmas, but also to account for relativistic effects (see Figure 1.3). A detailed theory of such topics, which are very broad and can be really technical, is beyond the scope of this work. Nevertheless, at least the most elementary features of electromagnetic waves propagation in plasmas are needed in order to understand how acceleration of particles can take place. A vast bibliography on this is available; for example, Macchi [7] or Mulser and Bauer [8] are advanced references that deal specifically with the super-intense interaction. For this brief introduction, the material from the fifth chapter of Zavelani-Rossi and Vismarra [4] could be enough.

With plasma, one refers to a macroscopic state of matter, usually globally neutral, in which the concentration of charged particles is greater than the one of neutrals. It is the case, for example, of a (partially) ionized gas, where two charged populations can be identified: electrons and ions. Plasmas can be described in several ways, according to which features are to be highlighted and the degree of complexity needed. One of them is the charged fluids model, and it is considered in the following along with Gauss units.

In the simplest case, the dynamics of the ions can be neglected because of their greater inertia when compared to electrons (i.e., the mass ratio is $m_p/m_e \approx 1836$). Although being globally neutral, local fluctuations of charge arise due to the balance between thermal motion and electromagnetic forces, from which a characteristic length can be extrapolated:

$$\lambda_D = \sqrt{\frac{T_e}{4\pi n_e e^2}}, \tag{1.1}$$

where T_e is the electron temperature, n_e the electron number density and e the electron charge. λ_D is called *Debye length* and it sets the spatial scale over which variations in

concentration of charged species are possible. This separation of charge can be also considered dynamically, and so another fundamental plasma parameter is retrieved: a characteristic oscillation frequency, called *plasma frequency*.

$$\omega_p = \frac{1}{\lambda_D}\sqrt{\frac{T_e}{m_e}} = \sqrt{\frac{4\pi n_e e^2}{m_e}} \tag{1.2}$$

In this last expression, the thermal velocity $v_t = \sqrt{T_e/m_e}$ can be identified and, keeping in mind what λ_D represents, the physical meaning of ω_p is highlighted. It can be interpreted as the frequency at which the system, perturbed from equilibrium, collectively oscillates due to the arisen electric field that tries to restore such equilibrium. Note the dependence on the mass: the reciprocal of this quantity is a natural response time and ions' is much slower due to their mass, confirming the initial consideration. In practical units, $\omega_p[\text{rad/s}] \approx 5.6 \times 10^4\, n_e^{1/2}[\text{cm}^{-3}]$.

At this point, the propagation of electromagnetic waves in plasmas can be addressed. In the simplest case, monochromatic waves with wavevector $\mathbf{k}$ and frequency ω can be considered. Considering the plasma, some simplifying assumptions can be made, namely single fluid, cold (i.e., neglecting spatial dispersion as $\omega/c \gg v_t$), non-collisional and without external magnetic field. Moreover, considering *linear response*, the dispersion relation for transverse modes can be retrieved:

$$\omega^2 = \omega_p^2 + c^2k^2. \tag{1.3}$$

Longitudinal modes at $\omega = \omega_p$ are also found: they are exactly the one related to the meaning of plasma frequency, that is stationary oscillations.
Referring to Figure 1.5, it is immediately seen that not all frequencies can propagate in a dispersive media like a plasma: a minimum admitted frequency exists and it is ω_p, which acquires the new meaning of *cut off frequency*. Then, two regions can be identified. For $\omega > \omega_p$, waves can propagate with a group velocity that starts from zero and tends to c, because at frequencies much higher than characteristic one, even the rapid electron population cannot follow the field oscillations, behaving like vacuum. For $\omega < \omega_p$, waves cannot propagate and are exponentially dumped and/or reflected due to the internal electric field that arises from charge separation. In this latter regime, a characteristic length that describes the penetration distance of a monochromatic wave in a plasma can be found and is called *skin depth*. It is

$$l_{sd} = \frac{c}{\sqrt{\omega_p^2 - \omega}} \tag{1.4}$$

and it is interesting that in the limit of low frequency it does not depend on it anymore.

Taking into account a certain wave or pulse, it is useful to know in which plasmas it can propagate. So, it is common to revert Equation 1.2, expressing the density in terms of ω_p. The *critical density* is then defined with the meaning of edge value between propagation and absorption.

$$n_c = \frac{m_e\omega^2}{4\pi e^2} \tag{1.5}$$

In practical units it can be written as $n_c[\text{cm}^{-3}] \approx 1.1 \times 10^{21}/(\lambda[\mu\text{m}])^2$. To summarize, three regimes are possible:

- $\omega < \omega_p$ or $n > n_c$, called *overcritical* or *overdense* plasma, in which the electromagnetic wave can *not* propagate;
- $\omega > \omega_p$ or $n < n_c$, called *undercritical* or *underdense* plasma, in which the electromagnetic wave can propagate;
- $\omega \approx \omega_p$ or $n \approx n_c$, called *near critical* regime, in which a more complex, intermediate behaviour with strong coupling between the electromagnetic wave and the plasma is observed, leading to volumetric absorption.

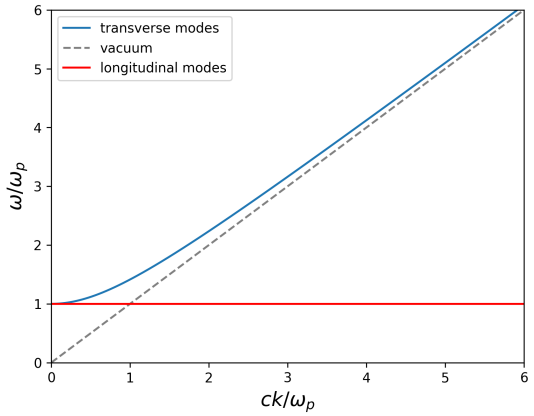

Figure 1.5. Dispersion relation of electromagnetic waves in a plasma.

As previously stated, at very high intensities, like the typical ones of particle acceleration, relativistic effects have to be taken into account. Without entering in too many details, for transverse wave propagation it is possible to write an analogous to the dispersion relation. Keeping in mind that the description is strongly non linear and correcting with the $\gamma = (1 - v_e^2/c^2)^{-1/2}$ factor, along with a new expression for the critical density:

$$\omega^2 = \frac{\omega_p^2}{\gamma} + c^2 k^2; \tag{1.6}$$

$$n_{c,r} = \gamma n_{c,nr} = \gamma \frac{m_e \omega^2}{4\pi e^2}. \tag{1.7}$$

Two very interesting phenomena can be forecast. Since γ is greater than one, the critical density is increased. As a consequence, regions where, classically, propagation is prohibited, are accessible thanks to relativistic effects. This is called *relativistic self-induced transparency*, because the propagation of the wave induces relativistic motion of electrons that in turn can make further propagation possible. The second phenomenon is *relativistically induced self-focusing*. As the refractive index of the plasma ($N = (1 - \omega_p^2/(\omega^2\gamma))^{1/2}$) is increased by the propagation of an intense radiation, because of its dependence on the γ, a situation in which such high index region is surrounded by a lower index one (the unperturbed plasma) arises, which is analogous to the one of optical fibres (internal reflection).

In order to understand the laser plasma interaction, a final, general ingredient is needed. Studying the interaction of an electromagnetic field with a charge and

accounting for first order non-linearities (amplitude of the fields not small), an effective force is found. It is called *ponderomotive force* and its non-relativistic expression is

$$\mathbf{F_p} = -\frac{e^2 n_2}{4 m_e \omega^2} \nabla |\mathbf{E}|^2. \tag{1.8}$$

The motion of particles is then characterized by a rapid oscillation at the field frequency plus a drift due to ponderomotive force towards *regions of low intensity field*. Note that it is independent of the sign of the charges and inversely dependent on the mass, making it much more effective on electrons than ions. Furthermore, it can be seen as proportional to an interesting parameter called laser irradiance, $\lambda^2 I$, that tells how to get strong forces: high intensity with a sharp spatial profile (gradient) and/or long wavelength. To extend it to the relativistic case, it is useful to introduce the electromagnetic vector potential $\mathbf{A}$ ($\mathbf{E} = 1/c \cdot \partial \mathbf{A}/\partial t$) and its normalized modulus, $a_0 = eE/m_e c^2$. In fact, $a_0^2 \propto \lambda^2 I$ and it allows to write the γ factor as

$$\gamma = \sqrt{1 + a_0^2/2}. \tag{1.9}$$

So, the value of the normalized vector potential sets the relativistic limit: when it is $\ll 1$, the non-relativistic approach is sufficient, while for $a_0 \sim 1$ or greater, relativistic effects must be taken into account. Again, to have an insight of which intensities are high enough for relativistic effects to happen, a_0 can be expressed in practical units:

$$a_0 = 0.85 \sqrt{\frac{\lambda^2[\mu m] I}{10^{18}\ \mathrm{W/cm^2}}}. \tag{1.10}$$

Lastly, the relativistic ponderomotive force is given by Equation 1.11.

$$\mathbf{F_p} = -m_e c^2 \nabla < \gamma > \tag{1.11}$$

The extension to the case of a plasma (so a population of charges instead of a single one) can be obtained, although not rigorously, by multiplying the forces by the number density, giving what can be interpreted as the push of charges toward regions of low electromagnetic pressure.

What has been discussed so far applies to monochromatic waves, but holds also for pulses. Focusing on the temporal profile, the ponderomotive force due to the leading edge of the pulse pushes electrons forward in the propagation direction. That leaves uncompensated positive charges, whose response is much slower, and an electric field arises. As a consequence, plasma oscillations at ω_p are induced. Then, the trailing edge of the pulse comes into play, and the ponderomotive force now pushes electrons backwards, enhancing the coulombian restoring force (Figure 1.6). In resonance condition, i.e. for period $T_{pulse} = T_{plasma}/2 \approx \pi/\omega_p$, these oscillations can be strongly amplified, and the process can be seen as a conversion from a transverse to a longitudinal mode. Of course, this description is valid when the pulse do propagate in the plasma, i.e. in underdense regime (in a general sense, considering also relativistic transparency). Electrons that are expelled from the laser pulse form a plasma wave, called *laser wake*, as depicted in Figure 1.7. The charge separation originating between the back of the wake, where electrons concentrate, and the middle, where still ions

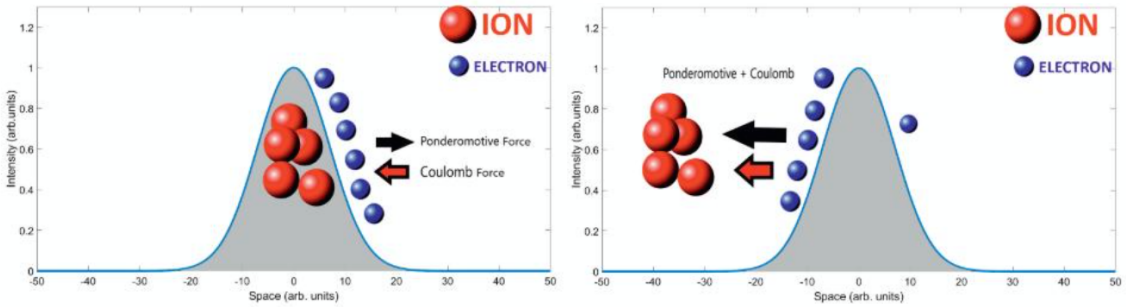

Figure 1.6. Pictorial representation of the propagation of a laser pulse in a plasma, from [4].

reside, is so strong that it can accelerate bunches of electrons in the forward direction, riding the plasma wave and reaching energies up to GeV in one cm. This mechanism of electron acceleration, called *laser wakefield acceleration*, is mostly effective for $T_{pulse} < T_{plasma}$ towards resonance, and continues until wave-breaking occurs.

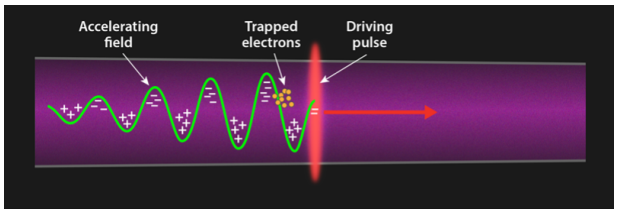

Figure 1.7. Schematic representation of laser wakefield acceleration, from [9].

In the case of an overdense plasma, like the ones generated by solid thin films, the laser pulse cannot penetrate beyond the skin depth and the energy absorbed from it is transported inside the plasma by very energetic electrons, called *hot*. These are of fundamental relevance in the context of ions acceleration because, as will be clarified in the following section, they are at the core of the process. The production of hot electrons is a process not completely understood and it can take place through different mechanisms. The main models describing them are the following:

- In non-relativistic regime (i.e., $I < 10^{18}$ W/cm^2), *inverse bremsstrahlung absorption* and *resonant absorption* dominate. The former is a collisional process between electrons and ions' field during which they absorb energy from radiation. Such mechanism is strongly dependent on electron energy and laser intensity, and so it becomes less important as these two quantities increase. On the other hand, resonant absorption is possible only when the laser is P polarized. It is due to Lorentz force at plasma interface, which induce plasma waves that in turn accelerate the electrons.

- In relativistic regime (i.e., $I > 10^{18}$ W/cm^2), that is the most relevant for this work, the main mechanisms are *Brunel effect* and the so-called $\mathbf{J} \times \mathbf{B}$ *heating*. As before, the first is active only for P polarized waves, because an electric field component along the normal to the plasma surface is needed. Such component of the laser extracts electrons toward vacuum and then re-accelerate them back into the plasma after an half period. In case of S polarized waves, or of normal

incidence, the dominant heating is due to the magnetic force which drives oscillations, analogous to the one described for Brunel effect.

As it should be clear, more than one of these mechanisms can take place simultaneously, depending on the plasma and laser parameters (intensity, polarization, density). In the case of a near critical plasma, the variety of phenomena interplaying in determining how the interaction occurs is vast, but, as anticipated, an efficient volumetric energy absorption is expected. As it will be clear in the following of this work, this paves the way for an efficient conversion of laser energy into electrons' and then ions' [10].

1.3 Acceleration mechanisms

Energetic protons and ions from laser interaction with solid matter, except for some low intensities experiments [11, 12], have been reported for the first time in the year 2000 by three independent works [13–15]. Directional proton bunches with energies in the MeV range were observed. Interestingly, the emission seemed to come from the non-irradiated surface, the rear one. One of the main concerns was, then, to understand how such particles were produced, if they were accelerated near the front surface and then crossed the material to the rear, or if they were directly accelerated at the back. Experiments evidenced that both the processes happen, but the latter is the most relevant. Various mechanisms that could explain such observations of laser-driven ion acceleration in solid targets have been proposed, among which Target Normal Sheath Acceleration (TNSA), Radiation Pressure Acceleration (RPA) and Coulomb Explosion (CE), also according to laser parameters as intensity and duration (see Figure 1.8) [16]. Nevertheless, the most established and consolidated physical model is TNSA, elaborated and proposed at first by Wilks et al. [17]. This acceleration schemed will be described in more details, although only qualitatively, in the next section.

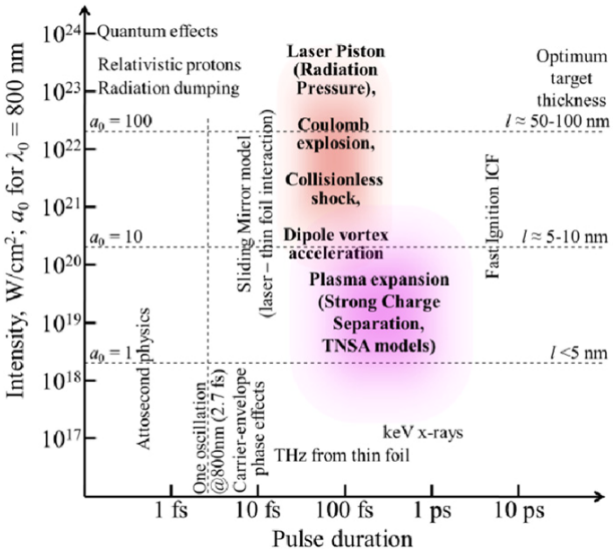

Figure 1.8. Representation of the possible regimes and describing models as a function of pulse intensity and time duration, from [16].

1.3.1 Target normal sheath acceleration (TNSA)

As depicted previously, the interaction of an intense laser pulse with the solid material forms a plasma. A very high current of hot electrons with an energy spectrum related to the laser intensity is generated and, for targets thinner than their mean free path, it can eventually reach the rear side. Then, if electrons cross the back boundary and escape in vacuum, the charge unbalance generates a sheath field E_s, normal to the rear surface. To estimate the magnitude of such field, a balance between electrostatic and electrons thermal energies can be written. So, considering an electron temperature T_e and a sheath extension roughly equal to Debye length, it reads

$$eE_s\lambda_D \sim T_e. \tag{1.12}$$

An expression for the temperature is also needed: keeping in mind that the heating process can be attributed to the effect of ponderomotive force, at first approximation

$$T_e \sim m_e c^2(\gamma - 1), \tag{1.13}$$

because $\mathbf{F_p} = -\nabla U_p$ (see Equation 1.11). Finally, recalling the expression of γ and a_0 scaling (Equation 1.9 and Equation 1.10), for a laser with $\lambda^2 I = 10^{20}$ W/cm^{2}µm^2, electric fields $E_s \approx$ MV/µm are foreseen.

It is in this very strong field that the origin of the proton acceleration is found: a positively charged particle crossing it would acquire an energy of $\varepsilon_i \sim ZeE_s\lambda_D \sim ZT_e$, which is really in the MeV range, over a distance in the order of µm. Because of the directionality of such field, the resulting beam would be highly collimated, an interesting feature of this particle source.

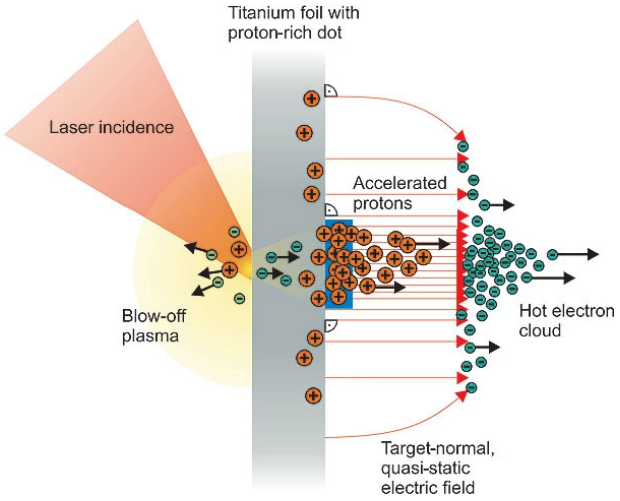

Figure 1.9. Schematic representation of TNSA, from [18].

The accelerated protons that are considered come from a thin layer of contaminants that contains hydrogen, present on the rear surface, i.e. at the maximum field position. Heavier ions can be accelerated much less effectively, mainly because protons, much more rapid thanks to lower inertia, will screen the sheath field. Nevertheless, it do is possible to accelerate them on a longer time scale, provided that the proton content is low enough to not balance the charge of the escaping electrons. This can be typically achieved by cleaning the target from contaminants, for example by heating it [19].

With this considerations, a scaling law for the TNSA mechanism has been found: proton energy, which is directly proportional to the sheath electric field and so also to hot electrons temperature, increases as $(\lambda^2 I)^{1/2}$ due to γ and, in turn, to a_0. Maximum proton energy experimentally recorded versus irradiance is presented in Figure 1.10 for several laser systems. It can be observed that a slower linear scaling with the irradiance seems to be valid for short pulse durations. As anticipated, several different mechanisms, besides TNSA, are possible and so also different laws could be possible. Identification of scaling of proton acceleration with various parameters, possibly also referred to the target, is crucial, because it can guide in the further development of the field and in improving the beam characteristics.

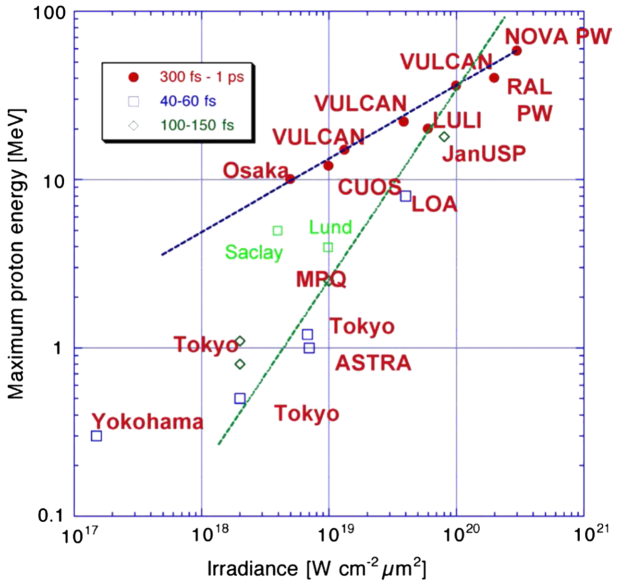

Figure 1.10. Maximum proton energy from solid targets as a function of the laser irradiance in three ranges of pulse durations. The scaling is represented with the two trend lines, from [20].

TNSA-generated proton beams are produced in bunches and are typically characterized by a broadband energy spectrum up to a cut off energy, whose value scales as discussed and can be approximated by a quasi-thermal distribution, a property that is usually not too good for applications. On the other hand, their spatial and angular characteristics are really promising, thanks to smooth proton beam profiles with a sharp boundary and a high degree of laminarity.

As it should be clear, the treatment presented in this section is not only qualitative, but also just introductory and far from exhaustive. A lot of texts, both books and articles, about the theoretical description of acceleration physical models are available; for example, [16] or [20] deal generally with the topic, while [21] is specifically about to TNSA.

1.4 Potential applications of laser-driven sources

Coming to an end of this first, introductory chapter that addressed laser driven particles acceleration, an overview of the potential applications of such a technology can be given. As anticipated, laser accelerated ions have peculiar properties that distinguish them from the conventional sources, but not all of them are desirable for some applications. In addition, achieving good shot to shot reproducibility is not so trivial. Despite that, the already identified possible ways of exploiting such source can also guide their development, while some unpredicted uses could be thought in the future.

A description of the employments of protons and ions by lasers can be found in most of the reviews on the topic, among which the already cited ones [16, 20, 22]. In this section, a brief summary of the main ones is given.

Experimental physics. In the field of experimental physics, potential applications could be in the production of warm dense matter, for which high energy flux and short temporal duration are needed. This technology could also enable the performance of nuclear and particle physics experiments in laser laboratories rather than in accelerator or reactor facilities. As an example, spallation reactions and intranuclear cascades studies could benefit from the broad energy band of these sources [23]. With regards to particle physics, instead, energies today inaccessible, but that could be achievable in the future, are needed. In particular, pions could be produced with a flux much higher than conventional accelerators one and, given their finite lifetime, the high field acceleration consequent to laser-driven production is of much interest [24].

Materials science. In materials science, the accelerated protons can be employed as a characterization probe for ion beam analysis techniques, such as Particle Induced X-ray Emission (PIXE) and Proton Induced Gamma-ray Emission (PIGE), for which MeV energies are need. Both numerical [25] and experimental [26] results have been obtained. Moreover, the radiation from laser-driven sources, thanks to the broad spectrum and the presence of various kinds of particles (electrons, gamma rays), can be very useful in radiation damage research, for example in materials for space applications or harsh radiation environments. Proton radiography, a technique that exploits the interaction of protons with a sample to probe it, is also possible. The particle beam is sensitive to material density through its energy losses, and to electric and magnetic fields due to the deflection they cause. The source characteristics such as short duration, high degree of laminarity and small source size allow observing fast dynamic phenomena with high resolution like the ones occurring in plasmas.

Inertial fusion research. In the context of inertial confinement fusion, one advanced strategy is the so-called fast ignition. In this scheme, ns laser beams compress a target to make a core plasma and, then, a shorter ignitor beam made of ions burns the fuel. Thanks to this separation of compression and ignition, the requirements of high symmetry typical of the conventional inertial fusion experiments can be relaxed. Laser-driven particles could be effectively exploited as ignitor because of their short time duration and high-intensity [27].

Neutron and radioisotopes production. If the maximum energy of the proton beam is larger than several MeV, one can use it for driving nuclear reactions through interaction with a secondary target. Radioisotopes for medicine, or neutrons for radiography, transmutation or cancer therapy could be produced. For such applications, the main issue is the yield of protons with energy higher than the threshold of the reaction, but potentially, laser-driven neutron beams could offer several advantages compared to conventional sources as cost, compactness, brightness, and short duration.

Biomedical applications. Besides the possibility of producing radionuclides, already mentioned before, particles can be exploited in hadron therapy. This technique consists in employing hadrons (protons, carbon ions) to deposit energy in the cancer tissue. The advantage of this therapy is in the way heavy charged particles lose energy when interacting with matter, i.e. mostly in a well localized region, called Bragg peak. The range is determined by the initial energy of the particle, and ,so, a fine tuning of it allows to drastically reduce unnecessary dose absorptions. To give an idea, the energy window of therapeutical interest for protons ranges between 60 and 250 MeV. The use of laser-driven accelerators could have potential advantages in terms of compactness and costs, but much effort is still required for them to meet therapeutic specifications. The main needed improvements reside in the maximum energy, the energy spectrum (ideally, a monochromatic or fine-tuned spectrum is required), the repetition rate and, in general, reliability. Finally, it can be cited that another cancer treatment could make use of these kind of sources, if a neutron conversion scheme is adopted: Boron Neutron Capture Therapy (BNCT) exploits the capture of a neutron by the tumour previously enriched with ^{10}B.

Industrial applications. In the industrial sector, two possible uses of such beams can be foreseen. One is the thin layer activation, which allows to measure the wear or corrosion of machine parts or tools. Their surface is activated, controlling the depth through the beam energy, and the activity evolution provides information on the amount of removed material with a quite high sensitivity [28]. The second one is laser-driven ion implantation which has several advantages over other techniques, for example a greater depth of implantation [29].

These examples show how wide is the range of fields that could potentially benefit from the development of laser-driven acceleration technology. Much improvement has been done and continues to be. As it was clear since the first experimental observations, the choice and design of the targets employed not only affects the beam characteristics and so offers a way to control them, but also a proper engineering of them allows to reduce lasers demands. The second chapter will then address the topic of targets for laser particle acceleration, thus clarifying the goals of this work.

Chapter 2

Targets for laser driven ion sources

This chapter is devoted to the presentation of the other main ingredient of laser particle acceleration, besides the laser itself: the target. Its importance, highlighting the role it has in controlling the radiation source properties, is described in section 2.1. Then, an overview of the possible concepts and designs that are or could be adopted, also in relation to the required needs, is given in section 2.2 and section 2.3, with a particular focus on Double Layer Targets (DLTs). To conclude, the challenges and difficulties in the production and the implementation of such targets are stressed in section 2.4, giving the opportunity to point out which are the motivations and objectives of this thesis work in the final one.

2.1 Role of target in laser-driven acceleration

The maximum achievable ion energy, as discussed in section 1.3.1, scales with the laser parameters, like intensity. Consequently, much of the improvement in the field had followed the way of increasing laser performances. But maximum ion energy is not the only characteristic of interest. For example, PW level laser systems allow to reach very high energies but, on the other hand, they are characterized by extremely low repetition rates (few shots per day), that in turns mean very low average fluxes. Such facilities are extremely expensive and their main use is devoted to nuclear fusion and extreme matter studies. So, another strategy should be more suitable if the goal are other applications (see section 1.4). It consists in reducing the laser power to TW along with time duration (down to few fs) and increase the focusing. Systems of this kind can reach repetition rates up to kHz and average currents or particle fluxes needed for applications could be achieved [30]. In addition, lasers up to tens of TW can be particularly compact, fitting in a room, and thus they could be easily accessible for universities, research centres and industry.

To aim at applications, it is crucial for the sources to be stable and reliable. However, shot to shot reproducibility in high repetition rate operation could be quite difficult to assure. Thus, along with the development of adequate laser systems, suitable targetry and diagnostics must be developed. In fact, the target properties and design are as fundamental as the laser source in defining the beam performances and advanced engineered ones could make feasible to develop effectively compact and relatively cheap systems. Some relevant target characteristics are, for example,

the aggregation state, the density, the thickness... Because laser-solid interactions are sensitive to perturbations of the order of the laser wavelength, high precision in fabrication is needed for most targets. Therefore, developing and validating a new design often requires extensive research. Not only, targets are usually destroyed in the interaction with the laser pulse and so they must be replaced at every shot with micron level precision in positioning. Furthermore, the ablated material can coat optics elements and generate electromagnetic pulses (EMP). Having in mind such scenario, several supporting technologies has to be considered, such as fast target refreshing, positioning and alignment systems or real time target characterization.

It should then be clear the relevance of target research and, since the first experiments, many designs have been proposed, also according to the phenomena investigated, the laser parameters adopted and the diagnostics employed. The variability is huge: they can be in different states of matter, sub-micrometric or millimetric in thickness, homogeneous or structured, planar or 3D. As long as the production of secondary radiation as electrons, ions or photons is concerned, the main approach has been focused on investigating, exploratorily, the basic physics and possible improvements in the source properties.

While some target concepts can be considered as established, others still need much development. In the following of this chapter, some configurations are addressed, making a distinction between conventional, exotic and advanced solid-state designs, mainly Double Layer Targets (DLTs) because of their relevance for this thesis work. The article from Prencipe et al. [31] is used as main reference.

2.2 Conventional and exotic targets

In this section, the basic target strategies are discussed following a classification based on the aggregation state (i.e., gaseous and solid), while in the last section other exotic or less common types are briefly presented, like fluids, gels and cryogenics.

2.2.1 Gas targets

Gas targets are particularly suitable for electrons acceleration and X-rays production thanks to their low density. Indeed, electron densities characterizing this state of matter are about $10^{16} - 10^{19}$ cm^{-3} and so it generates a plasma that is well underdense (see Chapter 1), allowing for laser propagation. Thus, wakefield acceleration driven by ponderomotive force, described in section 1.2, can take place. Moreover, pulses of X-rays with fs duration are emitted because of various mechanisms, like electron (betatron) oscillations, which occur during the electron propagation [32]. Electrons with energies over 1 GeV can be obtained [33]. The most employed gaseous targets are gas jets, gas cells and discharge capillaries.

Gas jets. These are the most common targets for laser electron acceleration. They consist of a small chamber which is filled with a gas (He, Ar, N_2...). A nozzle allows to get a controllable and laminar flux from it, reaching supersonic speeds, while background pressure can tune the gas density. Gas jets are characterized by electron densities on the high end of the previously stated range ($10^{18} - 10^{19}$ cm^{-3}), which

is not the best as long as maximum electron energy is concerned. Critical issues of such targets are related to the possibility of damaging the nozzle through the plasma plume, along with the durability of magnetic valves, which are needed to synchronize the jet with the laser pulsed. A typical experimental setup is shown in Figure 2.1.

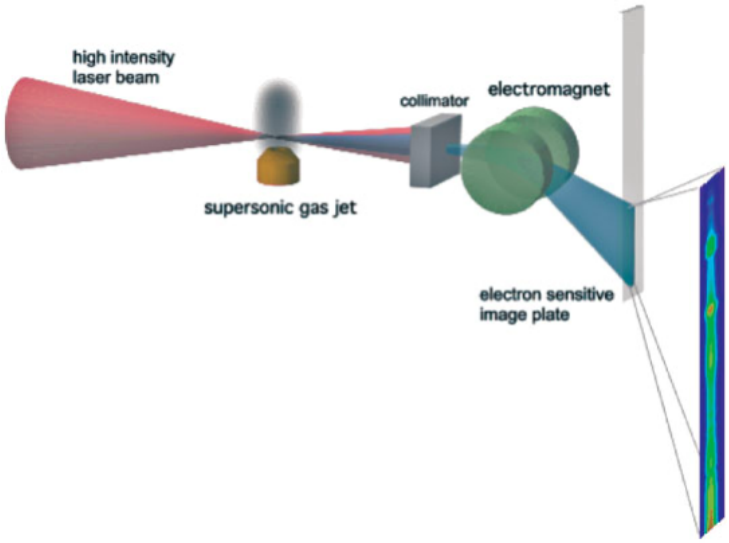

Figure 2.1. Experimental setup of laser-driven electron acceleration. An electromagnet is used to characterize their spectrum, from [33].

Overdense gas jet targets have also been studied to get laser-driven ion acceleration. Indeed, energies achievable with low density jets are below one MeV, while for values higher than 10^{21} cm^{-3} it could be possible to reach higher ion energies thanks to an acceleration mechanism based on a propagating shock wave, generated by the laser pulse [34].

Gas cells and discharge capillaries. Gas cells are introduced because they allow to reach lower densities ($10^{16} - 10^{18}$ cm^{-3}) and longer propagation lengths (cm instead of mm), thus increasing the achievable electron energy. Nevertheless, it is difficult to keep the pulse focused over the whole gas cell length, and so their use is limited to PW systems. Gas cells are small chambers, filled with gas, with two apertures to let the laser in and the electrons out. They can work at high repetition rate and if their length is controlled, particles energy can be tuned. In Figure 2.2, an example of gas cell target is presented.
To overcome the limitation due to laser defocusing in lower power systems, discharge capillaries waveguides have been developed. They consists in tubes of alumina or sapphire of hundreds of microns diameters filled with gas through holes drilled at each end. A pulsed discharge is used to ionize the gas and control plasma density, which is minimal along the capillary axis ($10^{17} - 10^{18}$ cm^{-3}). In this way, good laser focus can be kept through the whole length. The fabrication techniques employed for discharge capillaries are consolidated, but particular attention to the internal surface roughness must be paid, in order to prevent light scattering and damages, thus assuring their integrity at high repetition rates.

Figure 2.2. A photograph of an adjustable length gas cell developed by SourceLAB, from [35].

2.2.2 Solid targets

The interest in solid targets is mostly for ions acceleration. As already described in section 1.3.1, the main acceleration mechanism is the TNSA one, in which the electric field due to charge separation drives contaminant protons' acceleration (or heavier ions), producing a collimated beam of bunches. In the first three pioneering experiments already cited [13–15], simple solid state foils of aluminium or polymeric material were used, whose thicknesses ranges between $1 - 125$ μm. Such thin foils of different materials are particularly useful in investigating some dependences of the proton beam on the target characteristics, above all thickness, also in relation to different laser parameters. In Figure 2.3, an example of the behaviour of the cut-off proton energy as a function of Al target thickness and for two different laser contrast scenarios is shown. It can be seen that an optimal value exists, along with a very strong dependence on the pre-pulse intensity and laser contrast [20]. It is not too surprising that in thinner targets achievable energies are higher, because the hot electrons have to travel less inside the material and have less space to spread, meaning, in turn, higher densities at the rear surface and so greater fields.
Parametric scans in foil thickness also allow the investigation of the transition between different dominating acceleration mechanisms. It is found that TNSA is most relevant for μm and sub-μm targets, while for thinner ones, i.e. $10 - 100$ nm, other processes arise, such as RPA [20], although high contrast is required to avoid target destruction by pre-pulse. Indeed, it has to be pointed out that laser contrast requirements generally depends on the target properties, such as its thickness.

This kind of targets can be commercially available and so, in that sense, they can be considered conventional, at least for given values of the relevant parameters. When their thickness is of several μm, such foils are produced by mechanical rolling, but the tolerance on the nominal value can be high, leading to local variations not negligible in acceleration experiments and thus resulting in less reproducibility. On the other hand, for thinner films (less than 1 μm), Chemical Vapour Deposition (CVD) or Physical Vapour Deposition (PVD) techniques are employed for metallic materials, while spin coating can be adopted for polymeric ones. To overcome the limitations of these simple targets, and to improve their effectiveness in delivering ion beams, a lot of engineered solid targets have been proposed and will be presented as more advanced design in section 2.3.

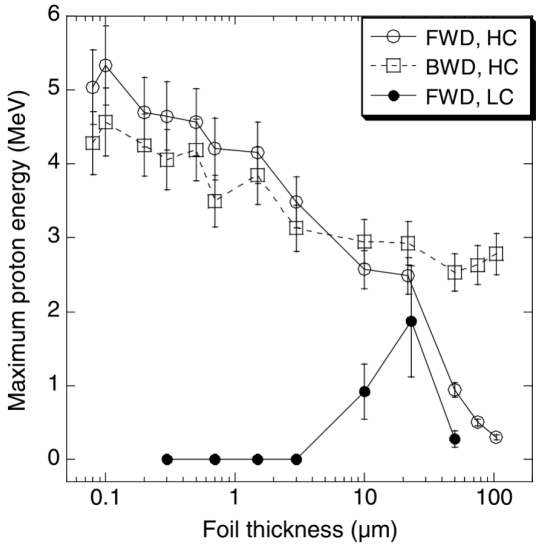

Figure 2.3. Variation of maximum proton energy as a function of *Al* target thickness. FWD means forward direction and BWD backward direction. Data for laser contrast of 10^{10} and intensity of 5×10^{18} W/cm^2 in the HC case, and 10^6 and intensity of 10^{19} W/cm^2 in the LC one are presented. From [36].

2.2.3 Other types of targets

Several other strategies exploiting peculiar targets can be found in literature. For example, tape-drive targets produced MeV proton beams at few Hz of repetition rate [37]. Thicknesses of about 10 μm were employed, but reducing it to increase maximum proton energy is quite difficult because of tearing.
Liquid state materials could also serve as targets in form of droplets: they have the advantage of being on the scale of the laser focus and electrically isolated from their surroundings, thus improving the conversion of laser energy to energetic ions [30]. Liquid jets have been investigated [38] too, leading to few MeV protons.

Another option is the use of liquid crystal films, which are produced directly in the interaction chamber thanks to a sliding blade that sets the delivered volume (see Figure 2.4) [39]. The thickness of these targets can range from a few nm to some μm, according to the blade speed. Nevertheless, a fine control at very small values is quite challenging and this poses some question on the stability of such targets. In addition, the incorporation of high Z elements in liquid crystals is not trivial.
Despite being originally developed for inertial confinement fusion experiments, cryogenic targets allow to study laser-driven ion acceleration with pure solid hydrogen or deuterium. They can be produced through several techniques, like condensation, extrusion or in form of liquid jets.

Lastly, foam targets should be mentioned. Porous materials present low average density, leading to an interaction regime that tends toward the near-critical one. This characteristic could be really helpful in increasing the coupling with the laser, making possible to reach higher proton energies. These can be produced through chemical techniques, like sol-gel polymerization, and can also be loaded with high Z elements in form of particles. A review of materials of this kind employed in laser-plasma interaction experiments can be found in [40]. Engineered targets based on low density

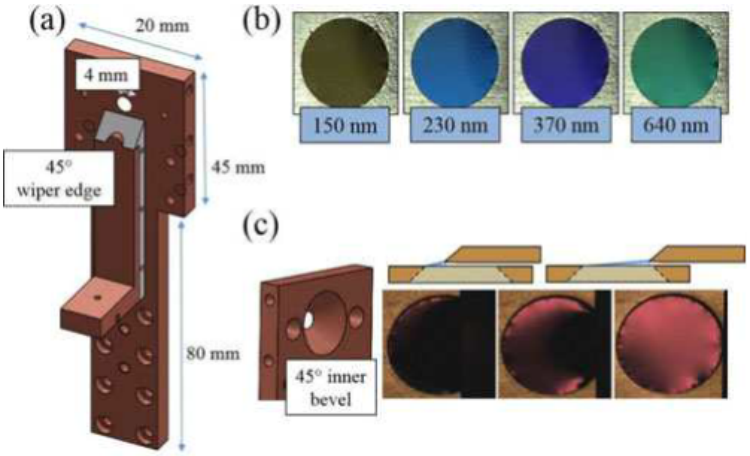

Figure 2.4. (a) View of the slider for liquid crystal film formation; (b) four films demonstrating thickness control; (c) representation of film formation. From [39].

materials have been investigated also in the form of films deposited through PVD (or also CVD) techniques. Such advanced designs are the main focus of the next section, where they will be described in detail.

2.3 Advanced solid-state targets

Solid-state targets, as previously stated, are mostly employed for protons and ions acceleration, though an increasing interest in them is arousing also for other particles, like photons and neutrons. In order to achieve beam characteristics more suitable for applications, a promising strategy is proper advanced engineering of such targets. In general, the goal is to enhance laser absorption and thus increasing the cut off energy and the particle flux. This can be done by properly modifying the front surface, or by changing the transverse dimension as in mass limited targets, as will be explained. A crucial aspect that has to be pointed out is the importance of very high contrast lasers, needed to avoid the destruction of the possible superficial features by the pre-pulse before the arrival of the main peak.

2.3.1 Overview of advanced strategies for solid targets

The advanced designs of solid targets generally has the goal of improving the characteristics of the produced particles or to obtain sources of different, like neutron ones. The general idea is to properly engineering the target so that a better coupling with the laser can occur. Here, some proposed concepts are presented.

A first kind of advanced solid targets is given by multiple layer targets with coatings on the non-illuminated side. For example, metallic foils with hydrogen-rich micro-dots with transverse size comparable to the laser focal spot area allowed higher yields of protons with a narrow energy spectrum [18]. Another type of multi-layer concept, in this case on the illuminated side, is the double layer target, that will be presented in detail in the following section.

Significant improvement in proton energy was observed with the so called reduced

mass targets: they consists of thin foils whose transverse size is limited to some µm, usually produced by lithographic techniques [41]. The idea behind such design is that with a reduced lateral dimension, electrons could be reflected at the surface, recirculating in the plasma. This allows to keep a denser and hotter electron sheath, leading to increased maximum ions energy and laser conversion efficiency (see Figure 2.5).

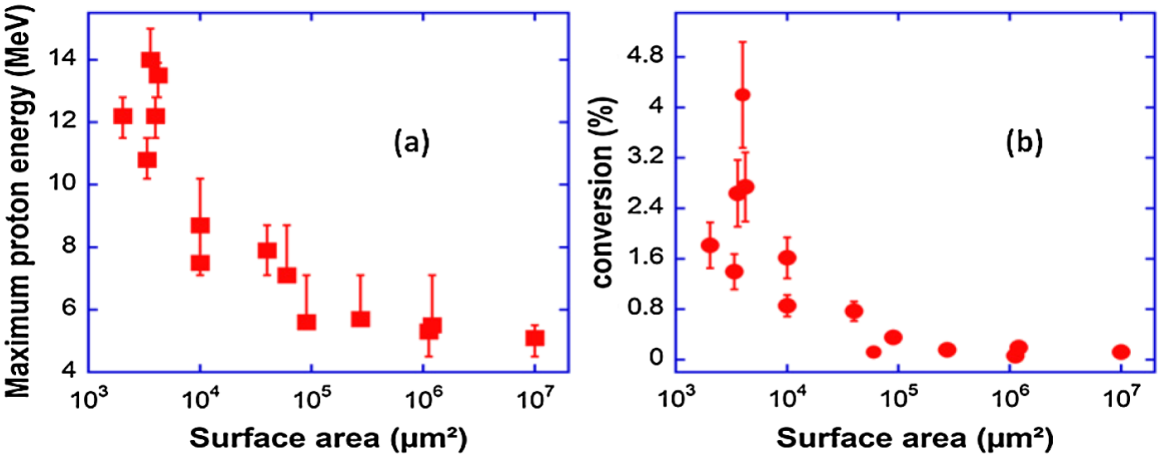

Figure 2.5. (a) Maximum proton energies for 2 µm thick Au targets of various surface area and (b) laser-to-proton energy conversion efficiencies (for protons with energy > 1.5 MeV). From [41].

It has also been observed that, considering that TNSA gives normally directed particles, the use of hemispherical or hemicylindrical targets can effectively alter the beam direction, allowing its control [42]. Lastly, for neutrons production, targets consisting in deuterated polyethylene, in which deuterium nuclei accelerated at the front can give fusion reactions with deuterium nuclei in the bulk [43], can be exploited. Alternatively, the use of the so-called pitcher–catcher configuration, in which a secondary converter target is introduced, is also advised.

2.3.2 Double layer targets (DLTs)

The target design which is the focus of this work will be here described, with the introduction of Double Layer Targets (DLTs). Despite the fact that also structured rear surface targets or other designs could be made of two layers, here this name is used to identify somewhat more specific. The basic idea is to coat the front surface of a conventional solid target, e.g. produced by rolling or with a suitable deposition technique, with a layer of low density and low atomic number material, for example carbon. An electron density close to the near critical one allows for better coupling with the laser pulse, resulting in volumetric energy absorption (see section 1.2). Moreover, dealing with a less sharp density profile, as it is in the case of a structured surface, can be beneficial for electrons heating. Mechanisms like laser focusing and channelling, as well as coulomb explosion, could also happen, helping hot electrons generation.

To have an idea of the required material densities, considering a typical Ti:Sapphire laser ($\lambda \approx 0.8$ µm), $n_c \approx 1.1 \times 10^{21} \times (\lambda[\mu\text{m}])^{-2} \approx 1.72\ \text{cm}^{-3}$, that means, for a

completely ionized media

$$\rho = \frac{n_c M_a}{N_A Z} \approx 5.8 \text{ mg/cm}^3. \tag{2.1}$$

For light elements (up to calcium), the ratio between the atomic mass and the atomic number is approximately equal to 2, so this value is a representative one. As it can be seen, it is an especially low mass density, about three orders of magnitude below solid-state one, and thus poses challenges in their realization. Some good candidates are nanostructured porous materials with a high void fraction, like nanotubes [44] or nanofoams.

Both numerical and experimental investigations of the positive effect of such a design in terms of energy and number of accelerated particles have been provided. In Figure 2.6, a comparison between experimental results in terms of maximum proton energy recorded for conventional solid foils and DLTs, as a function of laser intensity and for different polarizations, is presented. Here, the foam layer is deposited on the same aluminium foils, in terms of thickness, investigated as bare targets. It is clear that the presence of the foam layer increases the maximum energy at all intensities, with little dependence on the laser polarization. The number of accelerated particles is enhanced, too. It has been found that the thickness of the bulk solid layer does not affect much the achieved energy [45]. Instead, foam thickness do has an effect: an optimal value seems to exist, as shown in Figure 2.7.

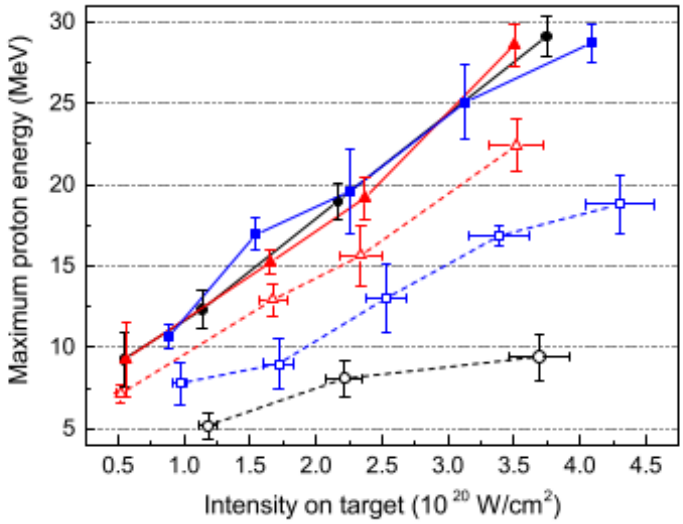

Figure 2.6. Maximum proton energy as function of laser intensity for several polarizations (s, blue squares; p, red triangles; c, black circles). Empty symbols refer to a 0.75 μm thick solid *Al* foil, while full symbols are associated to a DLT with 8 μm thick foam. From [45].

It should be recalled that, at sufficiently high intensities, even a foam slightly overdense could be seen as near-critical due to relativistic transparency, which enables the pulse to travel in the plasma and allows volumetric generation of hot electrons (see section 1.2).

Moreover, it has been found that the nanostructure of the illuminated surface can have great importance in determining how the laser interacts with the plasma [10,47,48].

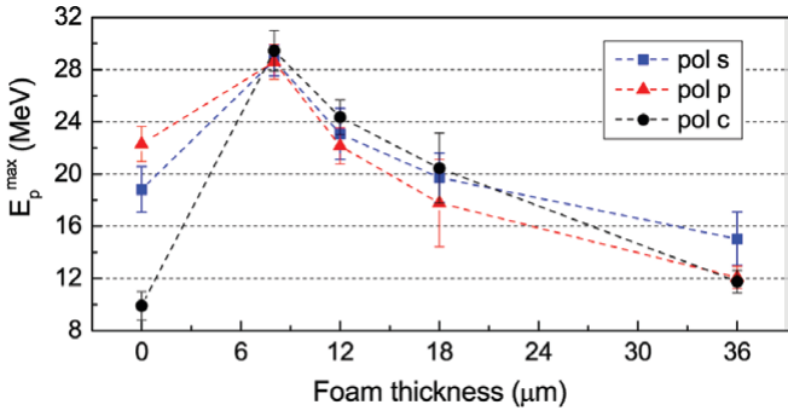

Figure 2.7. Maximum proton energy as function of foam thickness for different polarizations (s, blue squares; p, red triangles; c, black circles). The results refer to a DLT composed of 0.75 μm thick *Al* foils covered with $8 - 36$ μm thick foams. From [46].

As an example, in Figure 2.8 maximum proton energies resulting from numerical simulations of nanostructured and homogeneous DLT, along with conventional aluminium foils are presented.

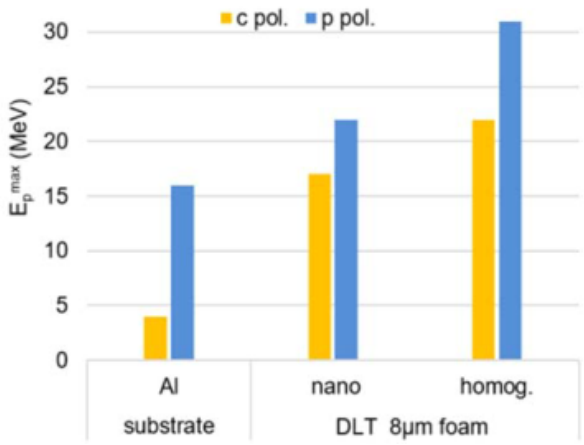

Figure 2.8. Simulated maximum proton energy from *Al* foil, DLT with nanostructured and homogeneous foam, using P- and C- polarized laser pulses. From [48].

A theoretical model describing ion acceleration through the interaction of a laser pulse with a DLT has been developed [49]. Although approximations valid only for homogeneous foams are assumed, it allows to compute reasonable estimates the optimal thickness and density as functions of laser parameters, along with prediction of maximum proton energies and enhancement factor with respect to single layer targets. These kind of targets are particularly appealing also because they enable the use of TW level lasers working at high repetition rates, and the characteristics of the obtained beams could potentially be controlled, at least partially, by tuning the properties of the low density layer. In this regard, a numerical investigation has been done as part of this thesis work and its results are presented in Appendix A. On the other hand, finely controlled production of DLTs poses several difficulties, addressed

in section 2.4.

2.4 Challenges in fabrication of advanced targets

Fabrication of solid targets for laser-driven acceleration experiments has to go through several steps, from design conception to manufacture of the single components and target assembly. All of these must be controllable and reproducible. In order to do this, target characterization (in terms, for example, of thickness, density, geometry, composition, crystalline structure, grain size, surface quality) is also crucial to check properties after every step. In addition, for commercial targets, after the development and characterization steps of the prototype are completed, also mass production scaling has to be addressed. In this case, analysis of each component can not be viable, and so automated systems for production, characterization and assembly has to be implemented.

Targets can be produced exploiting several techniques, some of which have already been pointed out in this chapter.Usually, multiple techniques are applied to produce a single one. In general, planar targets can be produced by PVD techniques such as thermal evaporation, e-beam evaporation, sputtering, Pulsed Laser Deposition (PLD), arc discharge coating, by CVD techniques, like atomic layer deposition or glow discharge polymerization or other techniques as electroplating, spin coating or spray-dry technique [50]. Lithographic procedures are also adopted (photolithography or electron beam lithography) to produce wafer-based targets. 3D targets are more complex and micro-machining is often adopted, while 3D printing could be of potential interest.

The adoption of a target in a real system requires several other elements such as a holder, the structures needed for alignment and positioning, systems for fast refreshing, along with protection parts of other targets from debris. A brief description of the main aspects to be considered and the challenges they pose in designing a system for laser-driven acceleration, in particular in case of high repetition rates, is given.

In the interaction of the intense laser pulse with solid matter, debris are produced. Along with material particles that could possibly damage the neighbouring targets and also the optical elements, a shock wave is sent through the surviving structure. The importance of such problems depends both on laser and target characteristics, like duration and energy or composition and size. The design of the target holder must then take into account problems of redeposition of evaporated material, protecting non-irradiated targets, but also laser interaction with it should be avoided.

Electromagnetic pulses (EMPs) are also produced as a consequence of laser-matter interaction. The problems related to them have to do mostly with electronics, which is needed for operation, control and characterization. EMPs impinging on electronic devices generates oscillating currents and can damage them and produce noise in detectors. Using shielded cables or shielding electronic devices can help in mitigating such unwanted effects.
Secondary radiation produced can induce nuclear reactions in the interaction chamber and thus materials activation. Back reflection of the laser pulse, with possible irreversible damage of the optical components could also happen.

After these general considerations, a specific configuration, main interest of this

thesis work, is described: the free-standing film on perforated holder. A thin film is free-standing when it is not in contact, at least in part, with a supporting structure. That is the case of a film deposited on a perforated holder like the one in Figure 2.9. Nevertheless, the most common use of perforated holders is still with solid foils clamped between the two side of it.

Figure 2.9. An example of perforated holder, adapted from [31].

The implementation of such a holder is useful because it allows multiple shots on a single target, also addressing partially the problem of possible damage to neighbouring, non-irradiated targets. On the other hand, it demands careful positioning and alignment. Some strategies to obtain such films can be found in literature; for example, the employment of standard photolithography, material layer deposition, selective etching and bulk silicon micro-machining [51, 52]. Miyamoto et al. [53], instead, proposed the use of a sacrificial support made of salt ($NaCl$), evaporated on a silicon substrate, on which a gold thin film could be deposited. After that, the soluble layer can be removed by dissolution in water and the floating metallic film is scooped up on a perforated holder. In this way, self-supporting thin films were formed on the apertures of the perforated holder.
One other procedure has been developed at NanoLab, Politecnico di Milano. Since it can be considered the starting point of this thesis, its description is left for the following section, in which a summary of the objectives of the work is given.

2.5 Context and goal of the thesis

Ions acceleration exploiting intense laser pulses is particularly appealing in view of the characteristics of the generated beams, but the application of this source still requires a lot of development. The design of the employed targets strongly affects the acceleration process. In fact, their proper engineering is a fundamental step in advancing such technology. Conventional solid targets in form of thin foils are usually produced by mechanical rolling, which leads not only to limited achievable thicknesses, but also to non-uniform ones, affecting reproducibility and control of the ion properties. In this regard, Double Layer Targets (DLTs) are promising candidates, in particular for compact TW laser systems. Nevertheless, their fabrication is not so straightforward. The front side layer should be made of an extremely low density material (about

6 mg/cm^3), in order to operate in the near-critical regime, enhancing laser-plasma coupling and electrons heating, which in turns determine higher ion number and energy. Nanostructured foams can be a valid option: they can be produced through PLD, employing different materials, and a first idea is to deposit it on a conventional metallic foil. In addition, the use of perforated holders as supporting structure of the targets for high repetition rate operation, poses some difficulties. The handling of the DLT and its clamping on the holder could easily break or crumple it, compromising the result.

For this reasons, a different way of realising a DLT has been thought at NanoLab, Politecnico di Milano. Instead of depositing the low density layer on a foil, both films can be produced exploiting PVD techniques, directly on the perforated holder. A free-standing film is thus obtained. The same procedure is also interesting for single layer, metallic targets, in particular at low thicknesses. The use of Magnetron Sputtering (MS) for the metallic film has been studied in a previous thesis work [54], exploiting both DCMS and HiPIMS. Attachment problems between target and holder are avoided, the film thickness can be tuned with much higher control and more uniform results can be achieved. Multi-elemental depositions are also possible. However, to be able to realise such a target, the perforation of the holder must initially be filled, and subsequentially freed from the filling material. Sucrose resulted adequate to this scope. Thus, the developed procedure consists of the following steps: firstly, a sucrose solution is pipetted in each hole; after solidification, the metallic film can be deposited according to needs; then, dissolution in water leaves the film free-standing; finally, the foam layer can be produced through PLD. The Figure 2.10 schematizes this process.

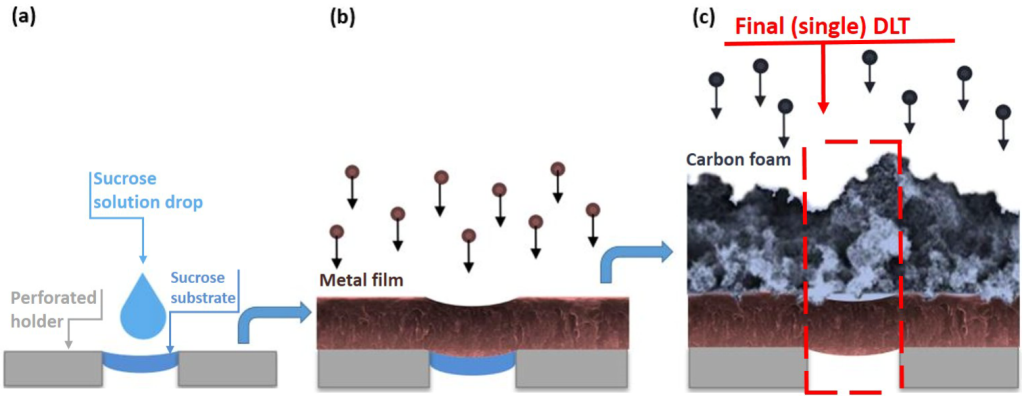

Figure 2.10. Schematic representation of the procedure for DLTs fabrication. (a) Perforated holder holes filling with sucrose; (b) metallic film deposition; (c) foam deposition and final result. From [54].

On the other hand, advancements in the study of carbon foam deposition through ns− and fs−PLD has been made, and models describing its growth developed [55]. Given the dependence of the accelerated beam properties on the nanostructure of the near-critical layer, the understanding of the relation between deposition parameters and morphological characteristics is of particular importance to achieve reproducibility.

This thesis works is located between the two sides of the development of such targets. The main goal is to investigate and understand the interaction of the two layers, also in relation to a real target holder, in order to produce a complete component.

Thus, optimization of the above described strategy is foressen. Then, the range of thicknesses that can be obtained, both for single layer and double layer targets, are investigated. The integrity and mechanical properties of metallic films, made of titanium, are thus studied, along with achievable foam characteristics. Another goal is to assess the dependence of foam adhesion on free-standing film thicknesses, along with the possible effects of some other properties.

The organization of the thesis is as follows. In Chapter 3, the main experimental tools that are exploited in the work are presented, namely Magnetron Sputtering, both Direct Current and HiPIMS, Pulsed Laser Deposition, with a focus on fs-PLD and the characterization techniques that are used. The ones that have been adopted are SEM, employed for morphological characterization, substrate curvature method, used to determine residual stresses, and Energy Dispersive X-ray Spectroscopy (EDXS), which can be used to compute mass thickness and density. Chapter 4 is devoted to the presentation of the deposited titanium films and carbon foams, in terms strategy, selection of the suitable deposition parameters and measured properties. The combination of the two and the main results for DLTs production are discussed in Chapter 5, while in Chapter 6 conclusions and future perspectives are presented. In addition to the experimental work, a numerical investigation on the properties of accelerated protons from targets with the characteristics described in this thesis and two laser configuration has been performed in the context of the ASPRI additional work, an high level training opportunity offered by the Politecnico di Milano; its results can be found in Appendix A.

Chapter 3

Experimental techniques

The experimental techniques employed in this work are here presented. In particular, as already anticipated, both the layers of the targets are obtained through Physical Vapour Deposition (PVD) techniques. In particular, the metallic film is realized employing Magnetron Sputtering (MS) (section 3.1), while the carbon foam is deposited with a Pulsed Laser Deposition (PLD) system (section 3.2). After the description of these two techniques, the main experimental methods and instruments used for characterization of thin films are presented in the last section: Scanning Electron Microscopy (SEM), Energy Dispersive X-ray Spectroscopy (EDXS) and substrate curvature for residual stresses.

3.1 Magnetron sputtering

Physical vapour deposition processes, in general, are based on the vaporization of a source of material, typically solid but sometimes liquid, in order to grow a thin film. Such material, in form of single atoms or small aggregates, is transported through the deposition chamber and finally impinges on a substrate where it condenses, producing a sample. The vaporization can occur through thermal evaporation or through sputtering.

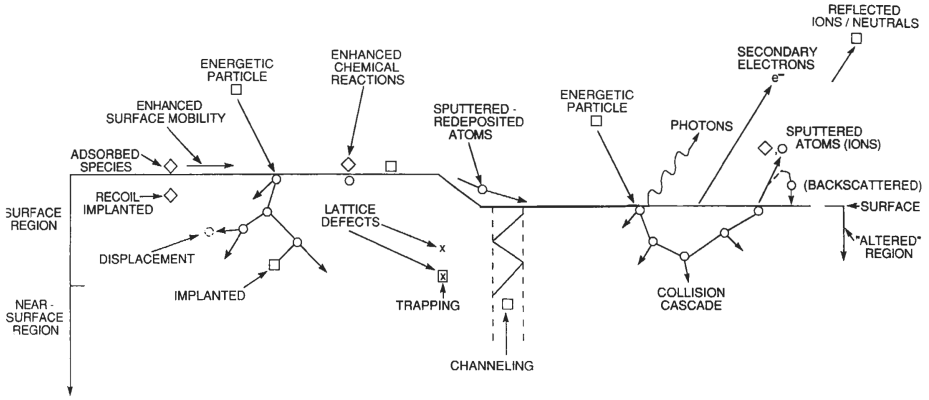

Figure 3.1. Depiction of energetic particle bombardment effects on surfaces and growing films, from [56].

Sputtering means that the emission of atoms from the source is due to the

bombardment with energetic particles of the target surface. In the interaction of such particles, mostly ions, with the solid material, a lot of phenomena take place (Figure 3.1), each depending on the type of ion, the nature of the surface atoms involved, and on the ion energy [56]. A minimum energy in the order of tens of eV is needed to extract an atom from the target, making it a threshold process. It should be noted that, in some cases, sputtered ions can also erode the target itself, producing self-sputtering.

To condense all possible events, the most fundamental parameter characterizing sputtering is introduced: *the sputter yield*. It is defined as the number of atoms (or molecules) ejected from the target surface per incident ion, and it is a measure of the efficiency of sputtering. Theoretical or semi-empirical expression for it can be derived [57, 58], and some values are reported in Table 3.1.

Table 3.1. Some values of sputter yields, from [56].

Sputtering Gas	He	Ne	Ar	Kr	Xe	Ar
Energy (keV)	0.5	0.5	0.5	0.5	0.5	1.0
Al	0.16	0.73	1.05	0.96	0.82	1.0
Au	0.07	1.08	2.40	3.06	3.01	3.6
C	0.07	–	0.12	0.13	0.17	-
Cu	0.24	1.80	2.35	2.35	2.05	2.85
Fe	0.15	0.88	1.10	1.07	1.00	1.3
Ti	0.07	0.43	0.51	0.48	0.43	-

What is left to understand is how to generate the energetic species needed to sputter the material. The simplest scheme consists of two electrodes in a low pressure gas chamber, with the target at the cathode and the substrate at the anode. Applying an electric potential difference between them, a discharge can be induced and gas ions are formed (plasma). Being charged, they are accelerated by the electric field on the cathode and thus can sputter it. Different gases and vacuum regimes can be adopted, affecting the deposition. A typically employed gas is argon, being inert, relatively inexpensive and with general good sputter yields. For reactive sputtering, nitrogen or oxygen can be added. Pressure has an important effect in the determining the deposition characteristics because scattering between the sputtered species and gas atoms increases at high values, leading to lower energetic deposited particles.

The *deposition rate*, that is the amount of material deposited per unit time, is given, in first approximation, by the product between the sputter yield and the impinging ion flux. So, in order to increase it, an higher current density at target surface should be achieved. In classical sputtering, this can be achieved increasing the pressure or the voltage. Nevertheless, in the first approach the energy of the species is reduced, and thus the film properties are degraded. At higher voltage, instead, much more electrons are produced and reach the anode, causing damages to the both substrate and growing film. The idea of Magnetron Sputtering (MS) is then introduced to reach higher deposition rates without theses drawbacks. Through the combined use of electric and magnetic fields, freed electrons produced during the sputtering process are trapped near the target surface, enhancing the ionizing efficiency and so leading to larger discharge current, which, in turn, means higher deposition rates.

3.1.1 Direct current magnetron sputtering (DCMS)

Magnetrons exploit a magnetic field parallel to the target surface and perpendicular to the electric field to constrain secondary electron motion to the proximity of the target. The magnetic field lines first emanate normal to the target, then bend with a component parallel to the target surface (the magnetron component). Electrons emitted from the cathode are initially accelerated toward the anode, executing a helical motion in the process, but when they encounter the region of the parallel magnetic field, they are bent in an orbit back to the target. This trapping produces a dense plasma region because of higher probability of gas atom ionization. It follows that ion bombardment of the target increases, giving higher sputtering rates and, therefore, higher deposition rates at the substrate. In addition, the increased ionisation efficiency achieved in the magnetron mode allows the discharge to be maintained at lower operating pressures (typically, 10^{-3} mbar, compared to 10^{-2} mbar) and lower operating voltages (typically, -500 V, compared to -2 kV) than is possible in the basic sputtering mode [59].

The magnetic field is produced by permanent magnets placed behind the cathode, i.e. the target. For circular electrodes, the two magnetic poles are in the form of an inner solid disk and an external ring, aligned in cylindrical symmetry. The relative strength of these two makes a distinction between balanced and unbalanced magnetrons, in which, respectively, magnets generate equal and unequal fields. While in the former case the dense plasma extends only for some centimetres, in the latter it can also reach the substrate, if the stronger magnet is the outer one (the so-called Type-2 configuration). This is due to the fact that not all the field lines are closed between the central and outer poles in the magnetron: some are directed towards the substrate, and some secondary electrons are able to follow these field lines. The plasma is no longer strongly confined to the target region, but is also allowed to flow out towards the substrate.

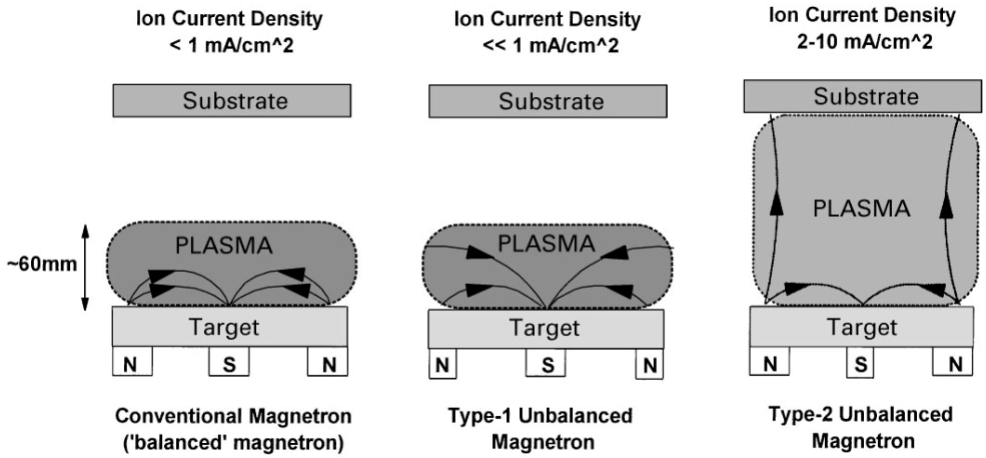

Figure 3.2. Schematic representation of the plasma confinement observed in conventional and unbalanced magnetrons, from [59].

The consequences of such unbalanced configuration are in the film growth. If the substrate is in the region of dense plasma, it will be subjected to strong ion bombardment which can affect film structure, producing denser ones. In balanced

magnetron it is possible to apply a negative bias to the substrate to increase the ion energy and current, but it can lead to defects in the film and increased stress. Substrate ion current densities approximately an order of magnitude higher than for a conventional magnetron can be generated with an unbalanced magnetron [60].

In the Type-1 case in which the central pole is stronger than the outer one, the field lines which do not close in on themselves are directed towards the chamber walls and the plasma density in the substrate region is lower, so such configuration is usually not adopted, except for depositions on delicate substrates like polymers.

Due to the positioning of magnets, the maximum ionization occurs between them and the shape of the formed plasma is toroidal. As a consequence, the erosion of the target assumes the form of a closed loop, called *racetrack* (see Figure 3.3). Such localized erosion makes the magnetic field stronger due to lowering of the distance to the magnets, leading to erosion rate increase and voltage decrease. This constitutes a limit on target utilization: only part of it, less than 50%, can be sputtered.

Figure 3.3. Photograph of a titanium target after use. The racetrack is perfectly visible.

After this general description of MS, a distinction in the operation of this technique can be made. The first and simpler possible way to power it is through Direct Current polarization. This gives the Direct Current Magnetron Sputtering (DCMS) deposition method. In this case, a continuous voltage (typically of hundreds of V) is applied between the cathode and the anode. As previously stated, a negative bias can also be employed on the substrate to accelerate the sputtered species and control their energy. In this operation mode, the typical average power density at the cathode is about several W/cm^2, resulting in a plasma density of the order of $10^{14} - 10^{16}$ m^{-3} [61]. The ionization fraction is typically really low, few percent or less [62], meaning that the majority of the species forming the film arrive at the substrate as neutrals. Moreover, because most of the charged particles bombarding it are Ar^+ ions, sub-plantation of argon in the film may occur, leading to lattice defects, high residual stresses, and poor adhesion. To improve film characteristics and achieve better control of the deposition, overcoming these drawbacks, another operation mode is feasible: High Power Impulse Magnetron Sputtering (HiPIMS).

3.1.2 High-power impulse magnetron sputtering (HiPIMS)

Magnetron sputtering can be operated in a pulsed mode, meaning that the applied voltage is modulated in time in form of pulses. The duration the pulses range typically from 1 µs to 1 s, with a frequency that spans from 10 Hz to 10 kHz. Each of them has a temporal width, also referred to as pulse on-time, between 5 µs and 5000 µs.

The idea is to use low duty cycles (i.e. the ratio between pulse on-time and cycle duration) to be able to increase the peak values during the on-time. A little average target power density is necessary to prevent overheating of the cathode and damage of the magnets and the target. Rectangular-shaped voltage pulse, which means constant value during the on-time, are the most used. On the other side, low duty cycles also implies low deposition rates.

The applied peak power density is typically in the range of a few kW/cm^2, while the average one is similar to DCMS, i.e. a few W/cm^2. In this way, target currents two or three orders of magnitude higher than the average target current in DCMS can be achieved (up to several A/cm^2). These high pulse currents result, in turn, in plasmas with electron densities in the order of 10^{18} m^{-3}. Total ion flux is also increased by orders of magnitude and a high degree of sputtered material ionization up to $\sim 70\%$ is reached [61].

In Figure 3.4, the current-voltage characteristics of DCMS and HiPIMS are shown. Considering a power law linking target current to voltage [63], it can be seen a change between the two operation modes, but also a transition during pulsed operation: at too high voltage, electron confinement is reduced.

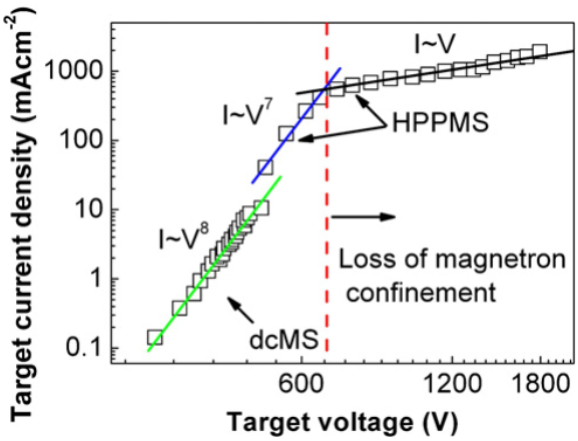

Figure 3.4. Current–voltage curves of a magnetron during operation in DCMS and HiPIMS, also spelled HPPMS, modes. The change of the slope from 7 to 1 at a voltage value of 650 V indicates loss of the electron confinement. From [61].

A common problem in sputtering processes is the occurrence of arcs. This phenomenon may be enhanced by the high peak target currents of HiPIMS operation, leading to detrimental effects on the quality of the deposited films, for example for the ejection of micro-metric droplets from the target. To mitigate it, the implementation of dedicated electronic systems is needed. Alternatively, short pulses of less than 20 µs can be employed: in this interval, the glow discharge remains in a transient regime, avoiding transition to arc.

The parameters of the deposition, like the peak target current and the gas pressure, influence the energy and the ionization degree of the sputtered species. In addition, thanks to high ionization fraction, the application of an electric field through a negative bias on the surface, is much more effective in controlling the ions energy and trajectories than in DCMS. In particular, a more directional flux can be obtained, allowing for homogeneous coating of complex surfaces.

Microstructure of deposited films varies according to some process parameters. A structure zone diagram (SZD) is often employed to illustrate this. Surface and bulk diffusion are the main influences on the growth process and can be related to the homologous temperature T_h, i.e. the ratio between the film growth temperature and its melting temperature. A second parameter to account for is the process pressure: at high values, scattering events become more frequent and, so, the energy of the species that reach the substrate is reduced and homogenized [64]. A basic structure zone diagram, then, has two axes, one to account for thermal effects (T_h), and the other for kinetic ones (P) [65]. Nevertheless, when the particles are particularly energetic as in HiPIMS, different parameters have been proposed by Anders [66].

The two-axis diagram can be divided into four zones, each corresponding to a different morphology.

- **Zone I**: the mobility is low, and it leads to continuative nucleation of grains, which results in a finely grained structure directed in the growing direction, with a high degree of lattice defects and pores at grain boundaries.
- **Zone T**: surface diffusion is possible, but grain boundary one is limited, leading to a competitive growth of V-shaped grains, inhomogeneous through the film thickness.
- **Zone II**: both surface and grain boundary diffusions are enhanced, resulting in uniform columnar grains.
- **Zone III**: finally, close to melting temperature, bulk diffusion and recrystallization dominates, and large grains can grow.

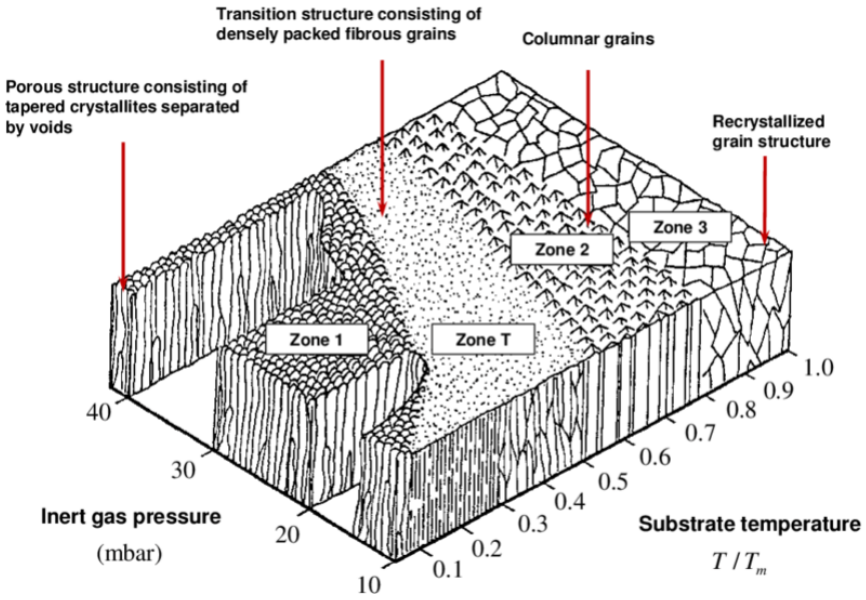

Figure 3.5. Structure zone diagram by Thornton for sputter deposition of metallic films, from [65].

DCMS deposited films typically show a columnar morphology, with a density not too high, while HiPIMS enables the production of denser films with a more compact microstructure and reduced surface roughness.

Magnetron sputtering system at NanoLab

The deposition system that has been used throughout this thesis work is located at the Micro and Nanostructured Material Laboratory (NanoLab) of Politecnico di Milano. The main part is a stainless steel cylindrical vacuum chamber of 500 mm in diameter and 670 mm in height. In the upper part of it, the sample holder takes place, while in the bottom part two magnetron cathodes in confocal geometry are present. The anode is linked to a motor so that it can rotate, setting the speed, to allow greater uniformity in the deposition, and can also be heated. A negative bias can be applied to it, in order to control the energy of the charged species. On the cathodes, planar, circular targets can be mounted. They are cooled through a water circuit and can be covered by a pneumatic shutter. The power supply consists in two Direct Current generators of 6000 W and 1500 W connected to a pulsing module. The system can then be operated both in DCMS and HiPIMS modes, with or without bias.

The vacuum in the chamber is obtained through the operation of two consecutive pumps: a scroll pump allows to reach a pressure of about 10^{-2} mbar, while a turbomolecular pump can bring the chamber to 10^{-7} mbar. A gas cylinder of argon is connected to the chamber through a feedback valve, allowing for the setting and control of the sputtering pressure. The measure of the pressure is obtained with several gauges (Pirani, capacitive).

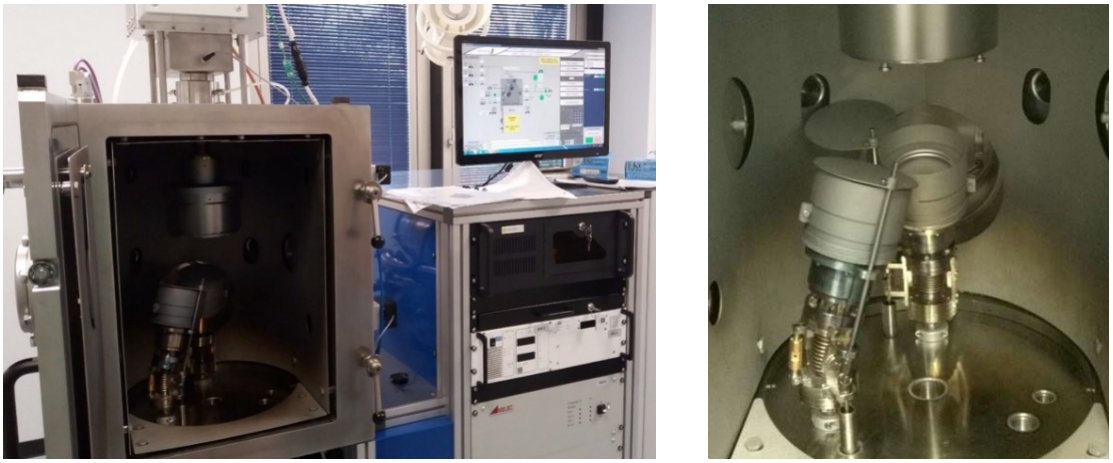

(a) (b)

Figure 3.6. (a) The deposition system installed at NanoLab and (b) a close up of the chamber, in which the cathodes and the anode are visible.

3.2 Pulsed laser deposition (PLD)

In pulsed laser deposition, the physical mean employed to vaporize the target is a laser pulse. The description of the processes that take place during the deposition is not

trivial. In a vacuum chamber with controlled gas atmosphere, the laser pulses interact with the target, and ionization, plasma formation and heating of the surrounding zone occur. The plasma plume is composed of ablated atoms, molecules, ions, clusters and bigger particulates, depending on the deposition parameters. Then, such species expand toward the front of the target, where the substrate of the deposition is located, and further interaction between the plume and the laser can potentially happen. Collisions among the species, or with the gas atoms, could also take place, leading to the formation of bigger aggregates. Once the ablated species reach the solid substrate, a thin film can form, also through rearrangement of the particles on the surface, in particular at relatively high temperatures. A schematic view of the technique is presented in Figure 3.7.

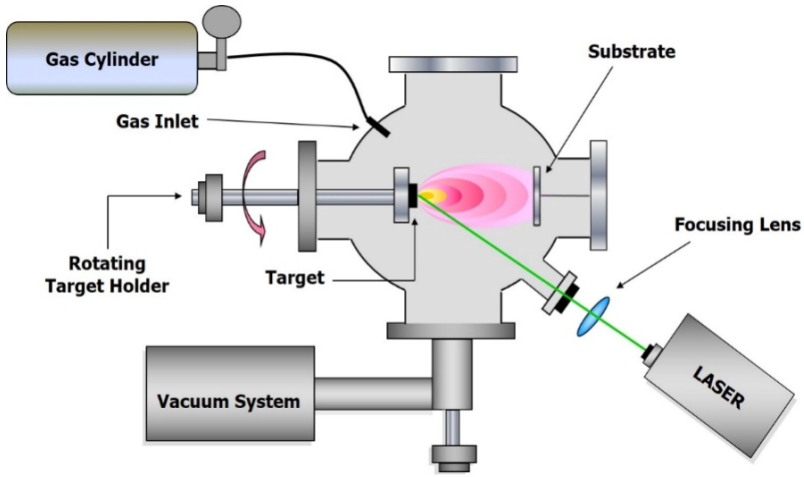

Figure 3.7. Schematic representation of PLD experimental set-up, from [67].

The employed parameters in PLD are: laser pulse of nanosecond or femtosecond duration, repetition rates around 10 Hz or more, fluences from less than one to a hundred of J/cm^2 and background pressure in the range $10^{-7} - 10$ mbar. Because the ablation of material can be high, to avoid the boring of the target, it is moved around, so that the interaction with the laser occurs evenly over the surface.

Because of the complexity of the physical phenomena taking place, the tuning of the deposition parameters can lead to very different resulting samples, from compact films to extremely low density foams. As an example, the background pressure influences the propagation and the kinetic energy of the ablated species in a way that at low values (or in vacuum), high energy and directionality lead to compact film, while at higher pressure, due to lower energy and directionality, porous ones are obtained. Even the target-substrate distance has a kinetic effect, increasing the travelled path and so the collisions. On the other hand, a uniform deposition over areas larger than few cm^2 is difficult to achieve. Substrate rotation can help in partially compensate this limit, that is due to the strong directionality of the plasma plume. Reproducibility of results can also be a problem, along with the difficulty in depositing on non-planar surfaces. For this reasons, this technique is more used in research than in industrial applications. Other advantages are the possibility of reactive and stoichiometric multi-elemental depositions. A particularly important role is played by the pulse duration, discussed in the following.

In nanosecond regime, laser intensity is typically low, so that the absorption of the pulse energy in the target is linear. Because of lower inertia, electrons are the first to interact with the laser, while only in some ps lattice vibrational modes, and so ions, will be excited. As the time duration of the pulse is longer than these time scales, both phenomena happens during each interaction, leading to material heating and melting. For a sufficiently high total energy, thus, vaporization can take place. Nevertheless, at high fluence, explosive boiling of the target with consequent emission of molten droplets can happen, which is detrimental for film deposition. A distinctive feature of ns-PLD is that the pulse lasts long enough for laser-plume interaction to occur, so that additional energy is transferred to the ablated species, causing further ionization and excitation. Lastly, it can be noted that some species can be scattered back toward the target surface, giving sputtering or redeposition.

3.2.1 Femtosecond pulsed laser deposition

The shorter pulses, of femtosecond duration, bring in different ablation mechanisms. In this case, because the characteristic times of ions dynamics are longer than the duration of the single interaction, direct coupling of the laser with the lattice is not possible. Energy is thus transferred directly only to electrons, the laser-plume interaction that is peculiar to nanosecond PLD here can not happen, and thermal effects are less important. A better energy transfer to the target thus occurs, leading to a greater ablation efficiency [68]. Moreover, the greater intensity of fs pulses allows for non-linear energy transfer.

A feature that distinguish the fs-PLD is the direct ablation of nanoparticles and clusters, while in the nanosecond regime their production requires the interaction with the background atmosphere that makes atoms stick together. In fact, the species emitted with longer pulses are mostly atoms and ions, as ionization is enhanced by laser-plume interaction. The shorter ones, instead, ablate more nanoparticles and clusters of varying dimension, typically of some nanometres [69]. Indeed, the possible emission of big flakes (microns) at high fluence could be detrimental to the film deposition.

The interest in this deposition technique, as far as this work is concerned, is in the possibility of growing very low density films, down to few mg/cm^3 as carbon nanofoams [70]. At low fluence (less than 1 J/cm^2) and relatively high pressure (around 100 Pa and beyond), cauliflower-like structures with a high porosity morphology are obtained. The employed gas has also an effect on the film, with heavier ones like argon giving more uniform and web-like foam structures. An aggregation model for the foam growth has also been developed: nanoparticles aggregate while in flight reaching the substrate as micrometer fractal aggregates, in a snowfall-like process [55].

Femtosecond pulsed laser deposition system at NanoLab

At NanoLab, Politecnico di Milano, both ns and fs PLD systems are present. For this work, the femtosecond one has been used. It is composed by two main independent parts, the laser and the vacuum chamber. The former is a commercial tabletop system by Coherent in which the CPA technique is adopted. A Ti:Sapphire oscillator creates the initial pulse, while the pump is a second harmonic Nd:YAG laser. The output is

a 80 fs pulse with a maximum energy of 5 mJ. The repetition rate is of 1 kHz, thus an average power of 5 W is obtained. The beam passes through a series of optical elements before entering the deposition chamber. In particular, a polariser coupled with a Brewster angle mirror allows for energy control, cutting part of the radiation when it is not orientated along the s polarization. The final lens has a focal length of 1.5 m and it is mounted on a rail so that it can be moved to change the spot size on the target.

In the vacuum chamber, the laser hits the target at 45° after crossing a window with high transmittance and anti-reflective coating. Both the target, which is made of pyrolytic graphite, and the substrate are mounted on motorized holders, so that translation in three directions and also rotations can be controlled through the terminal, also allowing to set their relative distance. The substrate temperature can also be controlled via software, as well as vacuum level and gas pressure. Two pumps, a scroll and a turbomolecular one, are operated in series to reach vacuum and then argon gas can be introduced. The pressure is kept constant thanks to a feedback loop and is monitored through two main sensors, a wide-range gauge (Pirani gauge plus Penning gauge) and a capacitive one.

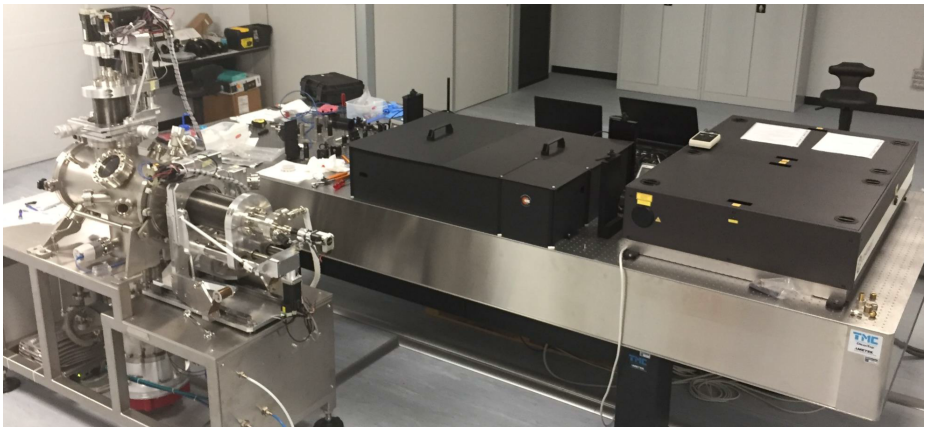

Figure 3.8. The fs-PLD system installed at NanoLab. The deposition chamber is visible on the left, while on the right the optic table with the laser is present. From [71].

3.3 Characterization techniques

The films that will be deposited exploiting the two above described techniques to produce targets for laser-driven particle acceleration, need to be characterized in some of their properties. Here, the instruments and methods employed for this scope are presented.

In this thesis work, Scanning Electron Microscopy (SEM) is used to study the morphology, but also the integrity of the films. It is also useful to measure the average thickness of the samples, through cross section micrographs. In particular, at NanoLab a field emission scanning electron microscope working in high vacuum Zeiss Supra 40 is installed. It is equipped with a high efficiency In-lens detector, a Everhart-Thornley Secondary Electron Detector and a Back-Scattered Electron Detector. The main characteristics of such microscope are: acceleration voltages between 200 V and 30 kV;

working distance ranging from 2 to 30 mm; maximum resolution of 1 nm at 20 kV with In-lens detector.

The SEM is also equipped with a microanalysis apparatus for Energy Dispersive X-ray Spectroscopy (EDXS) elemental analysis made by Oxford Instruments. In this thesis, it is employed to compute the mass thickness, and possibly density if a separate measure of thickness is known. In fact, a reference-free evaluation technique based on X-rays emissions has been developed by the group [72], which is particularly useful for the low density foam films. It has to be said that the X-ray detector was substituted with a better one, in terms of efficiency and resolution, during this work. As a consequence, the technique has been available only for a reduced time. Moreover, as will also be explained in the next chapters, the efficiency curve of the new instrument was not known and an experimental estimate of needed values has been tried.

The titanium samples deposited by magnetron sputtering were also characterized in terms of residual stress, as it influences the capability of remaining intact after the removal of the sacrificial substrate in the preparation of free-standing films. Substrate curvature method has been employed [73], analyzing the variation in distance between four laser spots reflected by the sample, before and after the deposition. In addition, a common analytical balance has been used to determine the deposited titanium mass, which in combination with a surface measure (through a simple ruler, for rectangular specimens) gives an alternative esteem of the density.

In the following, a more detail description of these techniques is given.

3.3.1 Scanning electron microscopy (SEM)

Electronic microscopes have been introduced to overcome the limitations of optical microscopes (OM), in particular in terms of maximum magnification and resolution. The Scanning Electron Microscope (SEM) has been developed in 1942, although it is only in the sixties and seventies that it became widely used. Using electrons as probe instead of light, it is possible to reach higher magnifications and greater resolutions, also gaining compositional information. In the SEM, the sample is scanned moving the electron beam and a point-by-point image is formed analysing the signal arising from the local interaction. To avoid unwanted collisions and contaminations, the sample is observed in vacuum.

The magnification is limited by the diffraction limit. Thus, reducing the wavelength of the probe, as it is possible employing massive particles like electrons, allows for greater results. In addition, charged particles can be strongly collimated through electric and magnetic fields, improving the resolution. In Table 3.2, a comparison between OM and SEM typical values is shown.

Table 3.2. Comparison between the typical characteristics of optical microscope and scanning electron microscope.

	Magnification	Field depth (10x and 100x)	Resolution (ordinary and limit)
OM	$1 - 10^3$	0.1 mm − 1 mm	5 µm− $\sim$ 0.1 µm
SEM	$10 - 10^5$	10 mm − 1 mm	50 nm − $<$ 1 nm

As it is depicted in Figure 3.9, the experimental scheme of the SEM can be summarized as:

- the electronic gun that produces a monochromatic electron beam;
- a first condenser lens that limits the current and blocks the electrons at high angle through an aperture;
- a second condenser lens that forms a thinner and more coherent beam;
- a system of scanning coils that deflects the beam, making it impinging on the surface of the sample sequentially;
- the final lens that focuses the beam on the sample;
- the detectors that reveal the particles coming from the interaction between the electrons of the beam and the sample.

A brief description of these elements is given in the following.

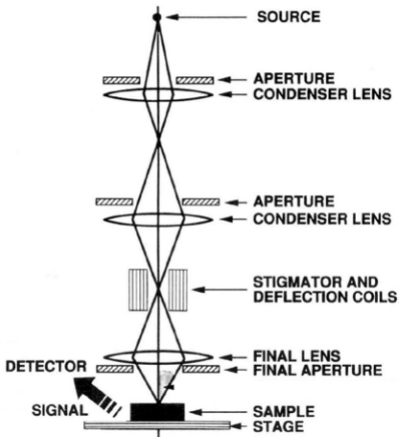

Figure 3.9. Schematic representation of a scanning electron microscope.

Electron guns can be based on two different effects, i.e. the thermionic effect and the field emission. Sources that exploits the thermionic effect consist in a tungsten filament heated up to 2700 K or in a crystal of lanthanum hexaboride heated to about 2000 K. At these temperatures, the electrons gain sufficient energy to overcome the work function of the material and thus are emitted by the tip of the filament. To avoid the oxidation of the filament, operation in high vacuum is needed ($10^{-5} - 10^{-6}$ mbar). The produced electrons are then accelerated by a potential difference of $1 - 50$ kV. Field emission guns, instead, emit electrons due to the effect of a strong electric field applied to the source. It consists in a very thin tip, usually made by tungsten, kept in ultra high vacuum ($< 10^{-8}$ mbar). In this case, more collimated and focused beams can be obtained. In addition, the needed acceleration and focusing systems require lower potentials. A combination between the two types, which allows for a higher brilliance, is obtained by coating the tip with a low work function material as zirconium oxide. In particular, this kind of source, called Schottky gun, is the one equipped on the SEM at NanoLab.

The lenses employed in the SEM are mainly of two types, i.e. electrostatic lenses, that accelerate the beam through a potential difference, and electromagnetic lenses (condenser and objective). This second kind of lenses are meant to focus and direct

the beam. In particular, the condenser lenses are located in the first part of the optical path and they set the current that arrives at the sample. The camera lens, or objective, instead, is near the sample and it sets the final dimension of the beam and thus the resolution. Between the lenses, a diaphragm controls the final aperture and limits the dispersion of the beam. A typical electromagnetic lens is constituted by a cylindrical coil with a ferromagnetic core. Electrons are deflected by the Lorentz force and, as the magnetic field generated is proportional to the current that flows in the coil, the focal distance can be controlled adjusting its value.

To get the scan of the electrons on the surface of the sample, two couples of coils are used, each producing a magnetic field that deflects the beam along the two axes. The beam moves along parallel and equispaced lines, in order to cover the whole surface. It interacts with the sample and produces a signal, which is detected by the detector, modulated by the amplifier and then transformed in a greyscale image on the monitor.

The signal produced by the interaction between the beam and the sample can be of different types: electrons (scattered, transmitted or Auger), X-rays and phonons. Both elastic and inelastic scattering happen. The majority of the signal is due to inelastic interactions with valence electrons of the sample, that results mainly in secondary electrons (SE) with energies lower than 50 eV. For a single incident electron, many can be emitted in an avalanche effect. Thus, the yield (i.e. number of secondary electrons emitted per impinging electron) can be greater than one and it has a weak dependence on the atomic number Z. On the other hand, it lowers increasing the incident energy and increasing the incidence angle. Secondary electrons do not give information about the composition but are very sensitive to surface topology. Due to the low energy, their escape depth is short: only the superficial electrons can come out of the sample. The escape probability decreases approximately exponentially with travelled distance. Thus, the number of emitted secondary electrons strongly depends on the orientation of the surface with respect to the incident beam and so on the morphology: tilted surfaces appears as more white. Elastic collisions between the electrons of the beam and the the nuclei of the sample atoms, instead, lead to backscattered electrons (BSE) that are more energetic. The scattering occurs in all directions, although back reflection is particularly effective. Their yield is sensitive to the atomic number of the sample due to the different charge density. In particular, at low Z the yield is low (black spot), while at high Z it is bigger (white spot). Thus, BSE gives qualitative information about the composition. X-rays production and the information that they can give will be described in section 3.3.2.

The volume responsible for the different signals is called escape volume (Figure 3.10). Auger electrons has the smallest volume (few nm), while secondary electrons are emitted from $10 - 20$ nm depths at maximum. Backscattered electrons, as they are more energetic, have escape depth of $1 - 2$ µm and the less interacting X-rays can come from $2 - 5$ µm. These values are general references, as the interaction volume depends on the energy of the beam and on the average atomic number of the sample.

Lastly, the detectors can be considered (see Figure 3.11). Different ones are needed for different signals. The most used detectors are Everhardt-Thornley and solid state detectors. The Everhardt-Thornley detector consists in a scintillator, a light guide and a photomultiplier. It allows to detect both BSE and SE and to distinguish the two signals, the different characteristic energies are exploited. SE are not energetic

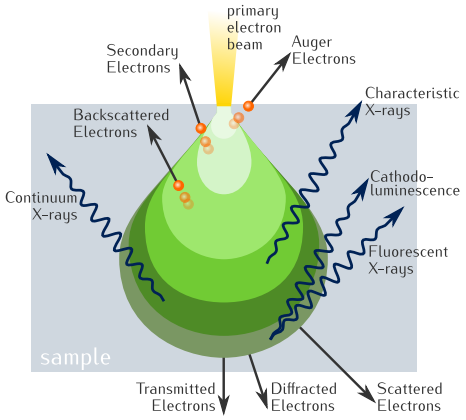

Figure 3.10. Volume from which the different signals arise in the interaction between the electron beam and the sample, from [74].

enough to give scintillation, so they are accelerated by an electric field. A grid that can be polarized positively or negatively allows the selection between SE and BSE: with positive potential, the secondary electrons are attracted and accelerated; with the negative one, backscattered electrons can still reach the detector, while SE are blocked. It is typically positioned on the side, so that it does not interfere with the incident beam. A solid state detector detector, specific for BSE, is used. It is made of silicon doped diodes in the form of a circular ring, located at the maximum of backscattered electrons, i.e. above the sample. As SE are not energetic enough to give electron-holes pairs, only BSE are detected. Moreover, a detector for both secondary and backscattered electrons placed within the electro-optical column, called in-lens detector, is used to form very high resolution images.

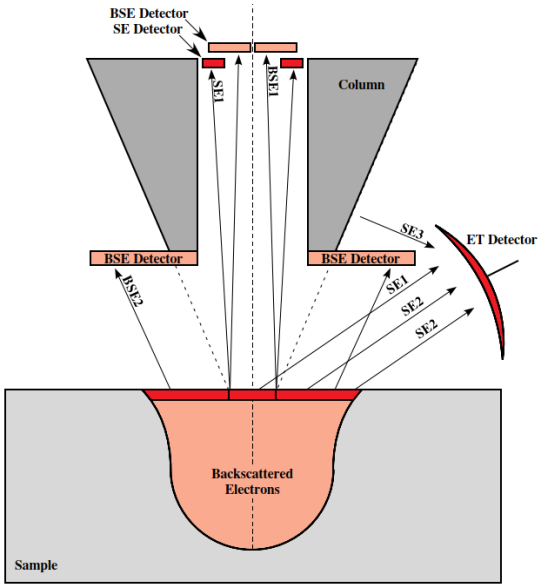

Figure 3.11. The typical location of the detectors in a SEM, from [75].

3.3.2 Energy dispersive X-ray spectroscopy (EDXS)

In the SEM apparatus, characteristic X-rays are emitted as a consequence of the interaction between the electron beam and the sample. These can be used to probe quantitatively the composition of the sample. Measuring and analysing the energetic distribution and the intensity of the photons, it is possible to compute the elemental concentration of the elements present in the sample, point by point. This technique is known as Energy Dispersive X-ray Spectroscopy (EDXS).

The resolution associated to the analysis is determined by the escape depth of the photons, that is usually in the order of some micron. On the other hand, the resolution is limited both by the excitation volume and the signal intensity: lower incidence energies gives lower interaction volumes but also weaker signals. Semiconductor detectors are typically used. As an example, lithium doped silicon is often equipped on SEM, even though liquid nitrogen cooling is needed to reduce the thermal noise. Another kind of detector that is used is the silicon drift detector. The newly installed detector at NanoLab is of this kind. Silicon drift detectors allows for high count rates, high energy resolution and do not need liquid nitrogen cooling, as Peltier effect is exploited to keep the temperature low. Despite the detection technology, the absorbed photon generates a certain number of electron-hole pairs and a current arises. Measuring it, the energy of the particle can be retrieved, and thus the element the has produced it can be identified.

Through EDXS it is also possible to measure the mass thickness of the sample. The idea was proposed for the first time in 1960 by Sweeney, Seebold and Birks [76]. It is appealing as it is a non-destructive technique that exploits a common instrument (a SEM with a X-ray spectrometer), for which the surface roughness does not affect the measurement and that has a high spatial resolution, down to tens of nanometres. From the calculation of the ratio (generally known as k-ratio) of the X-ray intensities of each element in the sample and the ones emitted from a homogeneous reference sample of known composition, the mass thickness can be retrieved. Indeed, it is possible to relate the k-ratio to the mass thickness through the knowledge of the distribution in depth of the generation of characteristic X-rays. The knowledge of this distribution is of crucial importance in the computation of mass thickness. Nevertheless, its shape is not so easy to determine, as it depends on the ionizations caused by energetic electrons which undergo complex multiple scattering events. Software employing semi-empirical and empirical models based on measures present in databases for the computation of such function have been developed. However, this strategy suffers from the limitation of the needed knowledge of measurements of a standard reference sample having the same composition of the substrate or the film, along with the intrinsic uncertainties of the experimental data.

Another reference-free technique has thus been developed [72]. Electron transport in solids can be studied in a kinetic approach, solving the Boltzmann transport equation under some simplifying assumption. It is thus possible to compute the functions for the distribution in depth of the generation of X-rays in a more reliable way, also in multilayer cases. Such functions enable to relate thin film mass thickness and composition to EDXS data using an innovative method: instead of the k-ratios, the ratio of the film X-rays intensities over the substrate intensity. In this way, there is no more need of reference samples, once the substrate composition is known, allowing

for reference-free measurements.

3.3.3 Substrate curvature for residual stresses

Various experimental methods to measure residual stresses in thin films are described in literature [73]. Among them, substrate curvature is one of the most versatile. In addition, it is non-destructive and can be used in real-time. The principle behind the method is to measure the curvature induced in the substrate due to stress in the film. Thus, two measurements of the radius of curvature have to be performed, i.e before and after the deposition, as the difference between the two is related to the film only.

The fundamental equation that relates the curvature radius to the stress of the film σ_f is the Stoney equation, which was derived for the first time by Stoney in 1909 [77]. It reads:

$$\sigma_f = \frac{E_s}{1-\nu_s}\frac{t_s^2}{6t_f}(\frac{1}{R}-\frac{1}{R_0}), \tag{3.1}$$

where E_s and ν_s are the Young modulus and the Poisson ratio of the substrate and t_s and t_f are the thicknesses of the substrate and the film, respectively. Here, R is the curvature radius after the deposition, while R_0 the one before it. Note that the average stress cannot be determined from the curvature without knowing the film thickness, which can be retrieved, for example, from SEM images of the cross section.

Some basic assumptions that also determine the validity of Equation 3.1 are made in its derivation. In the first place, it is assumed that the substrate is thin and that the film is much thinner of it, i.e. $t_f << t_s << R$. Moreover, the average stress in the Stoney equation is assumed to be equi-biaxial and laterally uniform. It means that it is not considered the case of polycrystalline films in which the stress may be different at/near the grain boundaries with respect from that in the middle of the grain. Or, also, that the stress may be non-uniform over the surface. Not only, the stress may vary through the thickness of the film. As the computed residual stress is averaged along the thickness, a single curvature measurement does not provide any information about the depth-dependence of the stress in the film. To assess the depth-dependence of the stress, successive measures of its evolution during the deposition are needed. It can also be noted that the knowledge of the film material mechanical properties are not needed. The Stoney equation depends only on the substrate properties, as under the thin film assumption, it dominates the flexural behaviour of the composite system.

Multiple techniques have been developed for measuring the wafer curvature. The apparatus installed at NanoLab that was used in this work is based on laser reflection [78]. The beam is generated by a diode laser ($\sim$ 5 mW output, 630 nm wavelength). Then, it passes through a pair of etalons. The first etalon multiplies the input laser beam in a direction, while the second one, oriented at 45° with respect to the first, duplicates it in the other direction. In this way, a 3 $\times$ 3 beam array is obtained. Nevertheless, the central spot is obscured through some tape as it is too much intense, while the four most external lights are too weak. Thus, a 2 $\times$ 2 array is the one employed in the measurements. After being focused, light impinges on the sample's surface at an angle of 60° and the reflected spots positions are recorded through a lens and a CMOS camera (4/3, 1.3 MegaPixel sensor, 1024 $\times$ 2048 digitalized image). The signal from the detector is elaborated by a pc software that allows to record it in

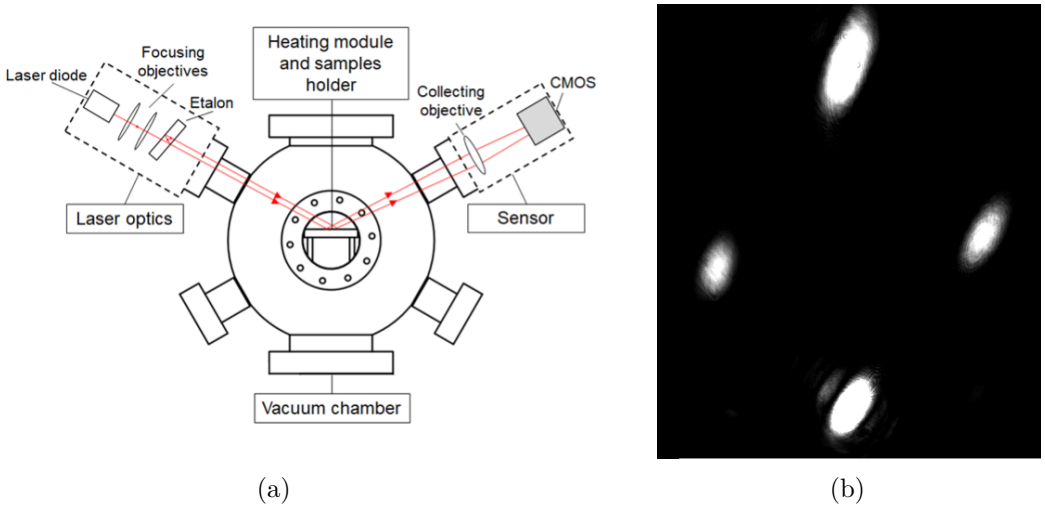

(a) (b)

Figure 3.12. (a) Scheme of the experimental setup, adapted from [78], and (b) laser spots array recorded by the camera.

the form of a sequence of frames (see Figure 3.12). The centroid of each spot is then computed with a MATLAB script and the curvature radius of the film is estimated. Lastly, the stress state of the film is evaluated according to the Stoney formula. It has to be noted that the accuracy of the method can be affected by vibrations. In this regard, the use of multiple laser beams reduces the sensitivity to such error source. Indeed, vibration of the sample may change the direction of the reflected beams, but it changes them all by the same amount. The relative spacing between the beams is thus not change and the curvature is determined from the change of it [73].

Chapter 4

Thin film production and characterization

4.1 Introduction

As the goal of this thesis work is to produce single and double layer free-standing targets, it is important to initially know how to produce the two desired films and what are their characteristics. So, in this chapter the deposition of titanium and carbon foam samples, respectively trough MS and fs-PLD, is addressed. In particular, in order to analyse their characteristic through the techniques described in section 3.3, the films are deposited on 500 μm thick (100)-silicon substrates. The starting point in the choice of the deposition parameters in both cases is given by the previous knowledge and expertise developed by the group, in particular in the framework of the ERC funded project ENSURE (Exploring the New Science and engineering unveiled by Ultraintense ultrashort Radiation interaction with mattEr) [71]. In this regard, these previous theses [54, 79] and papers [80, 81] are particularly relevant.

Titanium films were deposited employing both DCMS and HiPIMS in a hybrid combination, as described in section 4.2.1. The choice of this specific metal arises from the previous knowledge on his behaviour under sputtering, guided also by its interesting properties such as high mechanical strength, excellent thermal stability and good corrosion resistance in extreme conditions. As the goal is to be able to produce free-standing films in a relevant range of thicknesses, a preliminary study on film properties and uniformity is carried out. Thus, the parameters of the deposition were fixed, and a thickness scan between 100 nm and 2 μm of residual stresses and densities were performed. Morphology is also observed through SEM images, and the results are presented.

In the case of carbon foams obtained through fs-PLD, the samples have been characterized qualitatively in terms of morphology and quantitatively for mass thickness and density. The depositions were carried out not only on plain silicon, but also on two previously produced titanium films, to check for substrate effects. The results are presented in section 4.3.

4.2 Titanium films

4.2.1 Choice of deposition parameters

Employing a 99.995 % pure titanium metallic target with dimensions 76.2 mm in diameter and 5 mm in thickness (Testbourne Ltd, England), the films were deposited on silicon. The substrates were cleaned with isopropyl alcohol prior to the deposition, which occurred at room temperature (no anode heating). Moreover, the samples were rotating at 5 *rpm* to assure uniformity. Commercial argon (99 % pure) was employed as sputtering gas and the pressure was fixed to a value of 5×10^{-3} mbar, obtained on a vacuum of about 10^{-7} mbar.

A multi-layer hybrid structure was adopted. Each layer, hereinafter called hybrid layer, is obtained as a sequence of DCMS and HiPIMS, whose duration is decided based on the fraction of thickness to be deposited in one way or the other. Indeed, parametric experimental campaigns were conducted in the context of a doctoral work by D. Vavassori prior to this thesis. In this investigation, the effect of the number of hybrid layers (1,2,4,8), the applied bias in HiPIMS (0 V, 250 V, 500 V) and the thickness fraction deposited in the pulsed regime (20 %, 50 %, 80 %) have been studied. His experimental results are used as a starting point for the choice of the deposition parameters and thus are here presented. In Figure 4.1 and Figure 4.2, the resulting

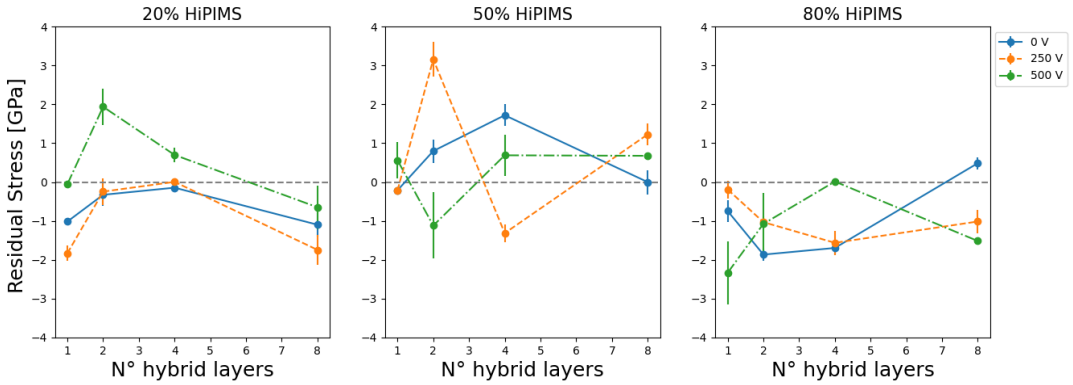

Figure 4.1. Residual stresses of titanium films as a function of the number of hybrid layers and for different HiPIMS fraction and biases.

values of density normalized over the bulk value of titanium and residual stress are reported. For all these samples, the thickness was about $400 - 500$ nm. It can be seen that the number of layer influences mostly the stress state of the film, which should be as close to zero as possible, while the fraction of HiPIMS has an effect on the compactness and density. Based on these data, a choice for the three parameters that appears as a good compromise in terms of both density and stress, also taking into account the duration of the depositions, was made for the films concerning this specific thesis work. In particular, 4 hybrid layers with 20 % of HiPIMS thickness were employed, although some depositions with 8 layers and/or 40 % were tested. Two additional depositions setting pure DCMS and pure HiPIMS with the same discussed parameters were also performed as a comparison.

The DCMS part was obtained maintaining constant the imposed parameters for

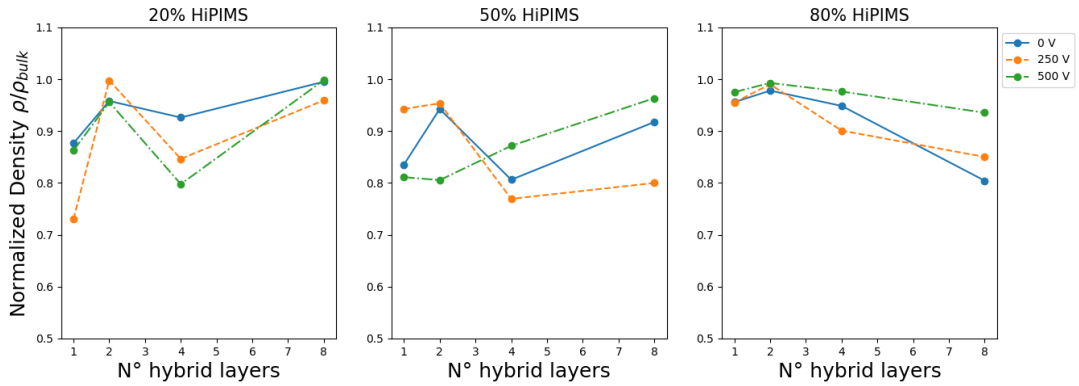

Figure 4.2. Normalized density of films as a function of the number of hybrid layers and for different HiPIMS fraction and biases.

every deposition, namely 500 V, 2 A, 300 W as nominal values. Indeed, the effective values, given that the three quantities are linked to each other, were less, as can be seen in Table 4.1. No bias was applied and the temporal duration of the deposition was chosen according to the desired film thickness. In this regard, an estimate of the average deposition rate has been obtained dividing the thickness measured on an apposite specimen by the deposition duration and resulted in about 10.19 nm/min for DCMS.

Table 4.1. DCMS deposition parameters.

	Nominal	Read
Voltage [V]	500	350
Current [A]	2	0.7
Power [W]	300	250

Table 4.2. HiPIMS deposition parameters.

	Nominal	Read
Peak Power [kW]	-	36-37
Current [A]	10	0.3
Power [W]	300	250

Total duration [µs]	5714
Sub-pulse on-time [µs]	20
Time between sub-pulses [µs]	200
Duty cycle [%]	1.75009

In HiPIMS, on the other hand, a structured pulse, composed by 5 sub-pulses, giving the so-called *chopped-HiPIMS* [82], was adopted. Such choice allows for an increase in the deposition rate, which in any case is quite low, around 2.75 nm/min. All the parameters are reported in Table 4.2. In this case, the parameter that is kept constant during the deposition is not the voltage but the *peak power*. It can be computed from the applied voltage V and the peak current density J_{peak} as $P_{peak} = V \cdot J_{peak} \cdot A$, where A is the racetrack area. Through an oscilloscope, the peak current density at the target can be measured, while the racetrack area is estimated to be around 23 cm^2. Since J_{peak} can vary during the depositions due to the digging of the metallic target, the applied voltage has been changed (always around $600 - 700$ V) in order

to keep constant P_{peak}. Indeed, this parameter has an effect on morphology. In particular, it can be globular or lamellar, and the second one is to be avoided to have flatter surfaces [80]. Thus, the peak power is set to the appropriate value of about $36 - 37$ kW. Lastly, in HiPIMS, a bias of 250 V has been imposed to the anode, to allow for a more compact result.

4.2.2 Morphological and structural characterization

To see the qualitative differences between DCMS and HiPIMS, the SEM micrographs presented in Figure 4.3 can be considered as they present pure, non-hybrid samples. In the former case, the cross section shows a relatively open structure, characterized by columnar grains with pyramidal tips and some voids, while a more compact and flat structure is obtain with the latter. In multi-layer hybrid films, an intermediate situation arises. In fact, the pulsed operation, which allows for more energetic species, initially fills the voids of the DC and then makes the thickness increase. This is also one of the reasons why the deposition rate is much lower, along with the back-attraction of metal ions to the target and the low duty cycle.

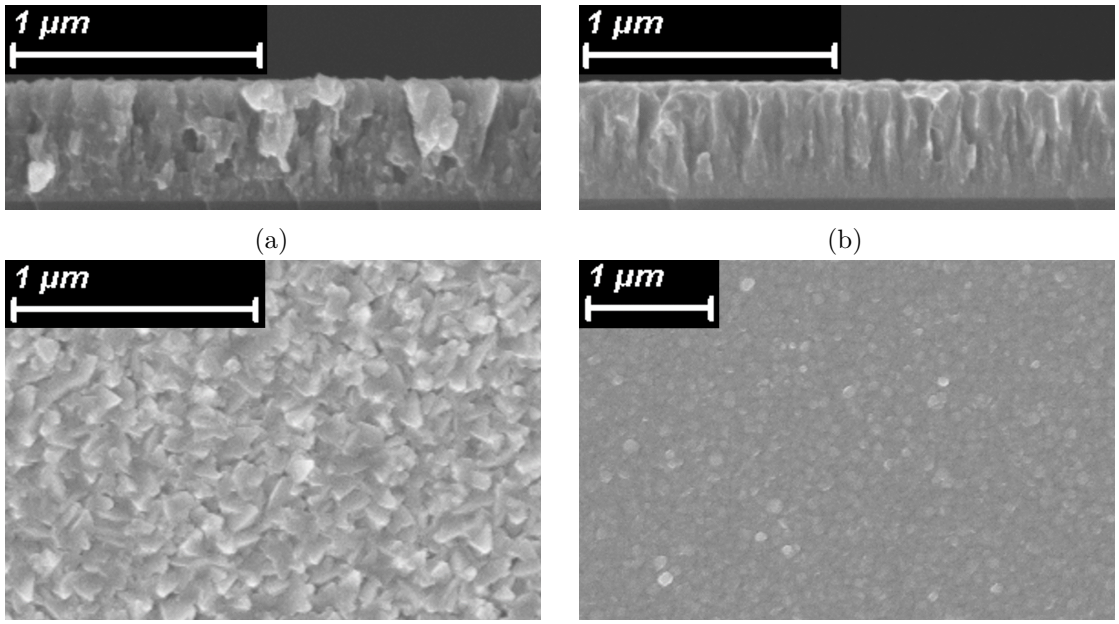

Figure 4.3. SEM images of the cross sections and planar views of (a,c) a pure DCMS film and (b,d) pure HiPIMS with 250 V bias. Both have a thickness of approximately 500 nm.

In Figure 4.4, the cross sections and planar images of hybrid films are shown. The layered structure is somewhat visible, in particular at high thicknesses, as well as the slightly more compact columnar structure. The surface appears as quite smooth, with less elongated, more circular grains. The thickness of the samples has some influence, in particular below 100 nm or above one micron. In the first case, the film growth is not completely developed, while in the second the structure appears as more oriented, with smaller columns.

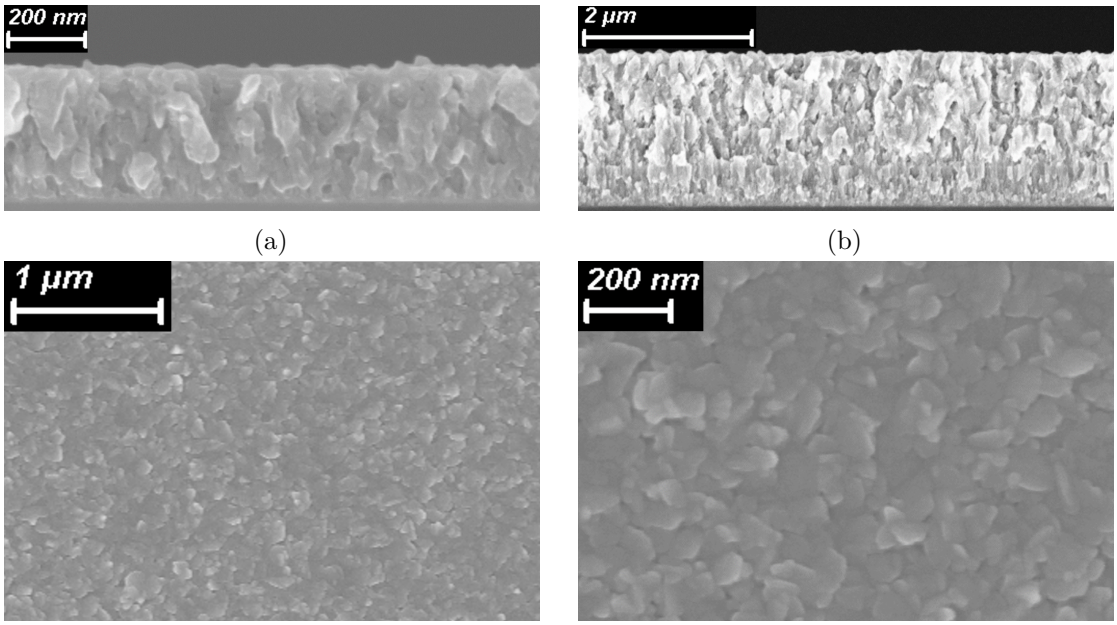

Figure 4.4. SEM micrographs of 4 layers, 20 % HiPIMS hybrid films. Cross section of (a) a thinner (400 nm) and (b) a thicker (2 µm) films and (c,d) planar views with different magnifications.

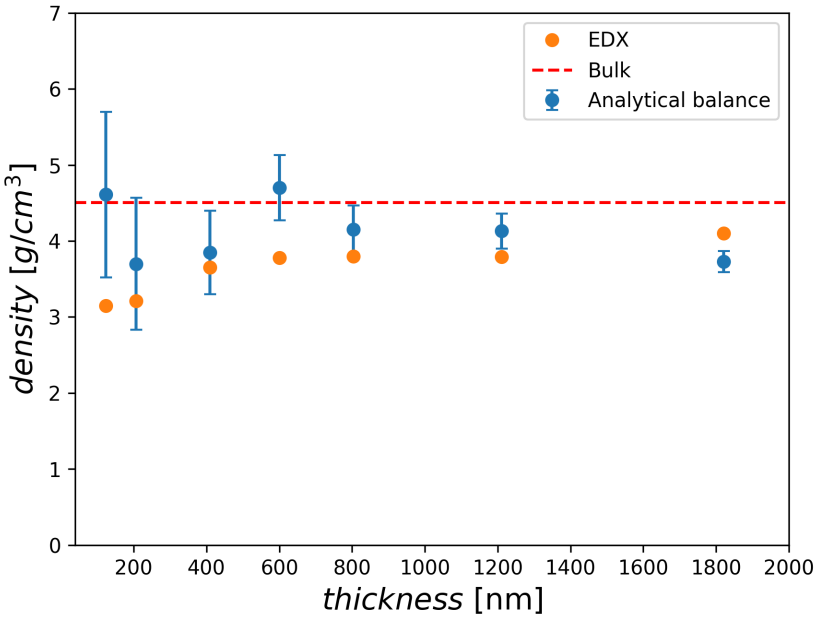

Figure 4.5. Measured values of density for the deposited titanium films. Results for both analytical balance (blue) and EDX (orange) methods are reported. A horizontal line at titanium bulk density is represented as reference.

The density was measured as a function of the thickness. The results are reported in Figure 4.5, where a line corresponding to titanium bulk density is drawn ($\rho_{bulk,Ti} = 4.506$ g/cm^3). As anticipated, values are obtained with two different methods. Uncertainties of the analytical balance measures are obtained through error propagation, while no uncertainty is reported for EDXS ones. That is because an estimate of them, and so of the accuracy of the measure, was not trivial at all for the reasons outlined in section 3.3. In particular, efficiency for titanium and silicon lines where experimentally estimated based on previously known sample measures. Moreover, the method has some uncertainties related to the Probability Function for X-ray Production (PFXP), in terms of the adopted model and cross section values. In this work by Prencipe et al. [83], this method is analysed also in terms of uncertainty, finding that a relative error of few percentage is usually observed. Nevertheless, little or no decrease of density with thickness is observed, despite one could expect that the increased amount of total DCMS deposited film, that is less dense, may lead to a less dense structure. In fact, though the relative fraction of DCMS and HiPIMS is the same for all the samples, in case of too high thickness of the lower density film, the energetic particles of HiPIMS could not be able to fill all the voids. Typical density values for pure DCMS are in the order of 0.65-0.7 of the bulk one, while the deposited samples reach a value always greater than $0.8\rho_{bulk,Ti}$.

4.2.3 Mechanical characterization

The knowledge of the residual stress state is helpful in understanding if the films could be able to remain intact as free-standing, that is crucial for the deposition performed directly on perforated holders, discussed in Chapter 5. Moreover, the stress is also related to phase transitions in polycrystalline titanium [80,84], despite in the deposited samples only or mostly α-Ti (hcp) is expected. Thus, substrate curvature method has been adopted to assess them as a function of deposited thickness. The uncertainties of the measures have been attributed as experimental standard deviation from a set of nominally identical samples. As typical for this technique, at low thicknesses the errors are quite big, as the film growth is not fully developed. Despite the film at 100 nm that presents a compressive stress around -1 GPa, all other samples show lower values of few hundreds of MPa at maximum. The stress evolution follows a compressive-tensile-compressive behaviour, getting closer to zero as thickness increases. A 4 layers, 800 nm thick hybrid film with 40 % HiPIMS instead of 20 % has been characterized as a comparison. While no significant differences were present in terms of density, the stress state was lower in module and opposed in sign: 526 ± 357 MPa versus -95 ± 83 MPa. It can be concluded that such low internal stresses, reached thanks to the layered structure, should not be too detrimental in the view of DLTs fabrication.

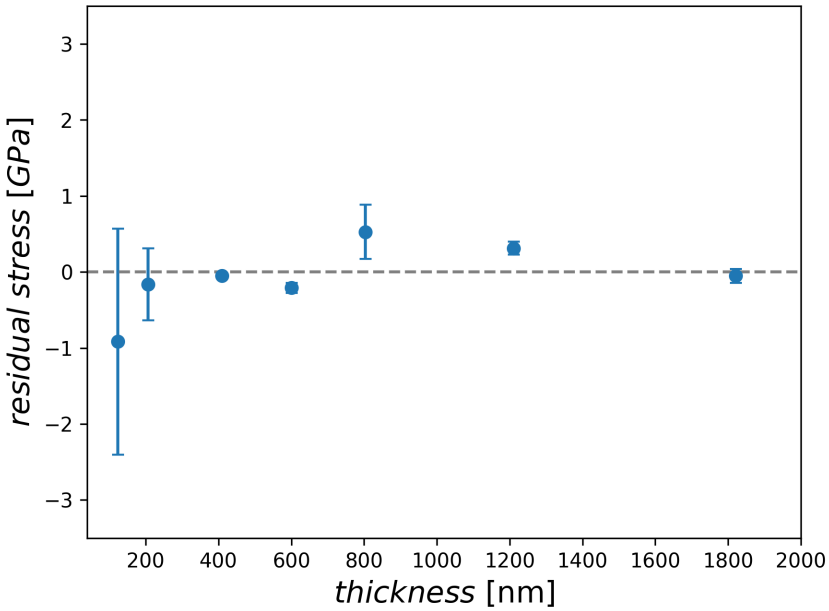

Figure 4.6. Residual stresses of 4 layers, 20 % HiPIMS films measured through substrate curvature method as a function of the thickness.

4.3 Carbon foams

4.3.1 Selected parameters for the depositions

The carbon foams deposited through fs-PLD were nominally all the same, meaning that the parameters were fixed. This choice arises from the fact that the focus of the work is on the coupling between the titanium film and the foam. As anticipated in Chapter 3, relatively high pressure and low fluence is needed to form porous fractal-like structures.

The procedure adopted for the depositions is as follows. A (silicon) substrate is put in the chamber, then pumps are started and vacuum is reached. While the sample is covered with the shutter, a laser cleaning of the pyrolytic graphite target is performed. The laser scans the surface drawing a spiral at fixed total speed (5 mm/s). The cleaning aims at making the deposition conditions as consistent and repeatable as possible, removing soot and particulate redeposited in previous operations. Argon gas can then be introduced to reach a pressure of 250 Pa. Because it has been found out that the continuous gas flux during ablation has an effect on the deposition, the chamber was isolated, closing the valves to both the pumps and the gas cylinder. Fluence is thus set to 360 mJ/cm^2 on target. The incidence circumference on the target is chosen as it does not cross a previous track and angular velocity is set so that tangential speed remains constant (this is to avoid too much digging when near the centre). Then, conditioning of the target, which means some seconds of ablation in the deposition conditions with the shutter still covering the substrate, is carried out. The substrate is at room temperature, not heated, and is made rotating at 11 *rpm* to allow for greater uniformity in the resulting film. The shutter is removed and the

deposition now takes place, lasting 10 minutes. A summary of the parameters is given in Table 4.3.

Table 4.3. fs-PLD foam deposition parameters.

Energy on target [mJ]	2.6
Fluence [mJ/cm^2]	360
Repetition rate [kHz]	1
Pressure [Pa]	250
Deposition time [min]	10

4.3.2 Samples characterization

Three main samples have been characterized, each differing for the substrate. One is a silicon wafer, the other two are titanium films deposited on silicon with the characteristics described in the previous section. In particular, one has a thickness of 200 nm and the other of 1200 nm. SEM micrographs allow to investigate the morphology of the foams. In Figure 4.7 (a)-(c), planar views at different magnifications of the foams are shown. All refers to the silicon deposition, as no appreciable differences are visible in the others. The foam appears as a web-like structure, with intertwined filaments spaced out by voids with variable dimensions, up to several microns. Some more globular particles are also visible, as typical of PLD. The surface coverage is good, as the substrate is not visible. A cross section of the sample deposited on titanium (200 nm thick) is also presented in Figure 4.7 (d).

The cross-views allow to measure the thickness of the foams, though it is much more difficult and delicate, compared to solid thin films. Indeed, the carbon structures tend to collapse under the bombardment of energetic electrons in the SEM, and the samples evolve during the observation. The retrieved values are thus rough esteems of the thicknesses, and uncertainties of more than 15 % are possible. It has to be noted that PLD is also characterized by a variation in deposited thicknesses up to 20 % in nominally identical conditions.
Average density is a particularly relevant parameter, as the near-critical material is the essential feature of the DLT (see section 2.3.2). The EDXS method has been employed to compute the mass thicknesses of the samples, from which the density can be retrieved dividing by the linear thickness. The same difficulties that has been encountered due to the change of the detector affected such measures. Thus, they have to be considered as preliminary results. In Table 4.4 the obtained values are reported. Also in this case, uncertainties are quite difficult to estimate, both on the thicknesses and the mass thicknesses. In particular, in the case where also titanium was present, the experimentally retrieved values for the revelation efficiencies of silicon were not in perfect agreement with each other. In addition, the presence of oxygen in both the carbon foam and in the passivating layer of titanium is also a problem for the computation of X-rays production intensities. The reported values are thus to be considered as indicative, and further measures are required in the future.

Given this, while a not so little difference is registered in the mass thickness, it seems to be mostly due to the linear thickness effect, as the densities are more

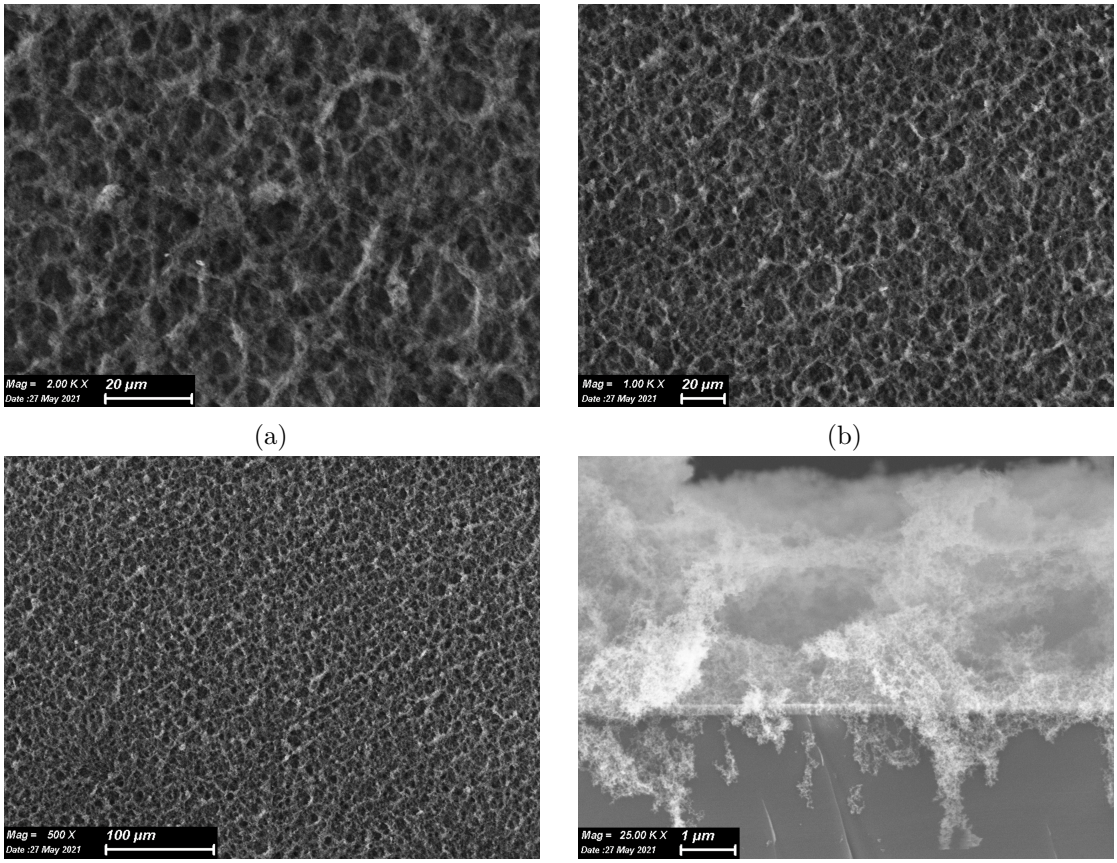

Figure 4.7. SEM images of carbon nano-foams. Planar views of the silicon substrate sample at (a) 2000 X, (b) 1000 X and (c) 500 X magnifications are shown. In addition, a cross section (d) of the foam deposited on the 200 nm titanium film is presented.

Table 4.4. Carbon foams properties.

	Silicon	Titanium 200 nm	Titanium 1200 nm
Thickness [µm]	10	16	12
Mass thickness [g/cm^2]	5.4×10^{-6}	9.8×10^{-6}	7.9×10^{-6}
Density [mg/cm^3]	5.3	6.0	6.5

similar one to the others, with a variation of less than 20 %. Because of the discussed experimental difficulties, it is not easy to understand if an effect of the titanium film on the foam deposition exists or not. Also, reproducibility of PLD depositions is to be accounted. Thus, this results can be considered as indicative of the possibility of producing foams with near critical densities, in the range $5 - 7$ mg/cm^3 employing the mentioned parameters. Moreover, they are useful for at least relative comparisons and considerations with regard to the deposition that will be discussed in the following chapter, i.e. on free-standing titanium films.

Chapter 5

Single and double layer targets on perforated holders

In this chapter, the methods and results concerning the production of double layer targets are addressed. In the first place, the target holders that have been employed and the technique adopted in order to obtain a free-standing film are described, also pointing out the critical issues. Then, the experimental results regarding the titanium films on the perforated holder are presented and discussed. Carbon foam depositions on the free-standing films are thus investigated. The effects of titanium thickness and surface features, along with the geometrical dimension of the holes, are considered. Lastly, a summary of the results and the issues that still need to be addressed is given.

5.1 Introduction and approach

5.1.1 Target holder and general strategy

As outlined at the end of Chapter 2, the main goal of this work is to investigate the production of free-standing targets directly on the holder, both as single and double layers, through magnetron sputtering and pulsed laser deposition.

The reference target holder for this thesis is made by SourceLAB, France. In particular, it is the one designed for the ion generation system named Kaio [85]. As shown in Figure 5.1, it consists of two masks made of stainless steel, each presenting a grid of holes. The two parts can be clamped together through a couple of screws, so that each hole on one side is aligned with one on the other. In the upper part, instead, an indent prevents the slide of one mask over the other. Moreover, two lateral guides do not allow the relative movements. A total of 165 holes are present on each target holder, arranged in 11 rows of 13 holes and 2 rows of 11 holes. Each perforation has a diameter of 1 mm, while the spacing between adjacent ones is about half a millimetre. The thickness of the steel in the drilled part is also of 1 mm.

Usually, a thin solid foil is put between the two masks and then they are clamped. Here, direct deposition of the target is performed on the side in Figure 5.1 (b), while the other part, Figure 5.1 (c,d), acts as a protection of the non irradiated shots during laser interaction experiments.

Despite being the reference target holder, the majority of the experimental work

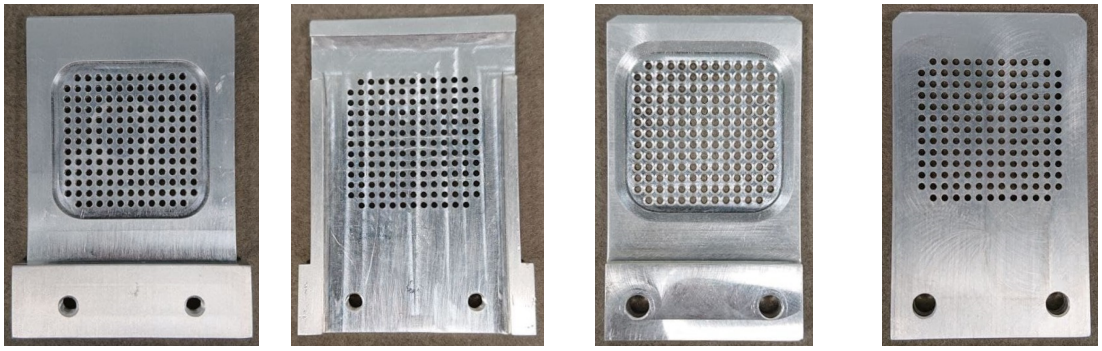

(a) (b) (c) (d)

Figure 5.1. Kaio target holder parts. Considering the front as the illuminated mask: (a) outer side of the back mask; (b) inner side of the back mask; (c) outer side of the front mask; (d) inner side of the front mask.

has been carried out on test holders (see Figure 5.2). They consist of a stainless steel slab with dimensions 5.5 cm × 4 cm × 1 mm. Two versions were employed, one with 4 rows of 9 holes for a total of 36 holes and the other with 6 rows of 9 holes (54 in total). In both cases, half of the perforations have a diameter of 1 mm and half of 1.5 mm. The main focus is on the smaller ones, as they are the same size as the reference holder holes.

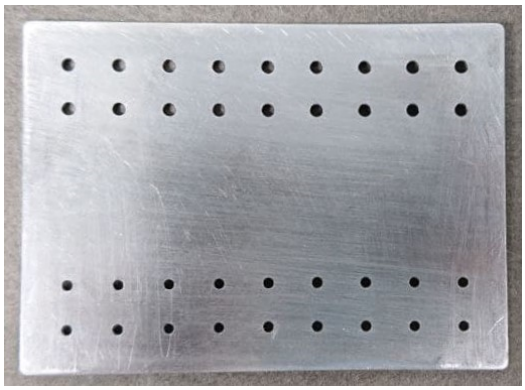

Figure 5.2. One of the perforated test holders employed in most of the depositions. In the lower part, 9×2 holes of 1 mm in diameter are present, while in the upper there are the other 9×2 holes with a diameter of 1.5 mm.

The choice of using a test component in place of the commercial one arises from the will of not deteriorate this last, as it is more sophisticated and expensive. Furthermore, the simple plate allows for faster cleaning from the deposited films, as it can be scrubbed with sandpaper, regardless of the scratches. On the other hand, the depositions on the target holder by SourceLAB can be removed through sonication plus mechanical removal of the film with adhesive tape.

In order to be able to deposit the films, the holes must initially be filled with some material. Then, after the deposition, such sacrificial substrate must be removed, so that a free-standing film is obtained. This is the general strategy adopted for the production of the targets. The details of the procedure are described in the next section.

5.1.2 Substrate preparation

The first step to make a perforated holder suitable for the deposition of a coating is to close the holes. In this way, a continuous surface on which a film can grow is obtained. The material to be used must have some characteristics, such as being soluble in an easily available and not dangerous to handle solvent, for example water. Moreover, it should not create excessive discontinuities at the edge of the hole after solidification and must be able to endure the temperatures that can be reached by the anode during magnetron sputtering depositions. In previous experimental activities [54], a procedure that employs sucrose have been outlined. A micropipette is used to deposit a specific volume of sucrose solution in each hole. As the diameter is sufficiently narrow, the drops remain in the holes by capillarity. Then, crystallization is carried out in vacuum, with a duration of about 5-6 hours. The process is thus quite long and tedious. Moreover, some defects like cracks and wrinkles along crystallization lines were present in the titanium film deposited on such substrate.

To overcome these limitations, a different material has been tested and then used throughout this work: caramel. Caramelization is a process that happens when a sugar is subjected to a thermal treatment at sufficient high temperature. In particular, sucrose has been used. Sucrose is a disaccharide formed by glucose and fructose. When heated, its molecules are firstly broken down into the monosaccharides of which it is constituted and then a complex series of chemical reactions occur. If the process happens at a temperature of around 170 °C, the so-called dark caramel is obtained, which quickly hardens as an amorphous solid. Not being crystalline, the problem of sucrose described above is no more present. Preparation time is also strongly reduced. Furthermore, the variation in volume during the hardening process is much less than the one following complete evaporation of water in the previously described method. Indeed, the control of the position of the substrate surface in the hole, and consequently the one of the target , is particularly relevant in high repetition rate experiments. The laser focus must be correctly on the surface to precisely know the intensity of the beam. Thus, if the target height changes significantly from shot to shot, the focusing operation must be performed for each hole, slowing the process and reducing the repetition rate.

To prepare the solid caramel substrate, in the first place the target holder is covered with silicon wafers on the side on which the deposition will take place. The wafers are fixed in position as tightly as possible, in particular using vacuum tape. In this way, a smooth caramel surface should be obtained, as the silicon is monocrystalline. The filling material can then be prepared, dissolving sucrose in water in a 2:1 weight ratio and bringing it to about 170 °C, when a dark colour is reached. In the meanwhile, the target holder should be heated up to the same temperature, so that the caramel will not harden too fast at contact. Finally, a thin needle is adopted to scoop the material and fill each hole. The holder is thus let cool down to room temperature, the silicon mask is removed and the component is ready for the deposition.

After the film has been deposited, the substrate must be removed without damaging the target. Caramel, as sucrose, is highly soluble in water. Thus it is sufficient to soak the holder in it and wait until the filling material is dissolved. This removal process can take place after the deposition of the metal film but before the deposition of the carbon foam, or after both. While in the first case no particular precautions other

than general care have to be taken, in the second situation the procedure is more delicate. Unlike the metal film, the foam is not water resistant and it will collapse in contact with it. Therefore, the holder must be kept horizontal in a vessel with the deposited face directed upward and the water level needs to be low enough to not touch the upper surface. Then, the water can be removed and the free-standing DLT recovered. In reality, as will be clear in the following, the substrate is better to be removed before the foam deposition, when only the titanium film is present. Thus, the just described complications are not relevant.

5.1.3 Critical aspects

Despite the advantages of using an amorphous solid and not a solution, like the surface texture and height, the relatively little time needed for the preparation, the ease of the whole process and the use of environment friendly materials (just sucrose and water), some drawbacks and issues are present. First of all, the caramel can present bubbles. The main problem with them is that the surface on which the deposition is made can be discontinue, resulting in a broken film. The majority of the bubbles can be removed by keeping the caramel hot, but at a temperature lower than 170 °C and waiting some seconds for their expulsion. Though some of them still remains and can affect some shots, a careful filling of the hole with the needle reduces this problem to a reasonable amount.

The major problem, however, is related to the silicon cover adhesion. If it is not perfectly adherent, some of the material can flow out of the holes, forming a very thin layer on the deposition surface. Depending on how bad the two surfaces are coupled, this layer can be a continuous one or can consists in a ring around the hole. In both cases, its presence is particularly detrimental for the films as it prevents them from sticking too the holder surface. In this way, as the sacrificial substrate is removed, the metal film detaches. As far as vacuum tape is used as fastening, this problem is often but not always present because of the intrinsic variability in the applied pressure when the silicon is blocked in position. To overcome this problem, a better adhesion is foreseen. In particular, a mechanical clamping, for example with the help of screws that fix the wafer between two plates, could be helpful in improving reproducibility.

Nevertheless, when the caramel leaks out of the holes, it is necessary to remove it. In order to do this, a dampened paper tissue is gently passed over the surface, trying to avoid to alter the surface in correspondence of the holes themselves. However, this procedure can be detrimental as the planarity of the filling surface can be lost and irregularities can arise. In particular, it is crucial when low thickness metal films are deposited.

One last issue could be encountered: the caramel can soften and deform at too high temperatures. This can be a problem in case of quite long depositions, i.e. of several hours, as will be better described in the following.

5.2 Free-standing titanium films

In this section, the realization of the single layer, free-standing titanium films will be described. As outlined in section 2.5, the interest in possible results is not only in view

of DLTs, but also in their use as simple targets in laser-matter interaction experiments. Thus, integrity is one of the most important characteristics to be investigated.

5.2.1 Integrity and surface morphology

Free-standing films were produced following the procedure described in the previous section on test perforated holders. Then, they have been observed at SEM. From the micrographs, it is possible to assess their integrity and the surface features of the films.

An example of the resulting samples is shown in Figure 5.3. In particular, it is a 200 nm thick film. The surface appears smooth and flat, with no visible topological features. Since the substrate on which the film grew was amorphous, no effects due to crystallization lines are present. The film looks intact, with no fractures. The hole edges are difficult to see, as the material continuously coat the holder. No systematic differences are observed based on the hole diameter.

A magnification (see Figure 5.3 (b)) of the surface shows a morphology analogous to the one described in section 4.2.2, with relatively small globular grains.

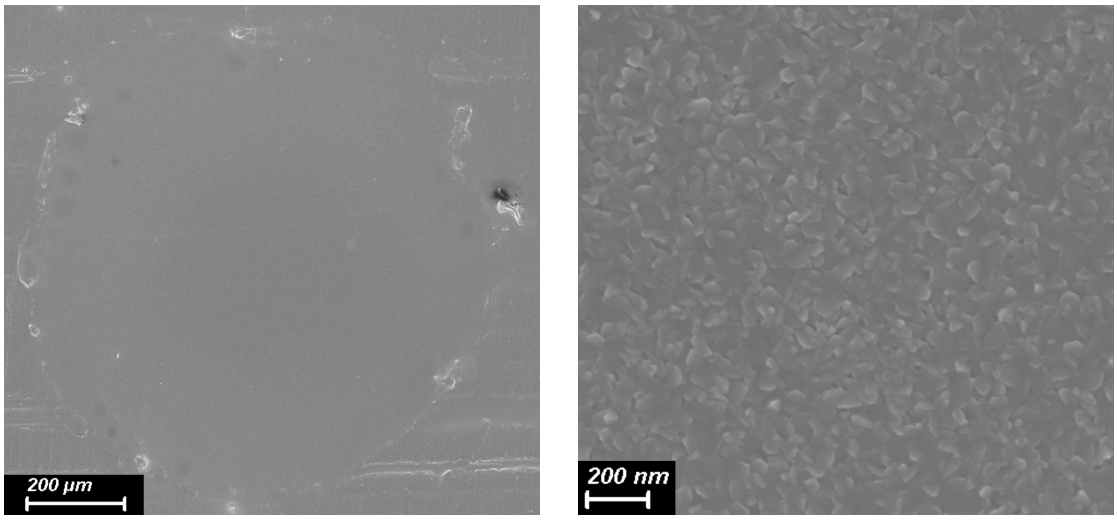

(a) (b)

Figure 5.3. A 1 mm diameter, 200 nm thick free-standing titanium film on one of perforated test target holder. (a) The whole film and (b) a magnification of the surface.

Nevertheless, not all the films result as perfectly intact. While the possible observed defects will be described in section 5.2.2, here it can be noted that, depending on the film thickness, the fraction of undamaged samples can vary. A scan between 50 nm and 2000 nm has been carried out. It has been found that in range between 200 nm and 1200 nm, the survivability, i.e. the fraction of intact free-standing films over the total, can be estimated to be around 80-90%, up to 100% in some cases. The main characteristic affecting the reproducibility seems to be the sacrificial substrate quality. Indeed, it has been observed that having a flat and levelled caramel surface is more important to achieve good adhesion and integrity as the deposited titanium thickness is decreased. In addition, it has been noted that, in general, better results are obtained when depositing on the Kaio holder with respect to the test one. This can be probably

due to the better surface quality of the component and to the possibility of avoiding major leakages of caramel during substrate preparation. In fact, the reduced surface that has to be covered allows for better silicon adhesion, despite still not optimal.

Outside the above mentioned interval of thicknesses, the performed depositions showed several difficulties in achieving acceptable results in terms of integrity. At low values, deposition of 50 nm films of three different kinds have been tested: the usual 20% HiPIMS, 4 hybrid layers film; a 8 hybrid layers film with 20% HiPIMS; a 40% HiPIMS and 4 hybrid layers film. For all the samples the film broke or detached when the substrate was dissolved in water. Two other low thicknesses were investigate, that are 100 nm and 150 nm. In this cases, only the 4 hybrid layers with 20% HiPIMS were deposited. Most of the 100 nm films broke, but the few (around 20%) that were intact resulted as flat and with good adhesion at the edges, as can be seen in Figure 5.4. This observation suggests that the problems are due to the substrate and not to the film. Similar considerations can be made in the 150 nm case, although the survivability of the films increased to about 50%.

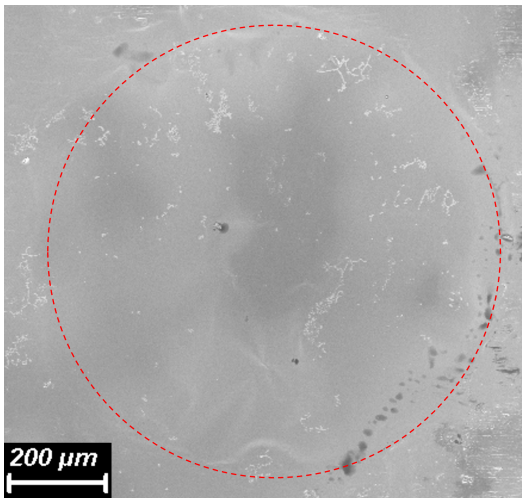

Figure 5.4. One of the intact films with a thickness of 100 nm. The edges are highlighted for clarity.

A single deposition of a 2 µm thick film was tried. The total duration of the sputtering process was of slightly more than 5 hours. Thus, when the sample was removed from the vacuum chamber, it resulted as quite hot and the caramel was altered, swollen on back side. As a consequence, the film was damaged or deformed. A limit for the caramel substrate technique is thus found, as it does not allow for too long depositions. This limits also the possible attainable thicknesses, unless some variations are introduced. As an example, consecutive depositions with a pause to allow the cooling of the anode can be thought, although a possible adhesion problem between the steps can arise. Another alternative could be to reduce the time for the same thickness, i.e. increasing the deposition rate. To achieve this, it could be possible to deposit a stable, denser base film with the usual 4 hybrid layers with 20% of HiPIMS and then proceed up the desired thickness with pure DCMS (the deposition rate of DCMS is about 4 times the HiPIMS one, as seen in section 4.2).

Between the first and the last depositions, several months have passed. Thus, it was possible to assess if the films would damage over time both as free-standing and

with caramel substrate underneath. No substantial variations have been observed in the titanium in both cases, though the substrate is prone to humidity absorption if left in atmosphere, which makes it become sticky.

5.2.2 Types of defects

As anticipated, in this section a list of encountered defects and their possible causes are presented. One of the most common consists in little cracks that starts at the edges of the covered hole, that are the weakest part of the film, and then propagate toward the centre of the free-standing film. An example can be seen in Figure 5.5, where a magnification is also presented. The crack width, in this case, is of about 3 µm. The possible cause of this kind of damages is mechanical solicitation that could also be enhanced by the concentration of stress due to the initially non-planar substrate surface. If the caramel is not levelled with the hole edges, once it is removed the film will feel a stress additional to the intrinsic one. In other cases, the film appears with some little holes over the surface, whose origin is not clear and can be various kind (see Figure 5.6).

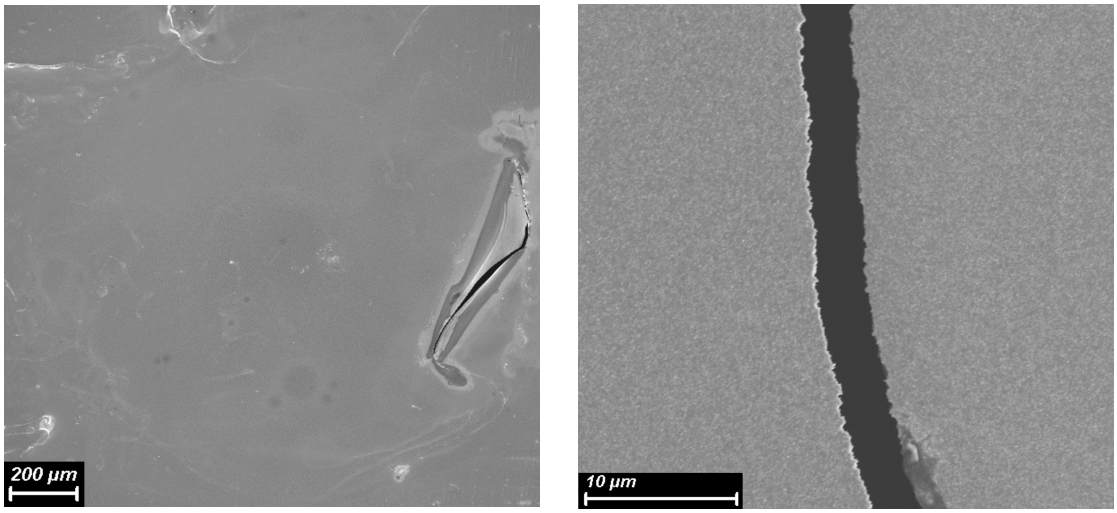

(a) (b)

Figure 5.5. SEM images of the cracks that can possibly form on the free-standing films. (a) The cracked film and (b) a magnification of a crack.

When the caramel leaks out of the silicon mask and has to be removed by cleaning the target holder to avoid defects like the described cracks, the substrate surface loses its flatness. Thus, wrinkles and corrugations can arise and be transferred to the film. Figure 5.7 shows this possible effect. It can be seen that the film is not flat, but its integrity is kept. This kind of issue should not be particularly detrimental.

Another problem related to the caramel substrate is the presence of bubbles. Indeed, if some air is trapped in the material, it will expand in vacuum, in the end causing blistering of the titanium film. A similar phenomenon could occur due to incomplete wetting of the silicon, resulting in a caramel surface not perfectly smooth, with some voids. Two examples are shown in Figure 5.8. Damages like this compromise

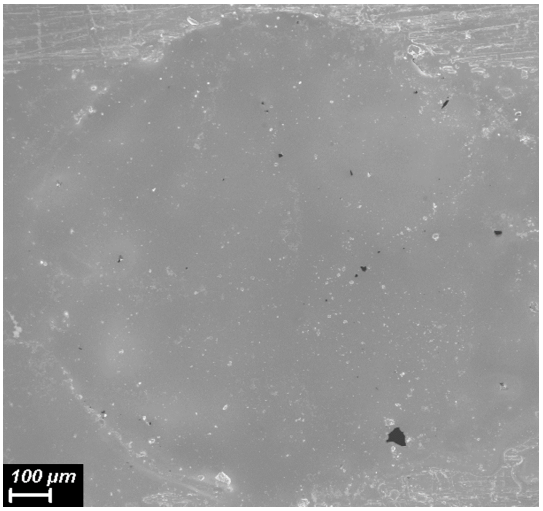

Figure 5.6. The black spots over the surface are little holes in the film. Their dimension is of some micron in diameter.

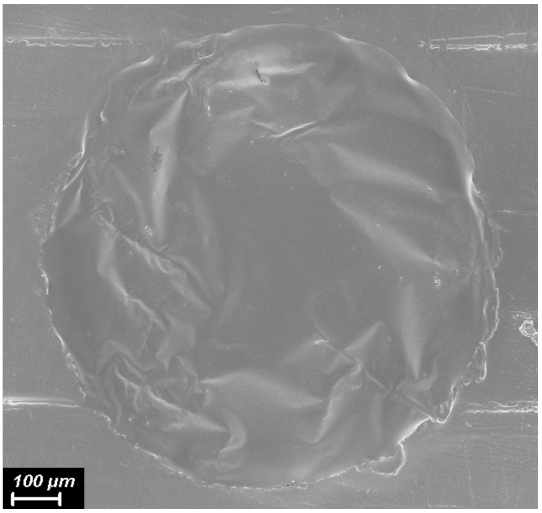

Figure 5.7. An intact free-standing film with corrugated surface.

the integrity of the film and thus their usage as targets in laser interaction experiments. A careful preparation of the substrate reduces their occurrence.

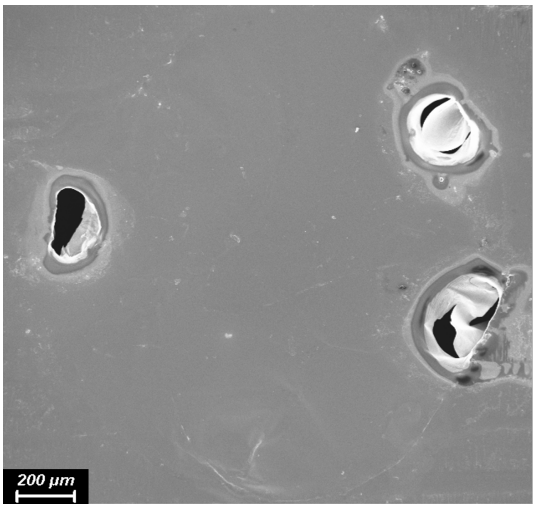

(a)

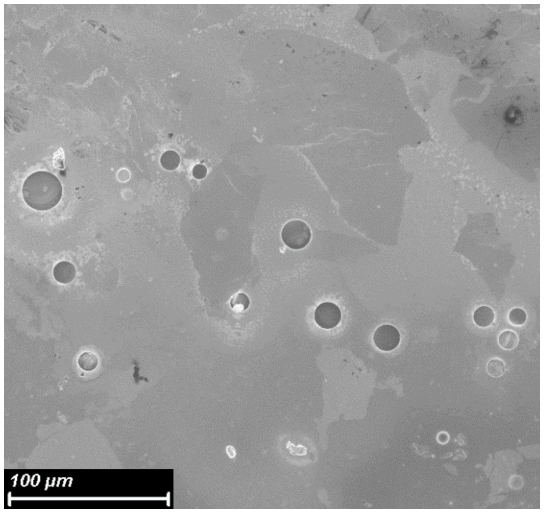

(b)

Figure 5.8. Two examples of the blisters and bubbles that could compromise the free-standing film integrity.

Lastly, some dirt or foreign bodies can easily deposit on the substrate prior to the titanium deposition. If this happens, such materials will remain incorporated in the film, altering the surface. In particular, the material could come from the process of cleaning from the excess caramel, that thus requires to be performed with adequate attention and materials.

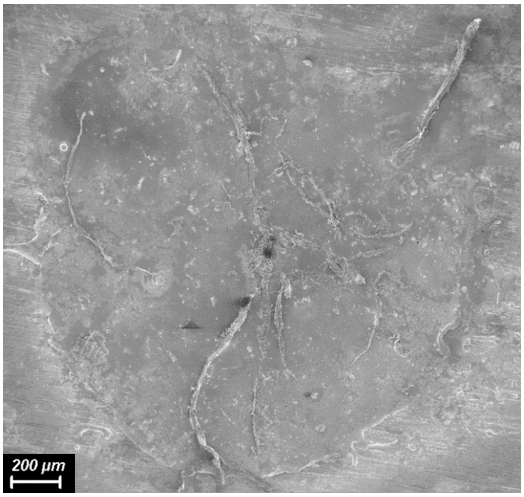

Figure 5.9. Image of a titanium film with incorporated extraneous materials in it.

5.3 Carbon foam and double layer targets

To investigate the production of double layer targets, carbon foam has been deposited on the just described titanium films, according to the procedure and parameters outlined in section 4.3.1. In the first place, studies were conducted on free-standing metal on the perforated holders. Then, some tests keeping the sacrificial substrate underneath the titanium layer during the foam depositions were also performed. In this context, an experimental difficulty can be reported regarding the Kaio holder. Since it is quite thick, it does not allow for the closure of the pulsed laser deposition system shutter. Thus, after laser cleaning and conditioning, vacuum has to be broken to put the sample in the chamber. In this section, the results and observations of this experimental campaign will be presented.

5.3.1 Foam deposition on free-standing films

The depositions of carbon foam through fs-PLD were conducted on free-standing titanium film with thicknesses in the range $200 - 1200$ nm. SEM images showed a clear difference between the 200 nm and the other ones. In this case, a much lower amount of material is present on the free-standing region. Moreover, a decrease in the surface covering along the radial direction, from the edge toward the centre, is present. Figure 5.10 shows a comparison between depositions on a 200 nm and a 400 nm thick metal layers. Magnification of the periphery of the free-standing region is also shown to highlight the effect: while no clear distinction is seen in Figure 5.10 (d), it is not the case for 200 nm film (Figure 5.10 (b)). Between the thicker cases, the qualitative differences in the covering are less evident, though the deposition seems to be more homogenous with increasing thickness. In Figure 5.11, the results on a 800 nm film is shown: the hole edges are hardly distinguishable. These observations, i.e. the thickness and the radial dependence of deposited material, could suggest that the vibrational solicitation of the film due to the impinging carbon clusters and the target holder motion prevents the further adhesion of aggregates and/or their partial detachment. As in elastic membranes vibrations, a mass, and thus thickness,

dependence of this phenomenon is foreseen.

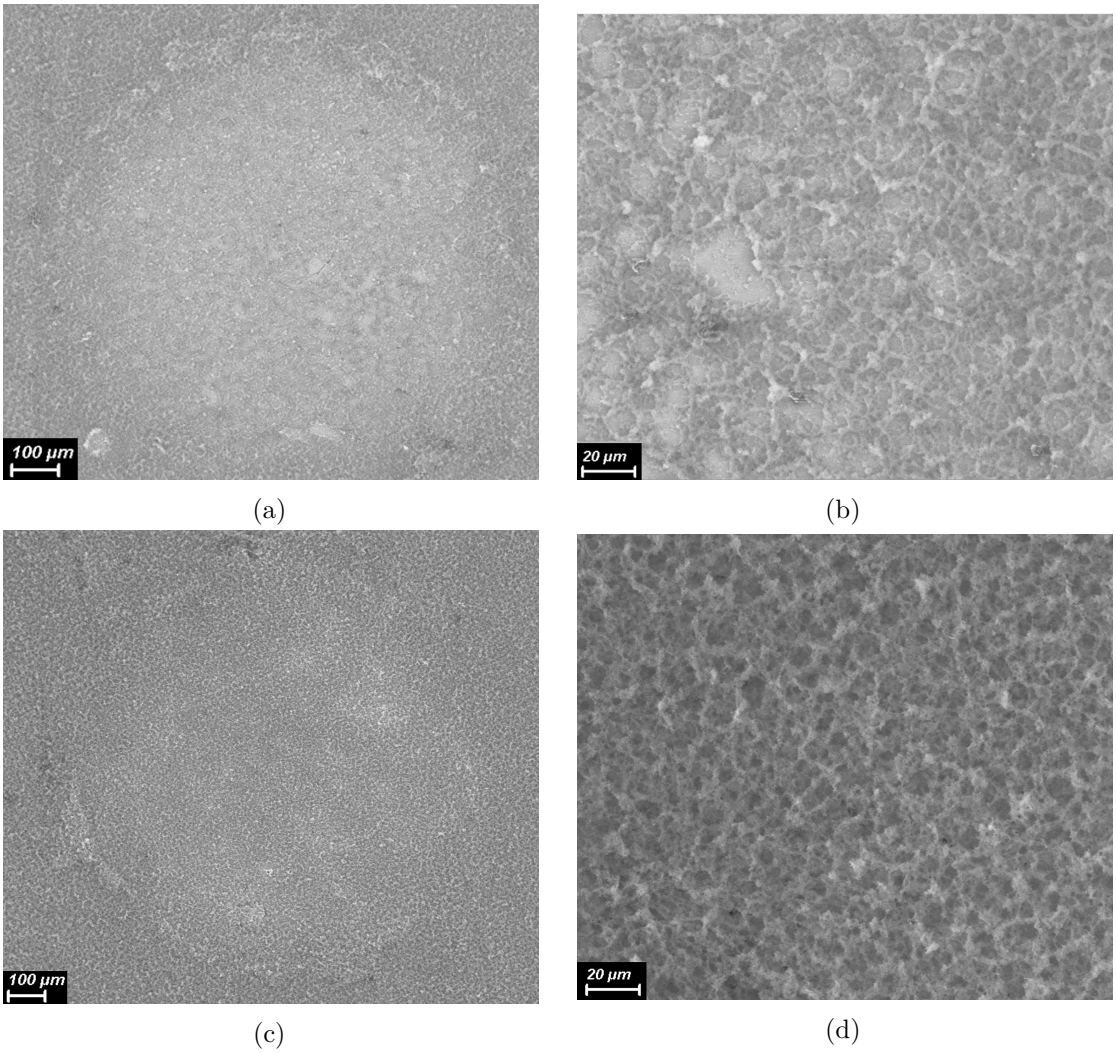

Figure 5.10. SEM images showing carbon foam depositions on free-standing titanium films. A clear difference is visible between the case of a 200 nm metal film (a,b) and 400 nm one (c,d). The peripheral magnifications (b,d) highlight the phenomenon.

To support this hypothesis and to have also a quantification of the deposited material, mass thickness estimates through the EDXS technique (see section 3.3.2) were performed. Due to the already described experimental difficulties related to the change of the X-rays detector during the thesis work, the results are more valid as a relative comparison than as absolute values. In addition, the measurement of the foam thickness through cross-section method is not possible in this case. Indeed, the steel holders cannot be cut as it is done with silicon wafers. Thus, since other techniques that allow to assess film thickness were not available, foam density values could not be retrieved.

In Figure 5.12, the resulting carbon foam mass thicknesses as a function of free-standing titanium layer thickness are presented for both 1 mm and 1.5 mm holes. As a comparison, the two horizontal lines represent the values computed for the samples

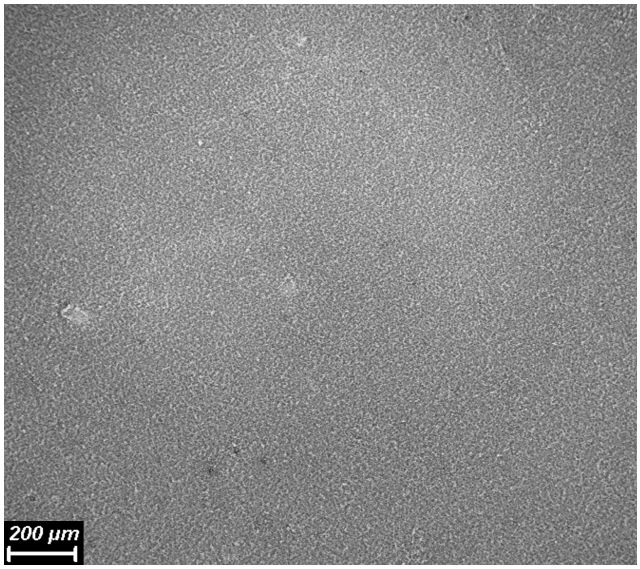

Figure 5.11. SEM image of carbon foam deposited on a 800 nm thick free-standing titanium films. The periphery of the free-standing region is hardly recognisable.

deposited on titanium with silicon substrate, already discussed in section 4.3.2. They are used as references.

It can be seen that the mass thickness corresponding to 200 nm is considerably lower, about halved, than the other values and, considering the SEM images, it is clearly due to the lower quantity of material that is deposited. On the other hand, the foam layers deposited on films with greater thickness present less variability. In particular, it is comparable to the difference between the two reference samples. As discussed in 4.3.2, the deposited thickness can be quite different between depositions nominally identical. Thus, the difference in mass thickness could probably be ascribed to variation in thickness at approximately constant density. Indeed, if a density of 6 g/cm^3 is considered, the highest difference in mass thickness, i.e. the one between the 600 nm and the 1200 nm samples, would correspond to about 5 µm. Nevertheless, without a separate measure of thickness, it is not possible to state if an increasing trend in carbon foam mass thickness with titanium thickness is present or not.

On the other hand, a systematically lower mass thickness is observed comparing the simultaneous foam depositions on free-standing films on the holes with greater diameter. This result is compatible with the above stated hypothesis of membrane vibrations, as a greater diameter allows for higher displacements. Thus, in the case of production double layer targets, the perforation diameter of the holder play a role, unlike what has been observed for simpler single layer targets.

A possible dependence on titanium's superficial morphology of carbon clusters adhesion on free-standing films was studied. Two different magnetron sputtering depositions were performed in order to get a smoother and a more rough surface. In particular, foam was deposited on 4 hybrid layers with 20% HiPIMS films with a thickness of 350 nm on top of which were added 50 nm of pure DCMS in one case and of pure HiPIMS with a bias of 50 V in the other. As seen in section 4.2.2 and in particular in Figure 4.3, in DCMS the grains are bigger and more jagged, since the sputtered species have relatively low energy. HiPIMS films, on the other hand present

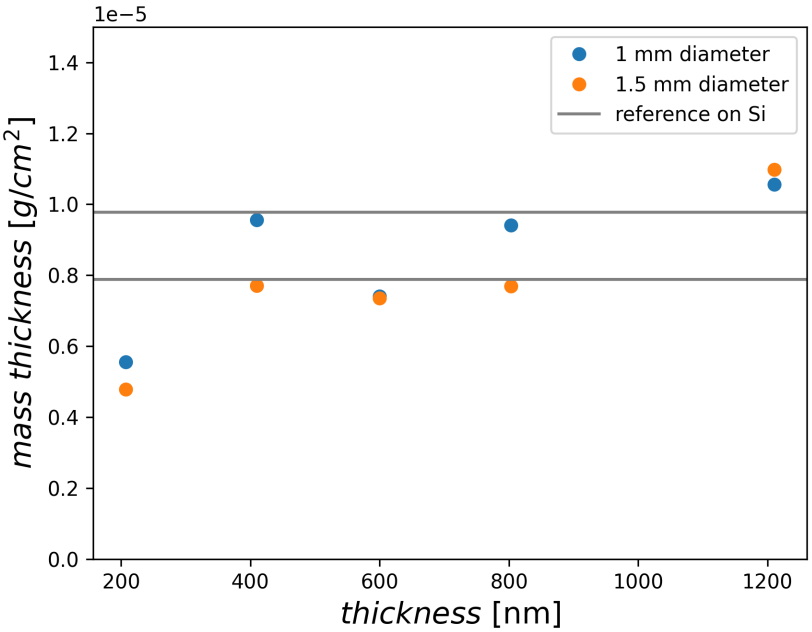

Figure 5.12. Plot of measured carbon foam mass thicknesses on free-standing titanium films as a function of the metal layer thickness.

more round and regular grains. The SEM images and mass thickness measurements, anyway, showed that no significant dependence on this characteristic is present.

5.3.2 Foam deposition in presence of caramel substrate

Despite the complications described in section 5.1.2 that arise if the sacrificial substrate has to be removed after both layer depositions, this strategy could possibly overcome the limitations encountered with low thickness free-standing titanium films.

For the whole thickness range, carbon foam was thus deposited on holders in which half of the metal films were free-standing and the other half with caramel still underneath, so that a direct comparison was possible. In terms of uniformity, better results are achieved and on the thin films a good coverage is also obtained. In particular, the carbon layer appears similar to the one presented in Figure 5.11 in all cases.

Nevertheless, several issues are encountered, regardless of the metal film thickness. In several cases, near the edges, titanium films that were intact prior to the PLD deposition seems to be broken, so that the caramel substrate is exposed. Moreover, nearby these regions the foam is reduced, as if it was incorporated in the substrate. An example of this behaviour is shown in Figure 5.13 (a,b). Another problem, presented in Figure 5.13 (c,d), consists in holes in the deposited film that expose the substrate.

Which is the origin of such issues is not clear, but their very high occurrence makes the strategy of removing the caramel substrate after the foam layer deposition not feasible.

Moreover, the damages to the film tend to evolve in time. Indeed, the observation with the naked eye of the same samples after some weeks showed that, in presence

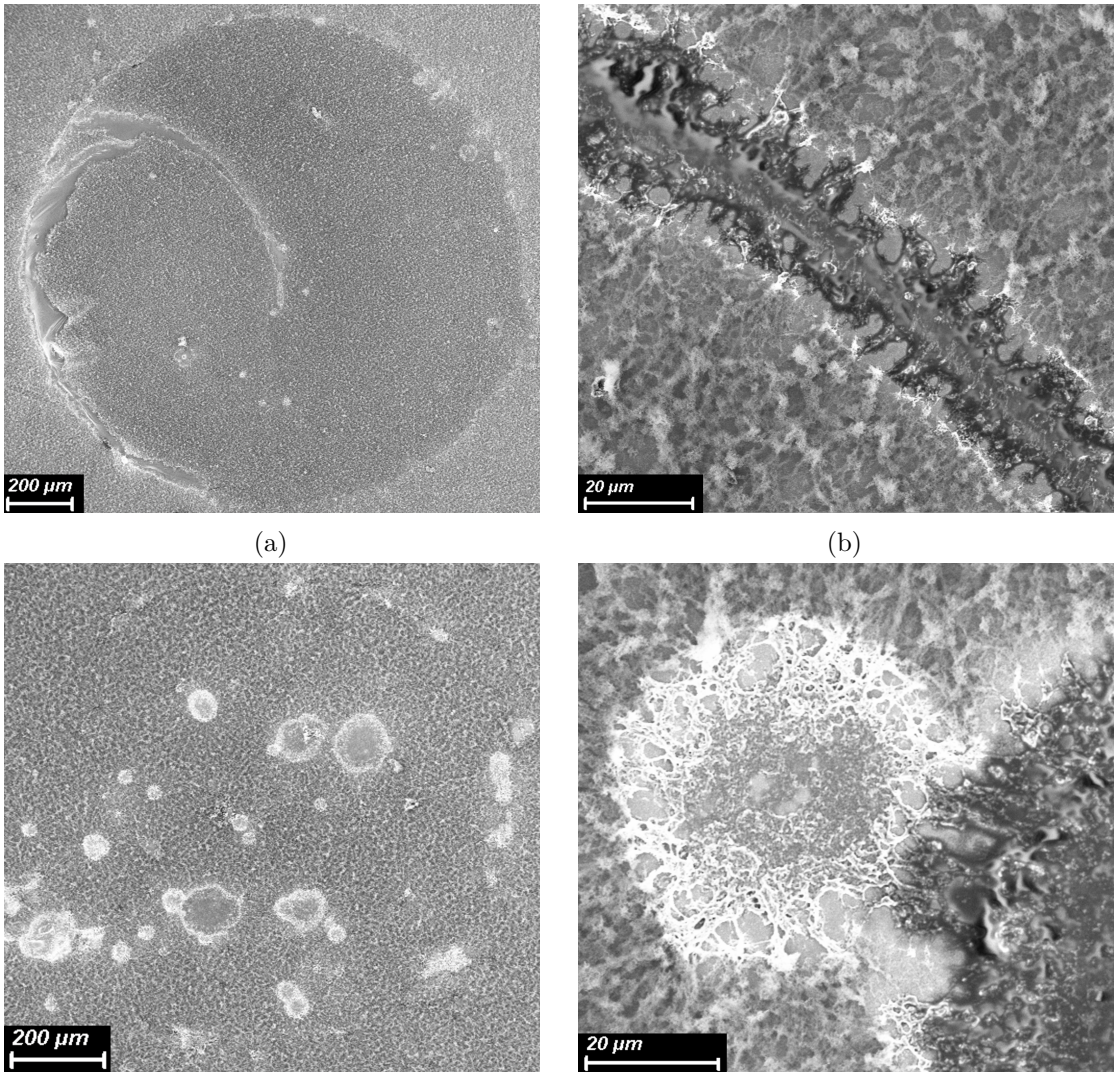

Figure 5.13. SEM images showing two examples and their magnifications of the damages and issues observed when depositing carbon foam on samples with caramel substrate underneath.

of the sacrificial organic substrate, the foam was significantly reduced in quantity. Looking at it through electron microscope, its morphology appears as changed, showing more compact structures with long filaments. On the other hand, no variations in time are observed when the double layer films are free-standing, so that they can probably be stored without particular precautions, keeping in mind that the foam is quite fragile and can wrap or detach under solicitation.

5.4 Summary of results

A procedure to deposit free-standing films on perforated holder has been developed. The holes of the holders are first filled with caramelized sucrose, a solid amorphous material, exploiting a silicon mask to prevent its spilling while soft and to obtain

flat surfaces. Once this substrate has hardened, the depositions can take place and afterwards the substrate removed by dissolution in water. In particular, both single titanium film and carbon foam-based DLTs have been tested. The integrity as function of thickness has been assessed and an interval of feasibility is identified. Between 200 nm and 1200 nm, flat and uniform films are obtained and the average integrity sets to around 80-90% of holes. At lower thicknesses, instead, worse results are observed. On the other hand, at higher values an issue with the substrate arise, as it softens due to the too intense solicitation that heats it up. This causes damages to the titanium film, so other strategies has to be found. Nevertheless, several problems are identified even in the mentioned interval: cracks, holes, blisters and wrinkles can be present in 10-20% of the holes. The main causes are to be attributed to the substrate, which can be not levelled with the holder surface, can retain air bubbles or not completely wet the silicon wafer.

As regards the double layer components, the metal thickness play a role in determining the amount of deposited foam and its uniformity. Indeed, on 200 nm thick free-standing titanium, a clear reduction in the quantity of carbon is observed radially. The combination of mass thickness measurements through the EDXS technique described in section 3.3.2 and SEM observations suggested that this effect is already strongly reduced on 400 nm thick films. Moreover, the systematically less mass thickness of carbon on the free-standing films with greater diameter (1.5 mm instead of 1 mm) support the hypothesis of an elastic membrane vibrations induced in the titanium film by the impinging foam clusters, that also explains the thickness dependence.

Depositions on non-free-standing metal films, i.e. with the organic substrate underneath, have been tested. Despite the improvement in foam uniformity, that in this case is comparable among all the different thicknesses, unexpected issues arise. Holes and cracks on previously intact titanium films that expose the caramel are observed and peculiar interactions between it and the foam modify the morphology.

A modification in time, over weeks, is seen when the carbon foam is deposited in presence of the caramel substrate, which appears more compact and reduced in quantity. Instead, no variations after some time are observed in the free-standing single and double layer films, suggesting no particular problems in target storage.

Chapter 6

Conclusions and Perspectives

The goal of this thesis work was to investigate the production of targets for laser-driven particle sources exploiting direct deposition of solid films on perforated holders. Titanium films deposited through magnetron sputtering and low density carbon foams obtained exploiting femtosecond pulsed laser deposition were considered. Since the focus was on the assessment on the effective possibility of producing real components, the parameters of the depositions were kept fixed throughout the study. Their values were chosen according to previous studies, papers and preliminary depositions. Morphological, structural and mechanical properties of the films were measured. In particular, the titanium films resulted in relatively low residual stresses and densities close to the bulk one (greater than 80 % of it), while the carbon foams have densities of few mg/cm^3 and appear as uniform and highly porous.

A procedure to obtain free-standing film was developed. The perforated target holder is firstly masked with a silicon wafer on the side on which the deposition will take place. Then, its holes are filled with an amorphous solid material: sucrose dark caramel. After the filling material has hardened, the mask can be removed and the metallic thin film deposition can be performed. To make the films free-standing, the organic substrate is removed by placing the holder in water, since caramel is highly soluble.

Different titanium film thicknesses were investigated in order to identify a range in which it is possible to produce free-standing targets. It has been found that between 200 nm and 1200 nm, on average, about 80-90% of the possible shots result as intact. This is interesting both for sole titanium targets and for realising double layer targets. In fact, compared to commercial metal foils, also lower thicknesses are accessible. In addition, magnetron sputtering deposition allows for more uniformity in thickness and less uncertainty in its value, about 5% instead of 30%. Since the maximum energy of the accelerated protons strongly depends on this parameter, a greater control on it is particularly important to assure reproducibility.

In relation to DLTs, carbon foam was deposited on free-standing titanium films in such thickness range. While on the thinner ones a low amount of material remained, above 400 nm thick films a uniform covering is obtained. This indicates that it is possible to produce advanced foam-based targets in such range with good results.

Nevertheless, several limitations and issues have been identified, concerning both single and double layer components. It was found that the caramel substrate has a very important role, in particular when low thickness films have to be deposited.

Indeed, if its surface is not levelled with the holder, or if it is not smooth, the metal can break or wrinkle. Titanium films with a thickness lower than 200 nm are thus particularly critical and their integrity is harder to assure. This problem could possibly be overcome by improving the adhesion of the silicon mask on the target holder. On the other hand, when too long depositions are considered, the organic substrate can soften due to its heating and thus the deposited films can be damaged.

Regarding the interaction between the materials, the difficulties encountered when the metallic layer is too thin are probably consequent to mechanical vibrations of the free-standing film. Thus, it could be thought to postpone the removal of the sacrificial substrate after both the depositions. Unfortunately, it has been observed that, following this procedure, several originally intact titanium films result damaged after the foam covering. This is not the case when the deposition is performed on free-standing elements. Thus, a peculiar interaction seems to occur between the materials.

To summarize, in this thesis work a procedure for producing free-standing targets for laser-matter interaction experiments has been outlined. Specific films depositions were tested, and the range of the applicability of this procedure in terms of film thicknesses were determined, both for single titanium and in combination with near-critical carbon foam. Deposited films are a valid alternative to conventional metallic foils, as they allow to achieve high uniformity with great control on the thickness and without significantly affect the density of the metallic layer.

Though, further improvement and experimental investigations are foreseen. First of all, a better and more constant adhesion of silicon on the holder surface is needed, in order to increase reproducibility and, possibly, be able to obtain even thinner free-standing titanium films. In this regard, mechanical clamping can be a possible solution to test and it could also imply little modifications in the target holder design.

On the foam side, a further study of the effect of the deposition parameters on the density, uniformity and reproducibility is advised. Also, better and broader investigations on mass thickness and the interaction of the foam with the metallic film is necessary. Density maps would allow a more quantitative description of the uniformity of depositions and Fourier analysis of SEM images could give insights on the morphology, like typical aggregation dimension. Since the density is of particular relevance in laser-matter interaction, it should be developed a procedure to assess it even in the free-standing case. That is, an independent measure of the foam thickness should be known.

Furthermore, the investigation can proceed also towards other materials. In fact, only titanium and carbon have been considered in the work, but, potentially, other metals or multi-elemental compounds could provide good or better results. It could be also though to try to produce both layers with the same material and technique (i.e., PLD) by properly changing the parameter of the deposition to initially obtain a solid and compact film and then a porous one.

Lastly, the targets produced according to the developed procedure should be tested in laser interaction experiments. In this way, the predictions on the resulting accelerated particles could be confirmed or denied. Comparison with conventional targets would highlight the possible improvements, in particular in terms of reliability and reproducibility. New and unknown issues and features could be found, thus gaining indications and insights on how to proceed in the optimization of engineered

targets for laser-driven particles sources.

Appendix A

ASPRI additional work: 2D particle-in-cell simulations

In this appendix, the additional work done in the context of the ASPRI programme is presented. The ASPRI programme is a high level training opportunity offered by the Politecnico di Milano for the specialization of their students. The programme is structured throughout the traditional degree path in Nuclear Engineering and gives the opportunity of deepening some aspects of the student's training. For this purpose, additional activities for a total of 20 extra credits are foreseen. In particular, they are devoted both to courses and extended master thesis work (5 credits).

This work has been devoted to the theoretical investigation of the behaviour of the developed targets under laser irradiation. A numerical investigation has thus been performed. In particular, 2D Particle-In-Cell (PIC) simulations are employed in order to assess the effect of the thickness of the titanium film in the double layer targets developed in this thesis. In particular, a parametric scan is performed in two very different laser intensity regimes, comparing simple metallic films and DLTs. Proton generation from Target Normal Sheath Acceleration (TNSA) is the main focus of the study, considering their maximum energies and their spectra.

A.1 Generalities and goals

Particle-In-Cell (PIC) is a technique used to solve a certain class of partial differential equations, particularly popular in plasma simulations. In this context, it is adopted to solve the kinetic description of plasma. In the following, a brief description of this method is given. A more detailed description of PIC methods and their functioning can be found in the papers by Dawson [86] and by Arber et al. [87]. The trajectories of charged particles (electrons, ions) are followed in the self-consistent electromagnetic fields computed on a fixed mesh. It is a relatively intuitive and straightforward method to implement that allows for relativistic description and in some case can also implement collisions among particles. The core of a PIC code consists of two coupled solvers: the *particle pusher* and the *field solver*. The particle pusher moves the charged particles continuously in space under the influence of electromagnetic fields and calculates the currents due to the particle motions. On the other hand, the field solver finds the solution of Maxwell's equations on a fixed spatial grid subject to

the currents calculated from the particle motions. The most used algorithms are the Boris pusher for the particles motion [88] and the Yee solver for the fields [89].

Due to the typically huge amount of particles present in a plasma, they are simulated in the form of collection of particles, called *super-particles* or *macro-particles*. Each of these macro-particles is representative of many real particles, whose number is determined by a chosen weight, and so their mass and charge are scaled accordingly. It has to be noted that the particles are described continuously in space and have a finite volume, while the fields are computed only in fixed points. This means that, in general, the electric current density at the mesh points and the electromagnetic fields at the macro-particles positions are not known. Thus, some methods to compute them are needed, i.e. current has to be "deposited" on the grid and the fields have to be interpolated to the particles positions. In order to do so, another important element has to be introduced: the *shape function*. It is a spatial function centred around the macro-particle position that describes its extension and allows for the computation of fields and current density through a convolution operation.

To summarize, after the particles and fields have been initialized, the following main steps are repeated sequentially for each time:

- the fields are interpolated to find the force that acts on every macro-particle;
- the macro-particles are moved by solving the equation of motion (particle pusher);
- the electric current density related to the macro-particles is projected on the mesh points;
- the new fields are computed by solving the Maxwell's equations (field solver).

As an example, in laser-plasma interaction simulations the fields are initialized to model the laser pulse as a wave with a specific spatial shape, often a Gaussian one, and the particles as a spatial distribution described by a specific function. Since the computational cost of such investigations is typically very high, parametric analysis can be performed in a reduced dimensionality, i.e. 2D instead of 3D. In this way, much less computational resources are needed.

Through PIC simulations, several information can be retrieved for any time-step: the positions and momenta (the phase space) of each macro-particle for all the charged species, the values of the electric and magnetic fields at each mesh point and all the quantities that can be computed from them. For example, kinetic energies, energy and/or angular distributions of particles, mass and charge density distributions... In the context of laser-driven particle acceleration, this allows to understand which kind of results can be expected and can also guide the improvement of the target design or the tayloring of it based on the needs.

Many particle-in-cell codes exist. In this work, the open-source code Warp-X [90], developed by the US DOE Exascale Computing Project, has been used. The main corresponding references are two papers by Vay et al. [91, 92]. The choice of this specific code follows from its possibility to perform the computations on GPU-based supercomputers. In fact, Marconi100 [93] high performance computing cluster by Cineca, based on GPU architecture, was the one available and has been used for all

the simulations. As for the data analysis, openPMD [94] meta-data scheme together with Python scripts have been adopted.

The main interest of this work is to study proton acceleration by TNSA from different targets in two different laser intensity regimes. The references for the choice of these regimes can be considered Kaio by SourceLAB [85] and Apollon [95]. The first one is relevant as its target holder has been employed in the production of the samples described in Chapter 5, while the second one is a Petawatt-level facility in France. The investigated one are simple titanium films, in the following called SLTs, and DLTs made of carbon foam over titanium. While the characteristics of the low density material have been kept constant (in thickness and density) in all the computations, a scan varying the metallic layer thickness have been performed for both target configurations. The considered values are the one described in the Chapters 4 and 5, i.e. $200, 400, 600, 800, 1200$ nm. The effect of the incidence angle in the case of a SLT is also considered. All the parameters adopted in the simulations are presented in section A.2.

In the section A.3, the results of the numerical study will be presented. Considerations common to the analysed cases are made, as the visualization of self-focusing effect in the near-critical plasma, the angular distributions of protons and the laser energy absorption. Then, to conclude, the contaminant proton energy spectra from all the different simulations are compared, in particular in terms of maximum kinetic energies and temperatures of the distributions.

A.2 Simulation parameters

As previously stated, PIC computations require the choice of the algorithms used for the solution of the differential equations that describe the system. In the performed simulations, Boris pusher and Yee's field solver are adopted. The shape function associated to the macro-particle is a third order one, which means a combination of parabolic functions. The simulation domain is a 2D box of 70 μm × 70 μm, divided in 7000 × 7000 cells (i.e. 100 cells per micron for each direction). To solve the equations, boundary conditions have to be specified. In this case, periodic b.c. along the transverse direction (y) and open ones along laser propagation direction (x), so that the laser radiation can exit the domain, are adopted. The total time duration of the simulations is set to 350 fs, while the time step has to be determined according to the Courant–Friedrichs–Lewy (CFL) condition, a necessary condition for stability of numerical solutions to the partial differential equations. It reads

$$dt = \frac{CFL}{c\sqrt{\frac{1}{dx^2} + \frac{1}{dy^2}}}, \tag{A.1}$$

where dt, dx and dy are, respectively, the time and the spatial steps, c is the speed of light and CFL the Courant–Friedrichs–Lewy number, assumed to be equal to 0.98. Thus, a time-step of 0.023 fs is obtained.

The laser pulse is made propagate along the x direction, with a P-polarization on the simulation plane (i.e. the electric field oscillates along the y direction). It is initialised as a Gaussian beam both in space and time, with its maximum

at half the box length in the y direction (35 μm). The chosen wavelength is the typical one of Ti:sapphire laser, that is 800 nm, which means a critical density of $n_c = 1.1 \times 10^{21}/\lambda^2 = 1.74 \times 10^{21}$ cm^{-3}. In one set of simulations, all the other laser parameters are set as similar to the SourceLAB Kaio system introduced in Chapter 5, while in a second one the intensity is varied to a much higher value, similar to Apollon one, keeping the other characteristics unchanged. In particular, the temporal duration in terms of full width half maximum (FWHM) is 30 fs and the spatial FWHM is 5 μm at beam waist, that is equal to a spot size of about 20 μm^2. The adimensional vector potential is set to $a_0 = 5$ in one case and to $a_0 = 50$ in the other. The maximum electric field amplitude is, for the wavelength of interest,

$$e_{max} = a_0 \frac{2\pi m_e c^2}{e\lambda} = a_0 \cdot 4 \times 10^{12} \tag{A.2}$$

that gives 2×10^{13} V/m and 2×10^{14} V/m, respectively, that is reached after 50 fs from the beginning of the simulation. Also, recalling the Equation 1.10 and reverting it, the peak intensity can be computed as $I = a_0^2/(0.85\lambda)^2$ (see Table A.1). Lastly, the position of the beam waist has to be decided. It is set to 35 μm, that, as will soon be described, is the position of front side of the titanium film. The laser is focused on the metallic surface of the target. In the case of DLTs, this choice is still valid because the Rayleigh range $z_R = \pi w_0^2/\lambda$, where $w_0 = FWHM/(2\sqrt{\ln 2})$ is the laser waist, is equal to 35 μm: much larger than the foam thickness. This means that the laser can be considered as already focused at the foam edge.

Table A.1. Laser parameters adopted in the numerical computations.

a_0	5	50
λ [μm]	0.8	
I [W/cm^2]	5.4×10^{19}	5.4×10^{21}
e_{max} [V/m]	2×10^{13}	2×10^{14}
Temporal FWHM [fs]	30	
τ [fs]	25.5	
Spatial FWHM [μm]	5	
w_0 [μm]	3	
z_R [μm]	35	
Focus position (x,y) [μm]	35, 35	
n_c [cm^{-3}]	1.74×10^{21}	

On the plasma side, a two or three layers structure is adopted for SLT and DLT, respectively. In both cases, two homogenous slabs, one representing the titanium film and the other a contaminant layer are present. In addition, DLTs present a carbon foam plasma at the front. The characteristics of each of these are here described.

The plasma that represents the titanium film is a homogenous distribution of ions and electrons whose left edge is at $x = 35$ μm and its thickness assumes the values 200, 400, 600, 800, 1200 nm, depending on the simulation. Titanium has atomic number equal to 22 and mass number 48. An important point is to understand if it has to be considered as partially o completely ionized, due to the laser interaction. To assess this, the work by Li et al. [96] has been considered. In particular, in the

supplementary note, the ionization fraction of titanium as a function of the applied electric field is studied (see Figure A.1), although in a constant case. As done in the main article, such results are extended to laser interaction. Thus, what can be concluded is that, at the field strength previously discussed, the most present species is Ti^{20+}. The titanium density has been considered as equal to a representative, average value, given the results presented in section 4.2.2, i.e. 4 g/cm^3. Thus, the electronic density can be computed, giving 1.02×10^{24} cm^{-3} or $588 n_c$ in terms of critical density.

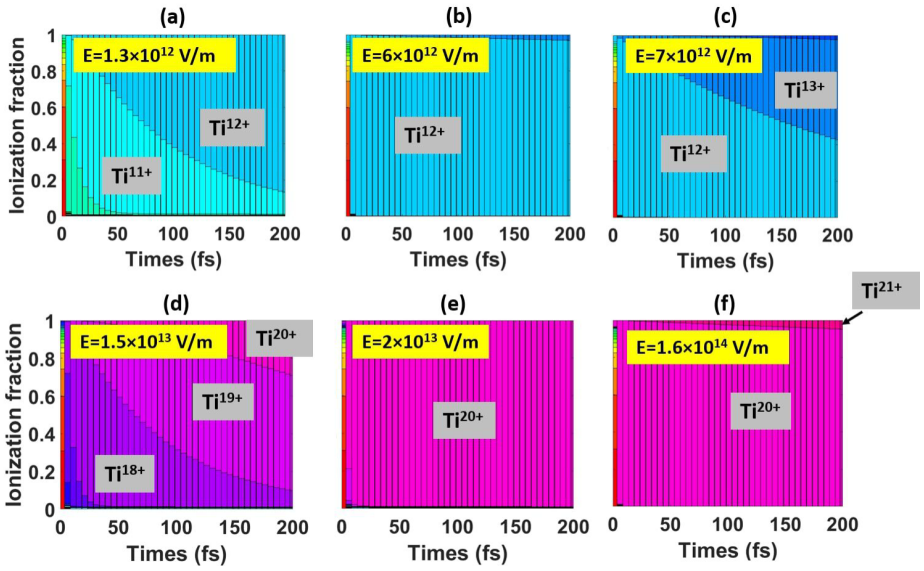

Figure A.1. Calculated ionization fraction as a function of time for a titanium film in a constant applied electric field E of different strength, from [96].

In regards of the foam layer, it is initialized as a homogenous slab of fully ionized carbon atoms ($Z = 6$ and $A = 12$) located at the front of the titanium film. The parameters that describe its thickness and density are chosen, again, in accordance with the results presented in section 4.3.2. In particular, thickness is set equal to 14 µm (that, indeed, is less than z_R, as anticipated) and density to 6.7 mg/cm^3. It corresponds to an electronic density of 2.07×10^{21} cm^{-3}, equivalent to $1.16 n_c$.

Lastly, at the back of each titanium layer, a 50 nm contaminant hydrogen coating (that will be source of accelerated protons) is added, setting its electronic density to the typical, representative value of $10 n_c$.

All the electron species (i.e., coming from the carbon foam, the titanium solid film and the contaminant layer) are initialised according to a Maxwell-Boltzmann distribution with a temperature of 100 eV, while all ions are considered initially cold. No drift velocity is considered at the beginning, as well as no initial electromagnetic fields pertaining to the plasmas are computed solving Poisson equation.

To conclude, the computation performed with a 45° laser incidence angle has been carried out keeping the laser source still and tilting the target. In this way, the only things to be changed are the functions that defines the extent of the plasmas and the boundary conditions: to avoid the re-entering of the reflected laser fields, non-periodic conditions are adopted along both axes.

A summary of the chosen parameters is shown in Table A.2.

Table A.2. Summary of the initial plasma characteristics.

	Foam	Solid metal	Contaminant
A	12	48	1
Ionization $[e^-/atom]$	6	20	1
n_e $[n_c]$	1.16	588	10
thickness [µm]	14	0.2, 0.4, 0.6, 0.8, 1.2	0.05

A.3 Parametric investigation of proton generation

As the laser impinges on the target surface, part of its energy is absorbed by the charged species that form the plasmas. As described in Chapter 1, most of this energy is transferred to the electrons, which have much less inertia than ions. It is only when the sheath is formed at the back of the target and a huge electric field arises that protons can be accelerated in the forward direction. It is thus interesting to consider how the total energy of the system, roughly equivalent to the laser one (the initial thermal energy of electrons, $T_e = 100$ eV, is negligible), is distributed among the species at different simulated times.

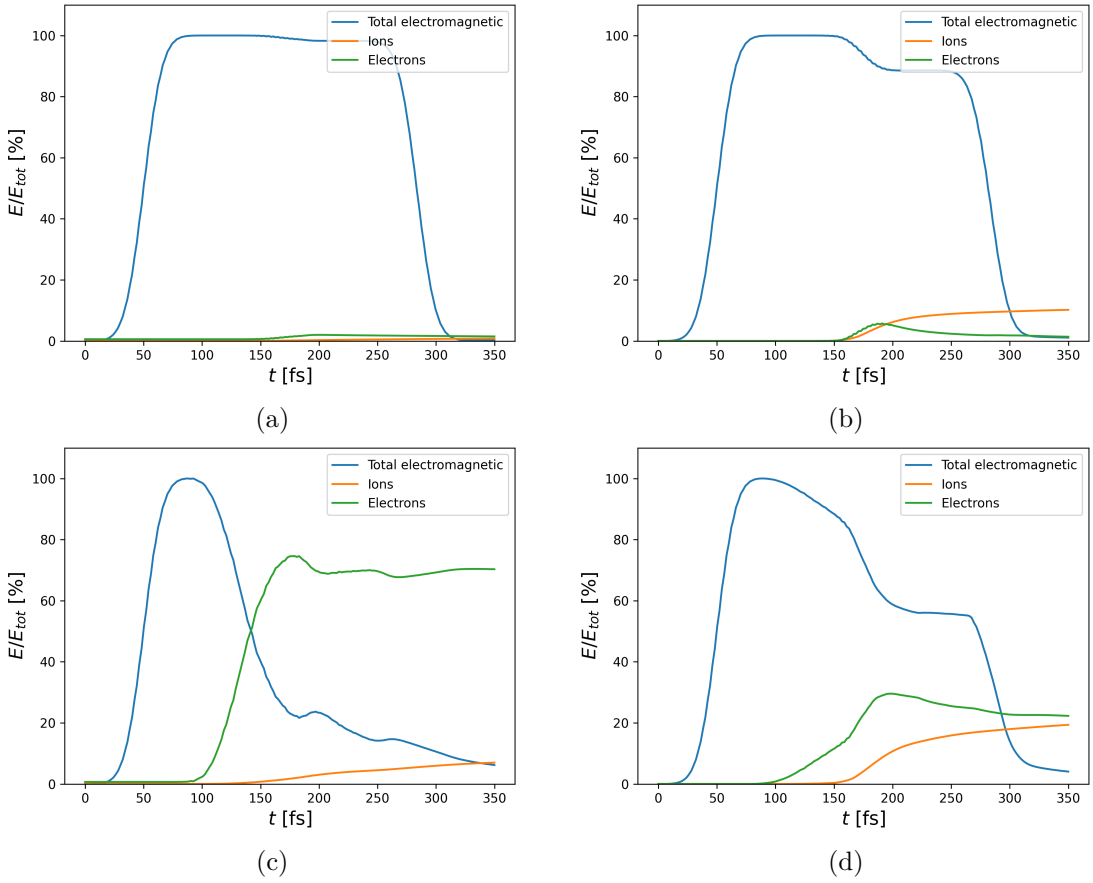

Figure A.2. Energy distribution between electrons, ions and electromagnetic fields relative to total laser energy as a function of time. In particular, four cases are presented: (a) SLT, 0.2 µm thick and $a_0 = 5$; (b) SLT, 0.2 µm thick and $a_0 = 50$; (c) DLT with 0.2 µm titanium and $a_0 = 5$; (d) DLT with 0.2 µm titanium and $a_0 = 50$.

The results are shown in Figure A.2, where the percentage of laser energy transformed in kinetic energy of all electrons (green line) and all ions (orange line), along with the energy stored in the electromagnetic fields (blue line), is depicted as function of time. Since the effect of the metallic film thickness is not, at least qualitatively, of particular effect on such quantities, only the plots characterized by a 0.2 µm titanium layer are presented, both in DLT and SLT configurations. On the other hand, the different intensities that are considered have a strong effect on the energy distribution. In the case of SLTs at low intensity ($a_0 = 5$), only a very low amount of energy is transferred to the charged particles and the laser leaves the box with little energetic variation, as the hat shape of the blue curve suggests (Figure A.2 (a)). When the near critical layer is added (Figure A.2 (c)), instead, a significant improvement in the conversion is observed, as the total kinetic energy of ions reaches some percent at the end of the computation. In the high intensity case, i.e. $a_0 = 50$, the situation is different. In this case, the single film target (Figure A.2 (b)) is able to convert laser energy into ions' one at a relative value similar to the previously described one for the DLT, but with less (relative) energy transferred to electrons. Lastly, in Figure A.2 (d) the behaviour of the double layer at high intensity can be seen: much more energy is transferred to ions, as a value around 20 % is reached, that is more than double that the one in the lower a_0 scenario.

To visualize what happens to the targets under laser irradiation, a plot that superimposes the electronic density of the plasmas and the magnetic field orthogonal to the laser polarization direction, i.e. along z, can be helpful (Figure A.3). Three time-steps are shown for each relevant configuration: as before, there is no qualitative difference in double layer targets due to the titanium thickness, while it is not the case for the simple foils. So, for SLT, the two limiting thickness cases are both shown, i.e. 0.2 µm and 1.2 µm. Starting from these last ones, it can be observed that

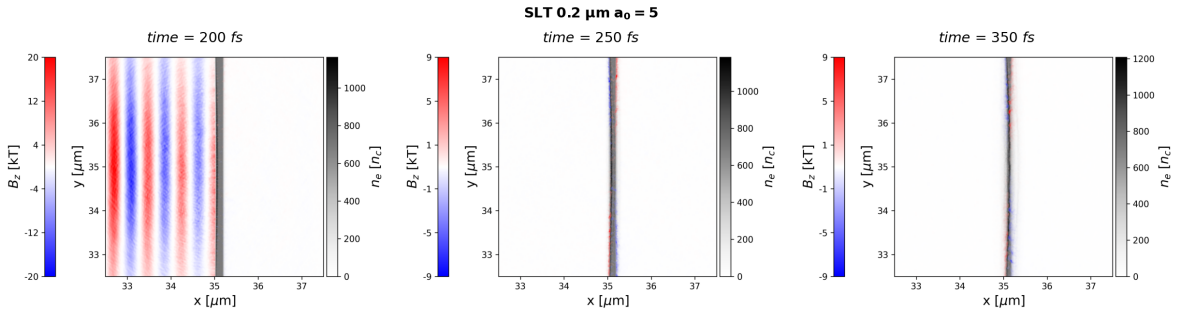

(a)

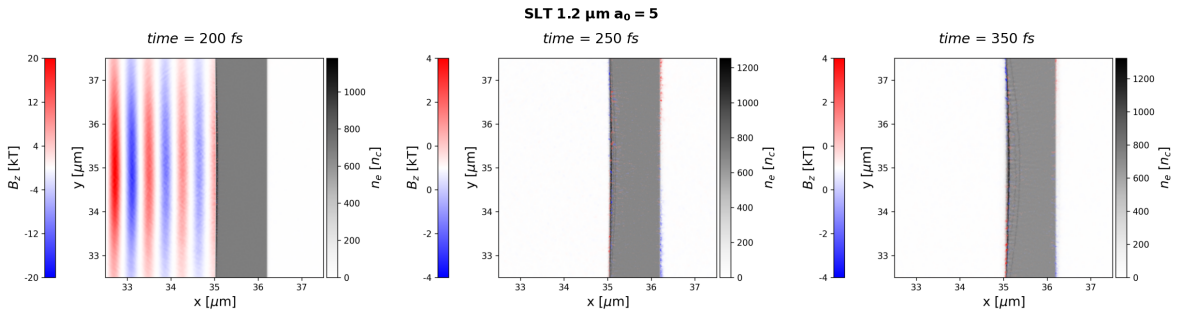

(b)

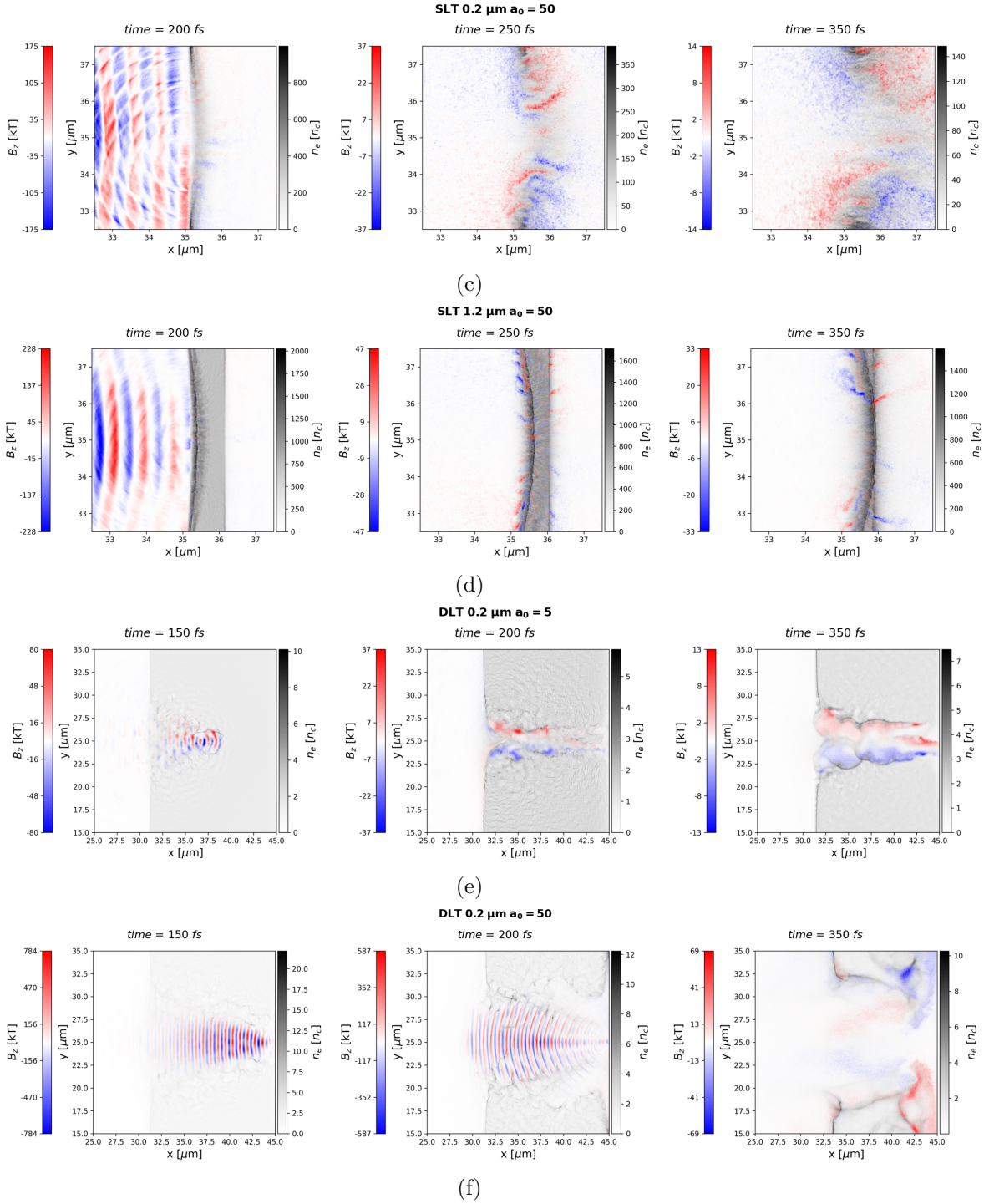

Figure A.3. Superimposed colormaps for z-component of the magnetic field B_z and the electronic density n_e at three time-steps for different scenarios: (a) SLT, 0.2 μm thick and $a_0 = 5$; (b) SLT, 1.2 μm thick and $a_0 = 5$; (c) SLT, 0.2 μm thick and $a_0 = 50$; (d) SLT, 1.2 μm thick and $a_0 = 50$; (e) DLT with 0.2 μm titanium and $a_0 = 5$; (f) DLT with 0.2 μm titanium and $a_0 = 50$.

at low intensity both the two targets are still confined in space at the end of the computation. In particular, while the thin film is visibly ablated (Figure A.3 (a)) and

thus appears thinner, the thick one seems just slightly perturbed (Figure A.3 (b)). On the other hand, when the more powerful pulse impinges on them, they are both disintegrated and the particles are dispersed in space (Figure A.3 (c,d)). When the interaction occurs with a near critical plasma instead of an overdense one, something very different happens. Indeed, the *self-focusing effect* is clearly visible at the first time-step and the formation of a magnetization channel follows (Figure A.3 (e,f)). As for the intensity effect, while with lower values the foam layer is perforated only locally (Figure A.3 (e)), at the end of the simulation, at high values the target is once again completely wiped out (Figure A.3 (f)).

After these general considerations, the characteristics of the accelerated protons from the contaminant layer can be discussed. The energy spectra, normalized to the total number of protons, are computed at the last time-step, i.e. 350 fs. At previous times, the functional shape is quite the same, but the endpoint is lower, as in 2D simulations no saturation occurs. That means also that the results have to be considered for a comparison rather then absolute, although an empirical law has been proposed to overcome this limitation [97, 98].

In Figure A.4, the results in the $a_0 = 5$ set, for both the target types and all the investigated thicknesses, are presented. In the case of DLTs, no significant effect, except for a slightly increasing endpoint energy with decreasing thickness, is observed. This suggests that the dominant role is played by the low density layer, which is the main responsible for hot electron production that leads the TNSA process. A different situation, as expected, is seen in the case of the single metallic film. Here, in all cases the achieved energies are much lower and the number of protons accelerated at higher energies decreases much faster with increasing energy. Though, the thickness has a strong influence, as a significant reduction both in energy and accelerated species is observed. In particular, the decrease is stronger passing from 0.2 µm to 0.4 µm, while above 0.6 µm it is less pronounced, as can be seen in Figure A.4 (b).

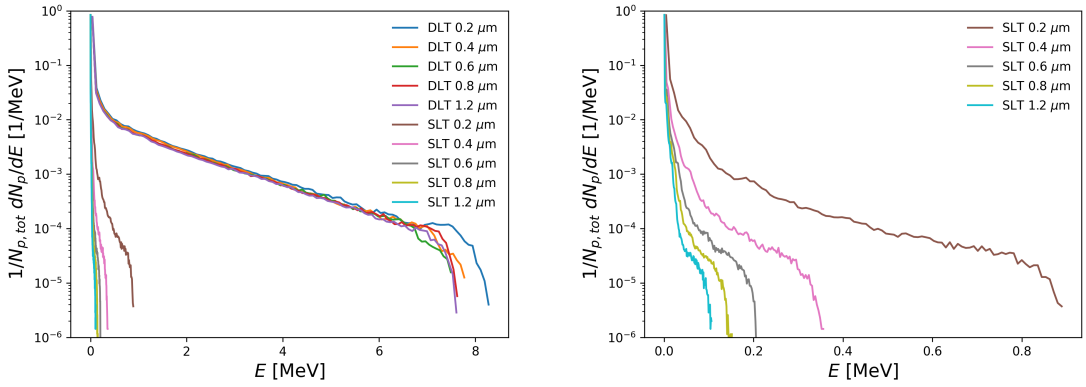

(a) (b)

Figure A.4. Normalized proton spectra from all the investigated targets for $a_0 = 5$ (a). In (b), a close-up presenting only the results from single layer targets.

When the intensity is increased to $a_0 = 50$ (Figure A.5), less difference is observed between the two target configurations, while the considerations made on the effect of the metallic film thickness remain substantially valid.

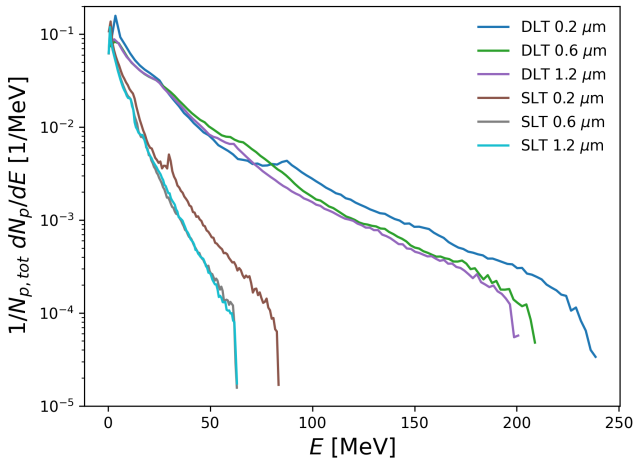

Figure A.5. Normalized proton spectra from all the investigated targets for $a_0 = 50$.

To better compare the results in terms of proton energies, a plot of the recorded maximum energies is shown in Figure A.6 for both values of normalized vector potential. The endpoint decreases with the thickness for both target designs, steeper at low values than high ones (in particular, above 0.6 μm).

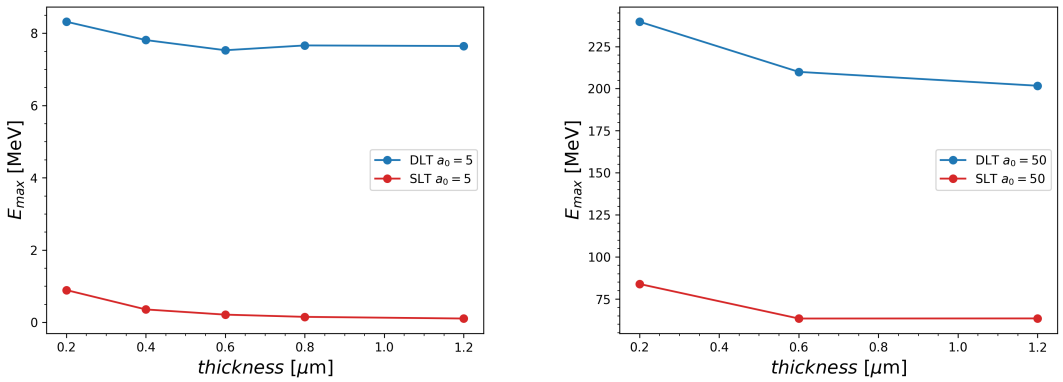

(a) (b)

Figure A.6. Maximum proton energies for all the performed simulations.

Moreover, it is possible to fit all of the spectra to a simple decaying exponential $e^{-E/T}$ (the plots are semi-logarithmic) by cutting the edges. Thus, the proton temperature can be retrieved. Results are presented in Figure A.7 and the general trend is analogous the maximum energy one. Nevertheless, for $a_0 = 5$ a slight increase is observed for 0.6 μm and 0.8 μm but it is a small variation that can be probably caused by the choice of the fit interval.

Another interesting consideration that can be made is related to the angular distribution of the accelerated protons. A double differential, energy and angle, spectrum (Figure A.8) shows one of the characteristics of TNSA, that is the directionality. Indeed, the emitted particles are directed in the forward direction, with little angular deviations. Anyway, in the higher laser intensity case the angular spread is greater,

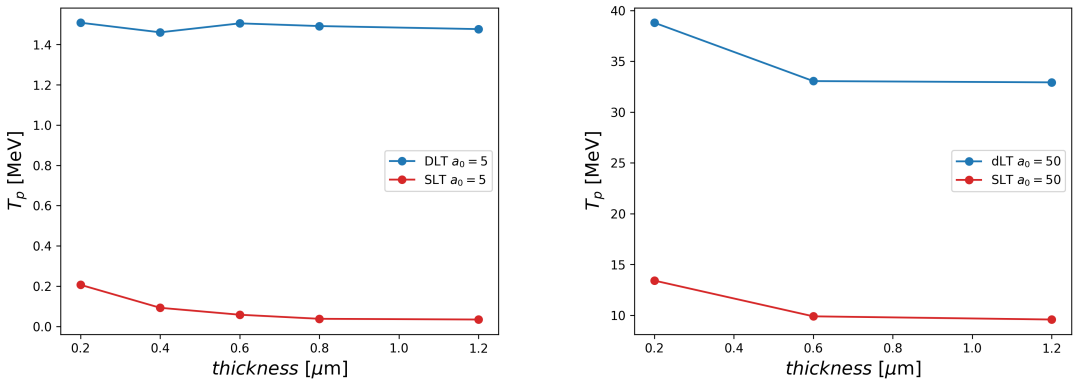

(a) (b)

Figure A.7. Estimated proton temperatures for all the performed simulations.

while no particular differences are observed as a function of the thickness, at least for DLTs. In fact, the SLTs seem to show an even greater collimation at higher thicknesses, although the variation is quite little.

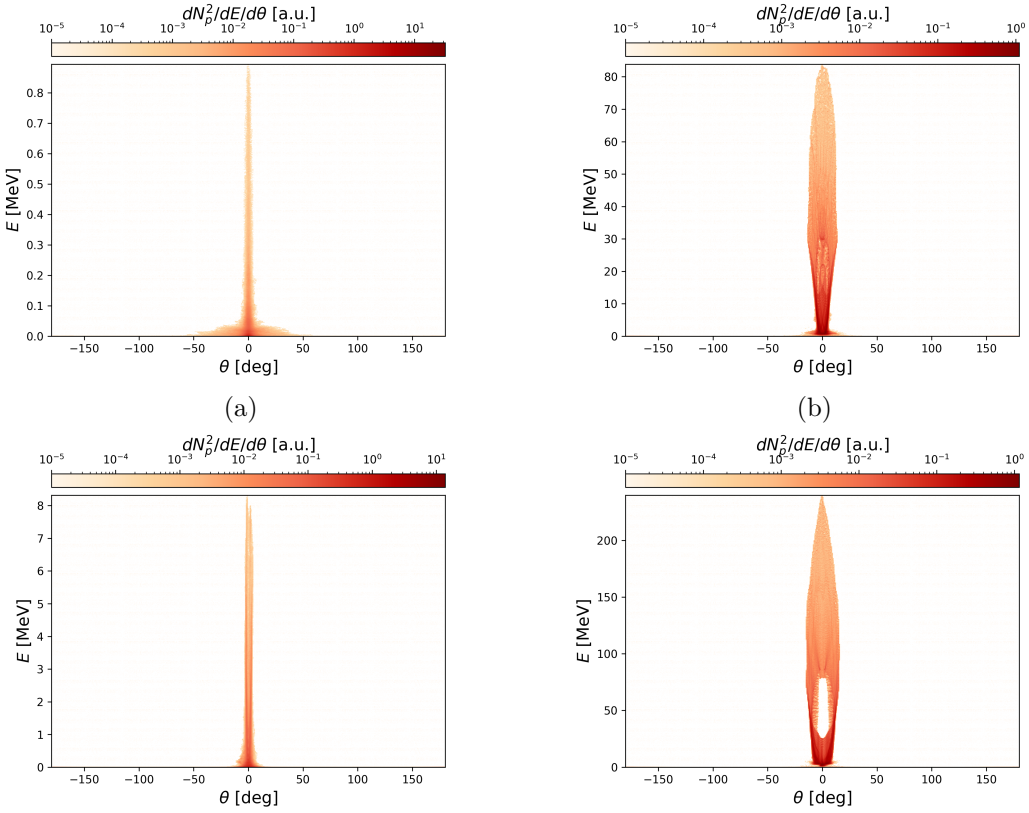

(a) (b)

(c) (d)

Figure A.8. Angular and energetic proton spectra. In particular: (a) SLT, 0.2 μm thick and $a_0 = 5$; (b) SLT, 0.2 μm thick and $a_0 = 50$; (c) DLT with 0.2 μm titanium and $a_0 = 5$; (d) DLT with 0.2 μm titanium and $a_0 = 50$.

As anticipated, the effect of laser incidence angle in the SLT configuration is also

investigated. In particular, a numerical computation for a 0.2 µm titanium film at $a_0 = 5$ has been performed. At oblique incidence, additional heating mechanisms should kick in, leading to enhancement of hot electron generation and thus in proton acceleration [99, 100]. In fact, referring to Figure A.9 (a), a higher coupling between the laser and the plasma is observed, as higher energy is transferred to the charged species. In turn, this results in a much higher number of protons accelerated at high energies, whose spectrum presents a maximum energy about five time greater than at normal incidence, as can be seen in Figure A.9 (b).

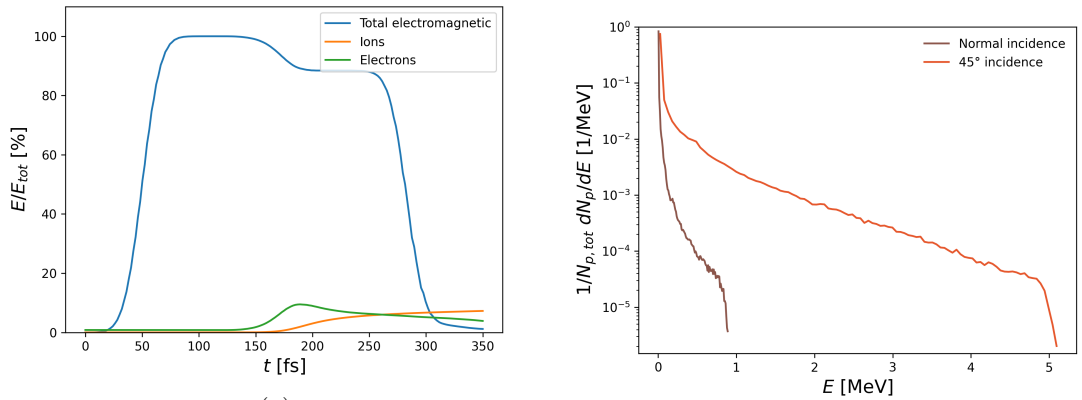

(a) (b)

Figure A.9. Investigation of the effect of laser incidence angle on 0.2 µm SLTs at $a_0 = 5$ in terms of (a) energy distribution among the species at 45° incidence and (b) comparison of proton spectra.

To summarize, the expected features of particles from target normal sheath acceleration are observed, like the narrow spread in the forward direction. The near critical layer is effective in improving the number and energy of the protons and the effect of the underlying solid film thickness is scarcely influential. On the other hand, the simple metallic films produce particles whose characteristics have a strong dependence on the thickness, with a quite quick decrease in maximum energy as it is increased. Anyway, at high intensity this effect is reduced. To improve the proton production by single layer targets, the laser incidence angle can be varied: in fact, a strong enhancement in terms of energy and particle number can be obtained, despite being still lower than in the DLT configuration. Considering the same laser system, the DLTs allow for higher maximum proton energies, greater proton temperatures and thus average energies, greater number of particles accelerated at high energies and good performance stability with respect to the metal layer thickness.

Bibliography

[1] O. Svelto, *Principles of Lasers*. Springer US, 2010.

[2] D. Strickland and G. Mourou, "Compression of amplified chirped optical pulses," *Optics Communications*, vol. 56, pp. 219–221, 12 1985.

[3] G. Mourou, "Nobel lecture: Extreme light physics and application," *Reviews of Modern Physics*, vol. 91, 7 2019.

[4] M. Zavelani-Rossi and F. Vismarra, *High intensity lasers for nuclear and physical applications*. Società Editrice Esculapio, 2020.

[5] S. Witte and K. S. E. Eikema, "Ultrafast optical parametric chirped-pulse amplification," *IEEE Journal of Selected Topics in Quantum Electronics*, vol. 18, 1 2012.

[6] Y. Chu, X. Liang, L. Yu, Y. Xu, L. Xu, L. Ma, X. Lu, Y. Liu, Y. Leng, R. Li, and Z. Xu, "High-contrast 20 petawatt ti:sapphire laser system," *Optics Express*, vol. 21, 12 2013.

[7] A. Macchi, *A Superintense Laser-Plasma Interaction Theory Primer*. Springer Netherlands, 2013.

[8] P. Mulser and D. Bauer, *High Power Laser-Matter Interaction*. Springer Berlin Heidelberg, 2010, vol. 238.

[9] F. Grüner, "Shooting ahead with wakefield acceleration," *Physics*, vol. 12, 2 2019.

[10] L. Fedeli, A. Formenti, L. Cialfi, A. Pazzaglia, and M. Passoni, "Ultra-intense laser interaction with nanostructured near-critical plasmas," *Scientific Reports*, vol. 8, 12 2018.

[11] W. I. Linlor, "Ion energies produced by laser giant pulse," *Applied Physics Letters*, vol. 3, 12 1963.

[12] S. J. Gitomer, R. D. Jones, F. Begay, A. W. Ehler, J. F. Kephart, and R. Kristal, "Fast ions and hot electrons in the laser–plasma interaction," *Physics of Fluids*, vol. 29, 1986.

[13] E. L. Clark, K. Krushelnick, J. R. Davies, M. Zepf, M. Tatarakis, F. N. Beg, A. Machacek, P. A. Norreys, M. I. K. Santala, I. Watts, and A. E. Dangor,

"Measurements of energetic proton transport through magnetized plasma from intense laser interactions with solids," *Physical Review Letters*, vol. 84, 1 2000.

[14] A. Maksimchuk, S. Gu, K. Flippo, D. Umstadter, and V. Y. Bychenkov, "Forward ion acceleration in thin films driven by a high-intensity laser," *Physical Review Letters*, vol. 84, 5 2000.

[15] R. A. Snavely, M. H. Key, S. P. Hatchett, T. E. Cowan, M. Roth, T. W. Phillips, M. A. Stoyer, E. A. Henry, T. C. Sangster, M. S. Singh, S. C. Wilks, A. MacKinnon, A. Offenberger, D. M. Pennington, K. Yasuike, A. B. Langdon, B. F. Lasinski, J. Johnson, M. D. Perry, and E. M. Campbell, "Intense high-energy proton beams from petawatt-laser irradiation of solids," *Physical Review Letters*, vol. 85, 10 2000.

[16] H. Daido, M. Nishiuchi, and A. S. Pirozhkov, "Review of laser-driven ion sources and their applications," *Reports on Progress in Physics*, vol. 75, 5 2012.

[17] S. C. Wilks, A. B. Langdon, T. E. Cowan, M. Roth, M. Singh, S. Hatchett, M. H. Key, D. Pennington, A. MacKinnon, and R. A. Snavely, "Energetic proton generation in ultra-intense laser–solid interactions," *Physics of Plasmas*, vol. 8, 2 2001.

[18] H. Schwoerer, S. Pfotenhauer, O. Jäckel, K.-U. Amthor, B. Liesfeld, W. Ziegler, R. Sauerbrey, K. W. D. Ledingham, and T. Esirkepov, "Laser-plasma acceleration of quasi-monoenergetic protons from microstructured targets," *Nature*, vol. 439, 1 2006.

[19] B. M. Hegelich, B. Albright, P. Audebert, A. Blazevic, E. Brambrink, J. Cobble, T. Cowan, J. Fuchs, J. C. Gauthier, C. Gautier, M. Geissel, D. Habs, R. Johnson, S. Karsch, A. Kemp, S. Letzring, M. Roth, U. Schramm, J. Schreiber, K. J. Witte, and J. C. Fernández, "Spectral properties of laser-accelerated mid-z mev u ion beams," *Physics of Plasmas*, vol. 12, 5 2005.

[20] A. Macchi, M. Borghesi, and M. Passoni, "Ion acceleration by superintense laser-plasma interaction," *Reviews of Modern Physics*, vol. 85, 5 2013.

[21] M. Roth and M. Schollmeier, "Ion acceleration-target normal sheath acceleration *," *CERN Yellow Report*, pp. 231–270, 2016. [Online]. Available: http://dx.doi.org/10.5170/CERN-2016-001.231

[22] M. Borghesi, J. Fuchs, S. V. Bulanov, A. J. MacKinnon, P. K. Patel, and M. Roth, "Fast ion generation by high-intensity laser irradiation of solid targets and applications," *Fusion Science and Technology*, vol. 49, 4 2006.

[23] P. McKenna, K. W. D. Ledingham, S. Shimizu, J. M. Yang, L. Robson, T. McCanny, J. Galy, J. Magill, R. J. Clarke, D. Neely, P. A. Norreys, R. P. Singhal, K. Krushelnick, and M. S. Wei, "Broad energy spectrum of laser-accelerated protons for spallation-related physics," *Physical Review Letters*, vol. 94, 3 2005.

[24] V. Y. Bychenkov, Y. Sentoku, S. V. Bulanov, K. Mima, G. Mourou, and S. V. Tolokonnikov, "Pion production under the action of intense ultrashort laser pulse on a solid target," *Journal of Experimental and Theoretical Physics Letters*, vol. 74, 12 2001.

[25] M. Passoni, L. Fedeli, and F. Mirani, "Superintense laser-driven ion beam analysis," *Scientific Reports*, vol. 9, 12 2019.

[26] F. Mirani, A. Maffini, F. Casamichiela, A. Pazzaglia, A. Formenti, D. Dellasega, V. Russo, D. Vavassori, D. Bortot, M. Huault, G. Zeraouli, V. Ospina, S. Malko, J. I. Apiñaniz, J. A. Pérez-Hernández, D. D. Luis, G. Gatti, L. Volpe, A. Pola, and M. Passoni, "Integrated quantitative pixe analysis and edx spectroscopy using a laser-driven particle source," 2021. [Online]. Available: http://advances.sciencemag.org/

[27] J. J. Honrubia, J. C. Fernández, M. Temporal, B. M. Hegelich, and J. M. ter Vehn, "Fast ignition of inertial fusion targets by laser-driven carbon beams," *Physics of Plasmas*, vol. 16, 10 2009.

[28] K. Ogura, T. Shizuma, T. Hayakawa, A. Yogo, M. Nishiuchi, S. Orimo, A. Sagisaka, A. Pirozhkov, M. Mori, H. Kiriyama, S. Kanazawa, S. Kondo, Y. Nakai, T. Shimoura, M. Tanoue, A. Akutsu, T. Motomura, H. Okada, T. Kimura, Y. Oishi, T. Nayuki, T. Fujii, K. Nemoto, and H. Daido, "Proton-induced nuclear reactions using compact high-contrast high-intensity laser," *Applied Physics Express*, vol. 2, 5 2009.

[29] F. P. Boody, R. Höpfl, H. Hora, and J. C. Kelly, "Laser-driven ion source for reduced-cost implantation of metal ions for strong reduction of dry friction and increased durability," *Laser and Particle Beams*, vol. 14, 9 1996.

[30] C. Palmer, "Paving the way for a revolution in high repetition rate laser-driven ion acceleration," *New Journal of Physics*, vol. 20, 6 2018.

[31] I. Prencipe, J. Fuchs, S. Pascarelli, D. W. Schumacher, R. B. Stephens, N. B. Alexander, R. Briggs, M. Büscher, M. O. Cernaianu, A. Choukourov, M. D. Marco, A. Erbe, J. Fassbender, G. Fiquet, P. Fitzsimmons, C. Gheorghiu, J. Hund, L. G. Huang, M. Harmand, N. J. Hartley, A. Irman, T. Kluge, Z. Konopkova, S. Kraft, D. Kraus, V. Leca, D. Margarone, J. Metzkes, K. Nagai, W. Nazarov, P. Lutoslawski, D. Papp, M. Passoni, A. Pelka, J. P. Perin, J. Schulz, M. Smid, C. Spindloe, S. Steinke, R. Torchio, C. Vass, T. Wiste, R. Zaffino, K. Zeil, T. Tschentscher, U. Schramm, and T. E. Cowan, "Targets for high repetition rate laser facilities: needs, challenges and perspectives," *High Power Laser Science and Engineering*, vol. 5, 7 2017.

[32] K. T. Phuoc, F. Burgy, J.-P. Rousseau, V. Malka, A. Rousse, R. Shah, D. Umstadter, A. Pukhov, and S. Kiselev, "Laser based synchrotron radiation," *Physics of Plasmas*, vol. 12, 2 2005.

[33] K. Krushelnick and V. Malka, "Laser wakefield plasma accelerators," *Laser & Photonics Reviews*, vol. 4, 1 2010.

[34] F. Sylla, M. Veltcheva, S. Kahaly, A. Flacco, and V. Malka, "Development and characterization of very dense submillimetric gas jets for laser-plasma interaction," *Review of Scientific Instruments*, vol. 83, 3 2012.

[35] "Sourcelab sl-alc motorized gas cell for electron injection." [Online]. Available: https://www.sourcelab-plasma.com/targetry-catalog/motorized-gas-cell/

[36] T. Ceccotti, A. Lévy, H. Popescu, F. Réau, P. D'Oliveira, P. Monot, J. P. Geindre, E. Lefebvre, and P. Martin, "Proton acceleration with high-intensity ultrahigh-contrast laser pulses," *Physical Review Letters*, vol. 99, 10 2007.

[37] M. N. ul Haq, H. Ahmed, T. Sokollik, L. Yu, Z. Liu, X. Yuan, F. Yuan, M. Mirzaie, X. Ge, L. Chen, and J. Zhang, "Statistical analysis of laser driven protons using a high-repetition-rate tape drive target system," *Physical Review Accelerators and Beams*, vol. 20, 4 2017.

[38] J. T. Morrison, S. Feister, K. D. Frische, D. R. Austin, G. K. Ngirmang, N. R. Murphy, C. Orban, E. A. Chowdhury, and W. M. Roquemore, "Mev proton acceleration at khz repetition rate from ultra-intense laser liquid interaction," *New Journal of Physics*, vol. 20, 2 2018.

[39] P. L. Poole, C. Willis, G. E. Cochran, R. T. Hanna, C. D. Andereck, and D. W. Schumacher, "Moderate repetition rate ultra-intense laser targets and optics using variable thickness liquid crystal films," *Applied Physics Letters*, vol. 109, 10 2016.

[40] K. Nagai, C. S. A. Musgrave, and W. Nazarov, "A review of low density porous materials used in laser plasma experiments," *Physics of Plasmas*, vol. 25, 3 2018.

[41] S. Buffechoux, J. Psikal, M. Nakatsutsumi, L. Romagnani, A. Andreev, K. Zeil, M. Amin, P. Antici, T. Burris-Mog, A. Compant-La-Fontaine, E. d'Humières, S. Fourmaux, S. Gaillard, F. Gobet, F. Hannachi, S. Kraft, A. Mancic, C. Plaisir, G. Sarri, M. Tarisien, T. Toncian, U. Schramm, M. Tampo, P. Audebert, O. Willi, T. E. Cowan, H. Pépin, V. Tikhonchuk, M. Borghesi, and J. Fuchs, "Hot electrons transverse refluxing in ultraintense laser-solid interactions," *Physical Review Letters*, vol. 105, 7 2010.

[42] S. Kar, K. Markey, M. Borghesi, D. C. Carroll, P. McKenna, D. Neely, M. N. Quinn, and M. Zepf, "Ballistic focusing of polyenergetic protons driven by petawatt laser pulses," *Physical Review Letters*, vol. 106, 6 2011.

[43] J. Krása, D. Klír, A. Velyhan, D. Margarone, E. Krouský, K. Jungwirth, J. Skála, M. Pfeifer, J. Kravárik, P. Kubeš, K. Řezáč, and J. Ullschmied, "Observation of repetitive bursts in emission of fast ions and neutrons in sub-nanosecond laser-solid experiments," *Laser and Particle Beams*, vol. 31, 9 2013.

[44] S. Vallières, M. Salvadori, A. Permogorov, G. Cantono, K. Svendsen, Z. Chen, S. Sun, F. Consoli, E. d'Humières, C.-G. Wahlström, and P. Antici, "Enhanced laser-driven proton acceleration using nanowire targets," *Scientific Reports*, vol. 11, 12 2021.

[45] M. Passoni, A. Sgattoni, I. Prencipe, L. Fedeli, D. Dellasega, L. Cialfi, I. W. Choi, I. J. Kim, K. Janulewicz, H. W. Lee, J. H. Sung, S. K. Lee, and C. H. Nam, "Toward high-energy laser-driven ion beams: Nanostructured double-layer targets," *Physical Review Accelerators and Beams*, vol. 19, 6 2016.

[46] I. Prencipe, A. Sgattoni, D. Dellasega, L. Fedeli, L. Cialfi, I. W. Choi, I. J. Kim, K. A. Janulewicz, K. F. Kakolee, H. W. Lee, J. H. Sung, S. K. Lee, C. H. Nam, and M. Passoni, "Development of foam-based layered targets for laser-driven ion beam production," *Plasma Physics and Controlled Fusion*, vol. 58, 3 2016.

[47] L. Fedeli, A. Formenti, C. E. Bottani, and M. Passoni, "Parametric investigation of laser interaction with uniform and nanostructured near-critical plasmas," *Eur. Phys. J. D*, vol. 71, p. 202, 2017.

[48] M. Passoni, F. M. Arioli, L. Cialfi, D. Dellasega, L. Fedeli, A. Formenti, A. C. Giovannelli, A. Maffini, F. Mirani, A. Pazzaglia, A. Tentori, D. Vavassori, M. Zavelani-Rossi, and V. Russo, "Advanced laser-driven ion sources and their applications in materials and nuclear science," *Plasma Physics and Controlled Fusion*, vol. 62, 1 2020.

[49] A. Pazzaglia, L. Fedeli, A. Formenti, A. Maffini, and M. Passoni, "A theoretical model of laser-driven ion acceleration from near-critical double-layer targets," *Communications Physics*, vol. 3, 12 2020.

[50] M. Barberio, M. Scisciò, S. Veltri, and P. Antici, "Fabrication of nanostructured targets for improved laser-driven proton acceleration," *Superlattices and Microstructures*, vol. 95, 7 2016.

[51] C. Spindloe, G. Arthur, F. Hall, S. Tomlinson, R. Potter, S. Kar, J. Green, A. Higginbotham, N. Booth, and M. K. Tolley, "High volume fabrication of laser targets using mems techniques," *Journal of Physics: Conference Series*, vol. 713, 4 2016.

[52] R. Zaffino, M. Seimetz, D. Quirión, A. R. de la Cruz, I. Sánchez, P. Mur, J. Benlliure, L. Martín, L. Roso, J. M. Benlloch, M. Lozano, and G. Pellegrini, "Preparation and characterization of micro-nano engineered targets for high-power laser experiments," *Microelectronic Engineering*, vol. 194, 7 2018.

[53] Y. Miyamoto, Y. Fujii, M. Yamano, T. Harigai, Y. Suda, H. Takikawa, T. Kawano, M. Nishiuchi, H. Sakaki, and K. Kondo, "Preparation of self-supporting au thin films on perforated substrate by releasing from water-soluble sacrificial layer," *Japanese Journal of Applied Physics*, vol. 55, 7 2016.

[54] D. Vavassori, "Production of optimized targets for enhanced laser-driven ion acceleration," 2019. [Online]. Available: http://hdl.handle.net/10589/148398

[55] A. Maffini, A. Pazzaglia, D. Dellasega, V. Russo, and M. Passoni, "Growth dynamics of pulsed laser deposited nanofoams," *Physical Review Materials*, vol. 3, 8 2019.

[56] M. Ohring, *Materials Science of Thin Films*. Elsevier, 2002.

[57] P. Sigmund, "Theory of sputtering. i. sputtering yield of amorphous and polycrystalline targets," *Physical Review*, vol. 184, 8 1969.

[58] Y. YAMAMURA and H. TAWARA, "Energy dependence of ion-induced sputtering yields from monatomic solids at normal incidence," *Atomic Data and Nuclear Data Tables*, vol. 62, 3 1996.

[59] P. J. Kelly and R. D. Arnell, "Magnetron sputtering: a review of recent developments and applications," *Vacuum*, vol. 56, pp. 159–172, 3 2000.

[60] N. Savvides and B. Window, "Unbalanced magnetron ion-assisted deposition and property modification of thin films," *Journal of Vacuum Science & Technology A: Vacuum, Surfaces, and Films*, vol. 4, 5 1986.

[61] K. Sarakinos, J. Alami, and S. Konstantinidis, "High power pulsed magnetron sputtering: A review on scientific and engineering state of the art," *Surface and Coatings Technology*, vol. 204, 2 2010.

[62] C. Christou and Z. H. Barber, "Ionization of sputtered material in a planar magnetron discharge," *Journal of Vacuum Science & Technology A: Vacuum, Surfaces, and Films*, vol. 18, 11 2000.

[63] J. A. Thornton, "Magnetron sputtering: basic physics and application to cylindrical magnetrons," *Journal of Vacuum Science and Technology*, vol. 15, 3 1978.

[64] E. A. Ellis, M. Chmielus, S. Han, and S. P. Baker, "Effect of sputter pressure on microstructure and properties of β-ta thin films," *Acta Materialia*, vol. 183, 1 2020.

[65] J. A. Thornton, "Influence of apparatus geometry and deposition conditions on the structure and topography of thick sputtered coatings," *Journal of Vacuum Science and Technology*, vol. 11, 7 1974.

[66] A. Anders, "A structure zone diagram including plasma based deposition and ion etching," 2010.

[67] A. D. Bonis and R. Teghil, "Ultra-short pulsed laser deposition of oxides, borides and carbides of transition elements," *Coatings*, vol. 10, 5 2020.

[68] B. Verhoff, S. S. Harilal, J. R. Freeman, P. K. Diwakar, and A. Hassanein, "Dynamics of femto- and nanosecond laser ablation plumes investigated using optical emission spectroscopy," *Journal of Applied Physics*, vol. 112, 11 2012.

[69] J. Perrière, C. Boulmer-Leborgne, R. Benzerga, and S. Tricot, "Nanoparticle formation by femtosecond laser ablation," *Journal of Physics D: Applied Physics*, vol. 40, 11 2007.

[70] A. Zani, D. Dellasega, V. Russo, and M. Passoni, "Ultra-low density carbon foams produced by pulsed laser deposition," *Carbon*, vol. 56, 5 2013.

[71] "Ensure erc project." [Online]. Available: https://www.ensure.polimi.it/

[72] A. Pazzaglia, A. Maffini, D. Dellasega, A. Lamperti, and M. Passoni, "Reference-free evaluation of thin films mass thickness and composition through energy dispersive x-ray spectroscopy," *Materials Characterization*, vol. 153, 7 2019.

[73] G. Abadias, E. Chason, J. Keckes, M. Sebastiani, G. B. Thompson, E. Barthel, G. L. Doll, C. E. Murray, C. H. Stoessel, and L. Martinu, "Review article: Stress in thin films and coatings: Current status, challenges, and prospects," *Journal of Vacuum Science & Technology A: Vacuum, Surfaces, and Films*, vol. 36, 3 2018.

[74] "Scanning electron microscope, wikipedia." [Online]. Available: https://en.wikipedia.org/wiki/Scanning_electron_microscope

[75] D. Brandon and W. Kaplan, "Scanning electron microscopy," pp. 261–331, 2008.

[76] W. E. Sweeney, R. E. Seebold, and L. S. Birks, "Electron probe measurements of evaporated metal films," *Journal of Applied Physics*, vol. 31, 6 1960.

[77] G. G. Stoney, "The tension of metallic films deposited by electrolysis," *Proceedings of the Royal Society of London. Series A, Containing Papers of a Mathematical and Physical Character*, vol. 82, 5 1909.

[78] E. Besozzi, "Thermomechanical characterization of fusion-relevant nanostructured coatings," 2018.

[79] D. Orecchia, "Femtosecond pulsed laser deposition of carbon nanofoams for laser-driven ion acceleration," 2020. [Online]. Available: http://hdl.handle.net/10589/164958

[80] D. Dellasega, F. Mirani, D. Vavassori, C. Conti, and M. Passoni, "Role of energetic ions in the growth of fcc and ω crystalline phases in ti films deposited by hipims," *Applied Surface Science*, vol. 556, p. 149678, 8 2021.

[81] A. Pazzaglia, A. Maffini, D. Orecchia, M. Zavelani-Rossi, and M. Passoni, "Fractal carbon nanofoams by nanosecond and femtosecond pulsed-laser deposition," 2020.

[82] P. M. Barker, S. Konstantinidis, E. Lewin, N. Britun, and J. Patscheider, "An investigation of c-hipims discharges during titanium deposition," *Surface and Coatings Technology*, vol. 258, 11 2014.

[83] I. Prencipe, D. Dellasega, A. Zani, D. Rizzo, and M. Passoni, "Energy dispersive x-ray spectroscopy for nanostructured thin film density evaluation," *Science and Technology of Advanced Materials*, vol. 16, 4 2015.

[84] J. Chakraborty, K. Kumar, R. Ranjan, S. G. Chowdhury, and S. Singh, "Thickness-dependent fcc–hcp phase transformation in polycrystalline titanium thin films," *Acta Materialia*, vol. 59, 4 2011.

[85] "Sourcelab kaio plug & play ion generator." [Online]. Available: https://www.sourcelab-plasma.com/solutions/particle-sources/particle-sources-catalog/ion-generator/

[86] J. M. Dawson, "Particle simulation of plasmas," *Reviews of Modern Physics*, vol. 55, 4 1983.

[87] T. D. Arber, K. Bennett, C. S. Brady, A. Lawrence-Douglas, M. G. Ramsay, N. J. Sircombe, P. Gillies, R. G. Evans, H. Schmitz, A. R. Bell, and C. P. Ridgers, "Contemporary particle-in-cell approach to laser-plasma modelling," *Plasma Physics and Controlled Fusion*, vol. 57, 11 2015.

[88] J. P. Boris, "Relativistic plasma simulation-optimization of a hybrid code," N. R. Laboratory, Ed., 1970, pp. 3–67.

[89] K. Yee, "Numerical solution of initial boundary value problems involving maxwell's equations in isotropic media," *IEEE Transactions on Antennas and Propagation*, vol. 14, 5 1966.

[90] "Warp-x documentation." [Online]. Available: https://github.com/ECP-WarpX/WarpX

[91] J.-L. Vay, A. Almgren, J. Bell, L. Ge, D. Grote, M. Hogan, O. Kononenko, R. Lehe, A. Myers, C. Ng, J. Park, R. Ryne, O. Shapoval, M. Thévenet, and W. Zhang, "Warp-x: A new exascale computing platform for beam–plasma simulations," *Nuclear Instruments and Methods in Physics Research Section A: Accelerators, Spectrometers, Detectors and Associated Equipment*, vol. 909, 11 2018.

[92] J.-L. Vay, A. Huebl, A. Almgren, L. D. Amorim, J. Bell, L. Fedeli, L. Ge, K. Gott, D. P. Grote, M. Hogan, R. Jambunathan, R. Lehe, A. Myers, C. Ng, M. Rowan, O. Shapoval, M. Thévenet, H. Vincenti, E. Yang, N. Zaïm, W. Zhang, Y. Zhao, and E. Zoni, "Modeling of a chain of three plasma accelerator stages with the warpx electromagnetic pic code on gpus," *Physics of Plasmas*, vol. 28, 2 2021.

[93] "Marconi100 cineca." [Online]. Available: https://www.hpc.cineca.it/hardware/marconi100

[94] "openpmd documentation." [Online]. Available: https://openpmd-api.readthedocs.io/en/0.14.2/

[95] "Apollon laser facility." [Online]. Available: https://apollonlaserfacility.cnrs.fr/en/home/

[96] J. Li, P. Forestier-Colleoni, M. Bailly-Grandvaux, C. Mcguffey, A. V. Arefiev, S. S. Bulanov, J. Peebles, C. Krauland, A. E. Hussein, T. Batson, J. C. Fernandez, S. Palaniyappan, R. P. Johnson, G. M. Petrov, and F. N. Beg, "Laser-driven acceleration of quasi-monoenergetic, near-collimated titanium ions via a transparency-enhanced acceleration scheme recent citations laser-driven

acceleration of quasi-monoenergetic, near-collimated titanium ions via a transparency-enhanced acceleration scheme," *New J. Phys*, vol. 21, p. 103005, 2019. [Online]. Available: https://doi.org/10.1088/1367-2630/ab4454

[97] J. Babaei, L. A. Gizzi, P. Londrillo, S. Mirzanejad, T. Rovelli, S. Sinigardi, and G. Turchetti, "Rise time of proton cut-off energy in 2d and 3d pic simulations," *Physics of Plasmas*, vol. 24, 4 2017.

[98] S. Sinigardi, J. Babaei, and G. Turchetti, "Tnsa proton maximum energy laws for 2d and 3d pic simulations," *Nuclear Instruments and Methods in Physics Research Section A: Accelerators, Spectrometers, Detectors and Associated Equipment*, vol. 909, 11 2018.

[99] T. Morita, T. Z. Esirkepov, S. V. Bulanov, J. Koga, M. Yamagiwa, S. V. Bulanov, and H. Daido, "Proton acceleration by oblique laser pulse incidence on a double-layer target." AIP, 2008.

[100] J. Ferri, E. Siminos, L. Gremillet, and T. Fülöp, "Effects of oblique incidence and colliding pulses on laser-driven proton acceleration from relativistically transparent ultrathin targets," *Journal of Plasma Physics*, vol. 86, 10 2020.